LAL 14-161
Juillet 2014

Comprendre le monde,
construire l'avenir®

Université Paris-Sud

Ecole Doctorale Particules, Noyaux et Cosmos (ED 517)
Laboratoire de l'Accélérateur Linéaire

Discipline : Physique

Thèse de doctorat

Soutenue le 03 Juillet 2014 par

Samuel Franco

Searching for long transient gravitational waves in the LIGO-Virgo data

Directeur de thèse :	M. Patrice Hello	Professeur (Université Paris-Sud)
Composition du jury :		
Président du jury :	M. Achille Stocchi	Professeur (Université Paris-Sud)
Rapporteurs :	M. Nelson Christensen	Professeur (Carleton College)
	M. Rémi Michel	Professeur (Université Pierre et Marie Curie)
Examinateurs :	M. Robert Mochkovitch	Directeur de recherche (Institut d'Astrophysique de Paris)
	M. Patrick Sutton	Professeur (Cardiff University)

Disclaimer

The work presented in this thesis has not been reviewed by the LIGO Scientific Collaboration or the Virgo Collaboration. Therefore it should not be taken as representative of the scientific opinion of either collaboration. This document has been assigned Laboratoire de l'Accélérateur Linéaire number LAL 14-161, LIGO document number LIGO-P1400133, Virgo document number VIR–0346A-14.

Contents

Remerciements

Après trois ans de bons et loyaux services, il est temps pour moi de mettre la touche finale à ce manuscrit, aboutissement de ma première, modeste, contribution à la Science. Il me faut faire attention, d'aucuns disent que c'est la seule partie de ma thèse qui sera lue avec attention ! Comme il est de coutume, je voudrais commencer par remercier Achille Stocchi, pour m'avoir tout d'abord accepté en Master 2, puis pour m'avoir accepté comme étudiant en thèse au LAL, et enfin pour avoir accepté de présider mon jury de thèse. Je voudrais ensuite remercier les autres membres du jury : merci Nelson pour tes conseils, pour ta bonne humeur, ta franchise, et surtout pardon mille fois pour t'avoir infligé la lecture d'un manuscrit dans un anglais disons approximatif. Merci à Rémi Michel d'avoir accepté à son tour de rapporter une thèse d'un domaine différent du sien, ce qui a dû être une tâche difficile. Merci également à mes examinateurs, Robert Mochkovitch et Patrick Sutton, pour avoir également accepté de faire encore une fois partie d'un jury de thèse Virgo au LAL !

Ougha à Patrice Hello, mon directeur de thèse, de m'avoir accepté comme doctorant – et comme passager dans sa voiture – pour le meilleur et parfois le pire. Etudiant j'ai pris beaucoup de plaisir à assister à tes cours de mécanique pour l'agrégation, et thésard j'ai pu apprécier ton humour, ta culture scientifique, science-fictionnesque et cinématographique. J'ai lu *Rendez-vous avec Rama*, et j'ai découvert *Citizen Kane* et la signification de *Rosebud*. Grâce à toi j'ai découvert le monde de la recherche, et j'ai pu le faire en prenant part à l'expérience la plus élégante de la physique moderne. Un très grand merci.

Merci également aux membres du groupe ! En premier lieu merci à Nicolas Leroy, notre directeur de la communication, pour m'avoir fait découvrir Virgo en mini-stage, mais surtout pour ton aide précieuse en informatique, ta disponibilité légendaire et ta sympathie. Merci à Marie-Anne, qui s'est beaucoup investie dans mon projet de thèse, et dont l'aide au quotidien (et les relectures très minutieuses de tous mes écrits) a été extrêmement précieuse. Merci également à Florent, qui a partagé son bureau et son expérience du DetChar avec moi, ainsi qu'à Fabien, toujours de bonne humeur, qui a été un lien précieux avec notre Nîmes natale. Merci à Marie, ma collègue thésarde, qui a traversé ces trois ans de thèse avec moi, et qui m'a fait découvrir les méandres de Virgo. Je te souhaite une brillante réussite dans ta future carrière ! Merci aussi à Tessa à qui je souhaite également de réussir dans son parcours académique. Merci enfin à mon prédécesseur, Michal, dont la thèse m'a aidé à rédiger la mienne.

Il n'est pas du groupe, mais un grand merci à mon parrain de thèse, Mathieu, dont les conseils m'ont aidé à traverser les périodes les plus difficiles de ces dernières années.

Je passe maintenant à mes camarades de NPAC qui ont rendu ces trois années de thèse plus faciles : Merci à Estelle ma binôme, bien sûr, Guillaume, Vincent, Jérémy, Agnès Ferté, Marco, Asénath, Pierre et Marie. Merci pour les repas, pour les soirées, pour les pauses LAL et pas LAL, merci encore et courage pour la suite !

I will now switch to English since I have American folks to thanks! First I want to thank the STAMP group in Minnesota: Eric, Vuk, Shivaraj and Michael, thank you for your warm welcome in the States, and for all the good work we have done together. Last but not least, many thanks to my friend Tanner, who worked with me on STAMPAS. It is hard to find the right words to express my gratitude for your kindness, for inviting me into your apartment, for explaining to me american customs and sports rules, for the debates on the French and English languages and accents, for the good times we had together both in the US and in France, for the meals we shared. I will miss working with you, and I

sincerely hope we will meet again. Thank you Tanner, and thanks to your lovely wife Katie too. I wish you all the best.

Les dernières lignes de ces remerciements vont à mes proches, qui m'ont accompagné depuis le tout début, et bien que parfois loin de moi, ont toujours pensé à moi et m'ont aidé au mieux. Merci donc à mes amis Jean-Baptiste, Brice, Anne, Johann, Jérémy et Arnaud, ma tribu de Joffre, sans oublier Julien et Samuel, mes amis khâgneux. Je pense à vous ! Merci à Jacques, qui m'a accueilli chez lui depuis mon M1, et qui avec le temps est devenu bien plus qu'un logeur: un ami très cher. Une pensée également à sa grande famille. Et merci à tous ceux que je n'ai pas cités, j'espère que vous ne m'en voudrez pas (trop).

Bien évidemment, j'adresse ici à ma famille un énorme merci : particulièrement à ma maman Chantal, mon papa André, ma grande sœur Mélanie, mon beau-frère Pascal et leur merveilleux fils Paulin, qui ont toujours cru en moi et sans qui je ne serai pas l'homme que je suis. Merci également à mes beaux-parents Véronique et Patrick et à ma belle-sœur Fanny, je vous adore ! Un merci tout particulier à mon cousin Jean-Marie, qui partage mes rêves d'étoiles et d'espace depuis tout petit. J'espère que vous êtes et resterez fiers de moi.

Mes derniers mots sont pour toi Lucie. Toi qui as accepté de partager ta vie avec moi, et qui m'a toujours soutenu quand ça n'allait pas, qui est restée avec moi malgré mes faiblesses. Tu as fait de ces trois années une période de bonheur immense, et je n'aurais jamais pu faire ce que j'ai fait sans ton amour. Je suis fier d'être ton fiancé. Je t'aime fort.

Synthèse

Les ondes gravitationnelles sont une perturbation de la métrique de l'espace-temps. Conséquences directes de la théorie de la Relativité Générale d'Einstein, elles sont émises par une grande variété d'objets astrophysiques, en particulier des astres compacts comme les étoiles à neutrons et les trous noirs. Interagissant très peu avec la matière, leur détection est l'un des grands défis de la physique moderne, car ces ondes sont potentiellement un vecteur d'informations très riche sur des phénomènes difficilement ou totalement impossibles à observer dans le domaine électromagnétique. Cependant leur faible interaction avec la matière rend leur détection ardue.

Ce n'est que très récemment que les progrès technologiques ont permis la création de détecteurs suffisamment sensibles pour détecter des ondes gravitationnelles. Virgo et LIGO sont des interféromètres de Michelson de bras longs respectivement de 3 km et 4 km, conçus spécialement pour détecter les ondes gravitationnelles. Celles-ci changent le chemin optique parcouru par la lumière et ainsi affectent le schéma d'interférences en sortie de l'interféromètre.

Cette thèse présente un pipeline d'analyse de données issues de ces détecteurs. Le but de ce pipeline, appelé STAMPAS, est de détecter des signaux transitoires longs, c'est-à-dire des ondes gravitationnelles d'une durée d'une à plusieurs centaines de secondes. Ces signaux ont été jusqu'à présent largement ignorés par les pipelines de recherche de signaux transitoires actuels, généralement concentrés sur la recherche de signaux très courts ou de forme connue. STAMPAS doit être capable de détecter des signaux transitoires longs sans information préalable sur l'instant de leur détection ou leur position dans le ciel, ni sur leurs propriétés.

Les ondes gravitationnelles

Les ondes gravitationnelles sont une conséquence de la théorie de la Relativité Générale, élaborée par Albert Einstein au début du vingtième siècle. Cette théorie décrit l'espace-temps de manière géométrique. L'objet mathématique central dans cette description est le tenseur métrique, qui définit en tout point de l'espace-temps la distance entre deux points infiniment proches. Cet objet intervient notamment dans la construction du tenseur d'Einstein $G_{\mu\nu}$ qui décrit la courbure de l'espace-temps. $G_{\mu\nu}$ est relié au contenu matériel et énergétique de l'univers par les équations d'Einstein.

Cette équation est très difficile à résoudre dans un cadre général. En introduisant un terme de perturbation h dans le tenseur métrique, et en linéarisant en h les équations d'Einstein, la résolution est possible, et leurs solutions sont les ondes gravitationnelles. Ce sont des ondes transverses se propageant à la vitesse de la lumière c. Elles possèdent deux états de polarisation: "plus" et "croix" $(+, \times)$, ainsi nommés à cause de l'effet du passage d'une onde gravitationnelle à travers un anneau de masses test. Une onde gravitationnelle se propageant dans une direction orthogonale au plan d'un tel anneau, de polarisation "+", allongera et rétrécira alternativement l'anneau dans deux directions séparées par un angle de 90 °. Une onde polarisée "×" aura le même impact, mais dans deux directions séparées des précédentes d'un angle de 45 °. Toute combinaison linéaire de ces états de polarisation est possible. En particulier, si les deux polarisations " + " et " × " sont en quadrature de phase, l'onde est dite polarisée circulairement.

Les ondes gravitationnelles sont théoriquement émises par toute distribution de masse ou d'énergie en mouvement accéléré. Toutefois pour que l'émission d'ondes gravitationnelles soit suffisamment puissante pour être détectée, la source doit être compacte (son rayon doit être proche de son rayon de Schwarzschild), asymétrique et relativiste. Cela limite le champ des sources observables aux objets astrophysiques. Aucune détection directe n'a été réalisée à ce jour, cependant les ondes gravitationnelles ont déjà été observées indirectement. L'un des exemples les plus connus d'observation indirecte est la mesure de la période de révolution du pulsar binaire dit d'Hulse-Taylor, PSR B1913+16. Cette dernière

a en effet été observée pendant plusieurs dizaines d'années. Elle décroît avec le temps conformément aux prédictions de la Relativité Générale qui prévoit que ce système perde de l'énergie avec le temps par émission d'ondes gravitationnelles, entraînant une diminution de sa période orbitale. Plus de détails sur la théorie des ondes gravitationnelles se trouvent dans le chapitre 1 de cette thèse.

La détection des ondes gravitationnelles

Malgré la puissance d'émission des sources astrophysiques d'ondes gravitationnelles, leur éloignement est tel que les ondes émises par ces objets ont une amplitude très faible en arrivant sur Terre. Pour pouvoir les détecter, un instrument de très grande sensibilité est requis. Virgo est un interféromètre de Michelson, dont les bras sont longs de 3 km. Situé près de Pise en Italie, il fait partie de la première génération de détecteurs interférométriques assez sensibles pour espérer observer directement les ondes gravitationnelles. Il fonctionne à l'aide d'un laser de longueur d'onde égale à 1064 nm, et d'une puissance d'environ 20 W. En plus de la séparatrice et des miroirs de fin de bras, des miroirs supplémentaires dans chacun des deux bras forment une cavité Fabry-Perot dans chacun d'eux. La longueur des cavités est un multiple de la moitié de la longueur d'onde du laser afin que ce dernier entre en résonance avec les cavités. Le chemin optique parcouru par la lumière passe ainsi de 3 km à environ 100 km. Enfin un miroir placé avant la séparatrice permet de recycler la puissance lumineuse en assimilant l'interféromètre entier à une cavité Fabry-Perot. Une photo-diode placée en sortie de l'interféromètre, mesure l'intensité lumineuse résultant de l'interférence des faisceaux lasers présents dans les deux bras de l'interféromètre.

Chaque miroir de l'interféromètre est attaché à un super-atténuateur, composé d'un pendule inversé et d'une chaîne de plusieurs amortisseurs sismiques. Ce dispositif atténue les vibrations du sol de quatorze ordres de grandeur en amplitude pour des fréquences d'oscillation supérieures à 10 Hz. En outre les miroirs attachés à ce système se comportent comme des masses libres au sens de la Relativité Générale, condition nécessaire pour tester cette dernière.

L'interféromètre est réglé, en l'absence de perturbation extérieure, sur une frange noire. En sortie de l'interféromètre, il y a interférence destructrice. Lorsqu'une onde gravitationnelle traverse le détecteur, le chemin optique de la lumière change différemment dans les deux bras. Cela induit un changement du schéma d'interférence, se traduisant par une variation temporaire de la puissance détectée. Cette variation d'amplitude est directement proportionnelle à l'amplitude de l'onde gravitationnelle ainsi détectée. L'amplitude lumineuse détectée est par ailleurs le seul canal physique de l'interféromètre. Ce canal est ensuite étalonné pour fournir $h(t)$. Il est alors directement comparable à l'amplitude d'une onde gravitationnelle.

L'un des défis majeurs de la mise en œuvre d'un tel détecteur est la compréhension et la suppression des bruits de fond. En effet une expérience aussi sensible que Virgo est affectée par une multitude de sources de bruits. On classe ces derniers en trois catégories : les bruits fondamentaux, qui sont dus à la nature même du détecteur, les bruits techniques, dus au matériel utilisé, et enfin les bruits environnementaux dus aux sources extérieures à l'interféromètre.

Parmi les bruits fondamentaux les plus importants, on peut citer le bruit de comptage de photons, dû à la nature quantique de la lumière. La mesure d'une intensité lumineuse par une photo-diode peut en effet se voir comme un comptage du nombre de photons atteignant la photo-diode par unité de temps. Or un tel comptage est soumis à une incertitude statistique qu'il n'est pas possible de supprimer. Ce bruit est particulièrement important à haute fréquence (> 500 Hz). Toutefois le bruit de comptage de photons peut être réduit en augmentant la puissance du laser, ce qui est accompli grâce au miroir de recyclage, et en augmentant la longueur du chemin optique des photons. Cela est accompli grâce aux cavités Fabry-Perot présentes dans chaque bras. Le bruit dû aux fluctuations thermiques des surfaces des miroirs et des fils de suspension est dominant en dessous de 500 Hz. Certains de leurs modes mécaniques de vibrations réduisent considérablement la sensibilité de l'interféromètre – ils ne sont toutefois gênants qu'à des fréquences spécifiques. Enfin, parmi les bruits environnementaux, le bruit sismique demeure la source la plus importante. Sa réduction à l'aide de

dispositifs de suspension adéquats les rend toutefois négligeables dans la bande de sensibilité de Virgo.

La compréhension des sources de bruits ainsi que les diverses stratégies employées pour les réduire ou les supprimer permet à Virgo d'être sensible à des variations relatives de longueur du chemin optique des photons de 10^{-21} environ, avec une sensibilité nominale entre 10 Hz et 10 000 Hz.

Un interféromètre de Michelson tel que Virgo ne peut prétendre faire de l'astronomie à lui seul. En effet la réponse d'un interféromètre aux signaux qu'il reçoit ne dépend que peu de la provenance des signaux. En d'autres termes ce type de détecteur n'est pas directionnel et ne peut localiser la source d'un signal. De plus, dans les directions des bissectrices des bras de l'appareil, l'interféromètre possède une sensibilité quasi-nulle. Pour pouvoir faire de l'astronomie, il est nécessaire d'utiliser un réseau d'interféromètres. Virgo a signé un accord de collaboration avec son homologue américain, LIGO, qui gère 3 différents interféromètres de même nature que Virgo : deux basés dans l'état de Washington, et le dernier en Louisiane. Ces interféromètres partagent leurs données et rendent possible l'astronomie gravitationnelle à proprement parler. Les résultats présentés dans cette thèse sont d'ailleurs essentiellement basés sur les données acquises par deux des interféromètres de LIGO. Plus de détails sur la détection d'ondes gravitationnelles par interférométrie sont présents dans le chapitre 2 de cette thèse.

Les sources d'ondes gravitationnelles - Cas particulier des signaux transitoires longs

Les sources astrophysiques d'ondes gravitationnelles détectables par LIGO et Virgo peuvent être réparties en quatre catégories. Le fond stochastique d'ondes gravitationnelles est la somme de toutes les ondes gravitationnelles émises dans l'univers. La coalescence de systèmes binaires d'étoiles à neutrons est une source à part : extrêmement bien modélisée théoriquement, des analyses très efficaces spécifiquement dédiées à ce type de signal ont pu être conçues. Les sources

continues sont des objets qui émettent en permanence des ondes gravitationnelles, généralement à fréquence constante, les pulsars en sont un bon exemple. Enfin les sources transitoires émettent ponctuellement des ondes gravitationnelles. Ce sont essentiellement des objets compacts excités, comme des étoiles à neutrons et des trous noirs.

On peut classer les sources transitoires en deux catégories : les signaux transitoires courts, durant jusqu'à une seconde, et les signaux transitoires longs, plus longs qu'une seconde. Ces signaux ont déjà été étudiés par plusieurs analyses différentes. Les signaux transitoires longs n'ont été que peu recherchés, à cause notamment de l'absence de modèles systématiques de telles ondes gravitationnelles, et des forts besoins en temps de calculs qu'une telle analyse implique en pareil cas. Les principales sources de signaux transitoires longs sont les proto-étoiles à neutrons, les instabilités des disques d'accrétion et les coalescences de binaires excentriques de trous noirs.

Les proto-étoiles à neutrons, formées au cœur des supernovæ à effondrement gravitationnel, peuvent émettre des signaux transitoires longs par deux mécanismes principaux. D'abord les mouvements de convection induits par les retombées de matière sur l'étoile à neutron en formation peuvent être sources d'ondes gravitationnelles pendant une trentaine de secondes. Les ondes gravitationnelles émises auraient une fréquence d'au moins 300 Hz, et seraient détectables si émises depuis notre galaxie. Enfin les étoiles à neutrons peuvent subir des instabilités de rotation, les rendant non-sphériques pendant une courte période. Cette asphéricité couplée à une grande vitesse de rotation engendre des ondes gravitationnelles d'une fréquence proportionnelle au carré de la vitesse de rotation de l'étoile à neutrons. Ce phénomène peut durer plusieurs minutes et émettre des ondes gravitationnelles détectables dans un rayon de 30 Mpc.

Les disques d'accrétion formés autour des trous noirs peuvent contenir des instabilités magnétohydrodynamiques, notamment engendrées par l'interaction avec le champ magnétique de l'astre central. Ces instabilités peuvent émettre des ondes gravitationnelles détectables jusqu'à une distance de plusieurs dizaines

de mégaparsecs. Leur fréquence inférieure à 1 kHz rentre dans la bande de détection des instruments.

Enfin les binaires excentriques de trous noirs, formées par capture gravitationnelle, peuvent émettre lors de leur fusion des signaux transitoires longs. Ces signaux peuvent durer plusieurs dizaines de secondes, montant régulièrement en fréquence à mesure que la coalescence approche, jusqu'à atteindre plusieurs centaines de hertzs. Plus de détails sur les sources d'ondes gravitationnelles, et en particulier sur les signaux transitoires longs, sont donnés au chapitre 3 de cette thèse.

Le pipeline STAMPAS

Le sujet principal de cette thèse est l'élaboration d'un pipeline d'analyse spécialisé dans la détection de signaux transitoires longs, sans aucune hypothèse sur la forme ou la provenance de ces signaux. Ce pipeline, nommé STAMPAS, est basé sur un pipeline pré-existant, STAMP (Stochastic Transient Analysis Multi-detector Pipeline). STAMP calcule la fonction de corrélation $s(t) = h_{I1}(t) \otimes h_{I2}(t)$ des données de deux interféromètres, puis en calcule la transformée de Fourier par segments de 1 seconde. Après normalisation, notamment pour tenir compte des facteurs d'antennes associés à chaque interféromètre, une quantité $Y(t, f)$ est obtenue. Elle peut être représentée sur une carte temps-fréquence, de résolution $1\ \mathrm{s} \times 1\ \mathrm{Hz}$.

La variance de cette quantité, pour un pixel donné, s'estime *via* le produit des fonctions d'autocorrélation $P_{I1}(t) = h_{I1}(t) \otimes h_{I1}(t)$ et $P_{I2}(t) = h_{I2}(t) \otimes h_{I2}(t)$. La moyenne de ce produit est faite sur les pixels les plus proches du pixel considéré. Le rapport de $Y(t, f)$ sur sa variance en un pixel donné est appelé rapport signal sur bruit (SNR). Une fois tracé sur une carte temps-fréquence, un algorithme regroupe les pixels de SNR significatif. Ces groupements sont appelés "triggers" et sont individuellement des candidats potentiels d'ondes gravitationnelles. Notons ici que l'algorithme est doté d'un outil interne de sélection des données, appelé "glitch cut". La glitch cut supprime automatiquement les bins des cartes

temps-fréquence qui contiennent beaucoup d'énergie ne provenant que d'un seul interféromètre, et qui ne sont donc pas compatibles avec un signal d'onde gravitationnelle fort – qui doit être visible dans les deux interféromètres *a priori*. Cela supprime les triggers générés par les excès de puissance présents dans les données et dus non pas à des ondes gravitationnelles mais à des anomalies techniques ou environnementales perturbant le signal de la frange noire.

Le pipeline STAMP est conçu pour être utilisé en connaissant par avance la position spatio-temporelle du signal recherché. En effet la corrélation des deux interféromètres n'est maximale, lorsqu'un signal est présent, que si le décalage temporel qui sépare la détection de l'onde gravitationnelle par le premier interféromètre et par le second, est pris en compte. Or ce décalage dépend de la provenance spatiale du signal. Ainsi, pour transformer le pipeline STAMP en pipeline multi-directionnel, le plus simple serait d'analyser, à chaque instant, toutes les positions du ciel possibles. En prenant en compte le fait qu'un même décalage de phase correspond en réalité à un anneau de positions possibles dans le ciel, il faudrait analyser, pour une résolution angulaire de 0,7 degrés, plusieurs centaines de positions, le nombre exact dépendant de l'éloignement des détecteurs utilisés. Cette approche est toutefois impossible à mettre en œuvre en pratique, car bien trop coûteuse en termes de puissance de calcul.

Cet obstacle peut être contourné en modifiant l'algorithme de regroupement des pixels. En effet ce dernier regroupe les pixels de fort SNR, nécessairement positif. Or tel qu'il a été défini, le SNR d'un pixel de STAMP peut être négatif si les données dont il est issu sont anti-corrélées. Si l'on recherche un signal présent dans les données, mais dans une mauvaise direction, ce dernier apparaîtra néanmoins dans la carte temps-fréquence, mais il sera vu comme une alternance de groupes de pixels de SNR positif et négatif, correspondant à des données corrélées et anti-corrélées. Si l'on prend en compte cet effet, il est possible de réduire le nombre de positions à analyser de plusieurs centaines à seulement 5. Ce nombre de positions est le meilleur compromis possible entre efficacité de détection et temps de calcul requis. Pour un gain d'un facteur 100 en temps de calcul, on obtient une perte de 10 % en termes d'efficacité de détection.

Le pipeline STAMPAS, pour STAMP-All Sky, fonctionne de la manière suivante : les périodes d'acquisition de données communes aux deux interféromètres étudiés sont découpées en fenêtres de 500s, se chevauchant sur une durée de 10s. Pour chacun de ces segments, cinq positions aléatoires du ciel seront analysées en utilisant les outils de STAMP et l'algorithme de regroupement de pixels approprié. Si des triggers se trouvent au bord d'une fenêtre de 500 s, la fenêtre suivante est agrandie pour pouvoir contenir le trigger intégralement, au cas où ce dernier soit à cheval sur deux fenêtres. Enfin si un signal est présent quasiment à l'identique (fréquences et temps GPS similaires) dans plusieurs directions, seul le trigger de SNR le plus élevé est conservé pour l'analyse.

Pour estimer l'efficacité de détection du pipeline vis-à-vis de signaux spécifiques, il est possible de réaliser des injections, c'est-à-dire d'ajouter aux données des signaux simulés, de différentes amplitudes, puis d'essayer de les détecter en utilisant le pipeline. On peut ainsi tracer une courbe représentant le nombre d'injections retrouvées par le pipeline sur le nombre total d'injections effectuées, en fonction de l'amplitude des injections, pour un signal donné. Un seuil en SNR est imposé pour tenir compte du bruit de fond; ainsi seules les injections retrouvées avec un SNR plus grand que ce seuil sont considérées dans le précédent calcul. Plus de détails sur le pipeline STAMPAS se trouvent dans le chapitre 4 de cette thèse.

L'analyse S5

Description - Etude du bruit de fond

La première analyse effectuée à l'aide du pipeline STAMPAS l'a été sur les données issues de la cinquième période d'acquisition de données (S5) des interféromètres LIGO-Hanford (H1) et LIGO-Livingston (L1), de Novembre 2005 à Octobre 2007. Environ 272 jours de données cumulées ont été utilisés. Notons que certaines fréquences, connues pour être sources de bruit hautement non stationnaire, ont été supprimées des cartes temps-fréquence. Les signaux d'ondes gravitationnelles choisis pour tester l'efficacité du pipeline sont cinq modèles différents

de signaux issus d'instabilités de disques d'accrétion (ADIs pour Accretion Disk Instabilities) et cinq modèles de signaux issus de coalescence de binaires excentriques de trous noirs (EBBHs pour Eccentric Black Hole Binaries).

Pour estimer le bruit de fond de l'analyse, une méthode classique a été utilisée, la décalage temporel. Les canaux $h_{H1}(t)$ de H1 et $h_{L1}(t)$ L1 ont été décalés l'un par rapport à l'autre avant d'être corrélés. Cette opération supprime naturellement toute corrélation due à la présence d'une onde gravitationnelle. Par ailleurs cette corrélation "en décalé" possède des propriétés statistiques similaires à celle de la corrélation des données non décalées. En répétant l'opération plusieurs fois, on peut ainsi obtenir une durée effective de données de bruit de fond beaucoup plus importante que la durée des données brutes. Cela permet une estimation du bruit de fond plus précise. Pour cette analyse, 200 décalages de durées différentes ont été réalisés, pour une durée de données cumulée d'environ 150 ans.

Le but de cette étude des bruits de fond est essentiellement d'élaborer des stratégies pour supprimer les triggers issus du bruit, sans risquer de supprimer des signaux d'ondes gravitationnelles. Deux méthodes de sélection ont été élaborées à cet effet. La première est basée sur le constat que, parmi les signaux de bruits de fond les plus importants obtenus, beaucoup sont dus à la corrélation malheureuse de deux artefacts très courts présents dans les données des deux interféromètres, vraisemblablement dus à des défaillances techniques brèves ou des bruits environnementaux. Dans les cartes temps-fréquence, ils se présentent comme des signaux assez brefs, durant généralement moins de dix secondes, dont l'essentiel de la puissance est concentrée dans une période de moins d'une seconde. Ce comportement est essentiellement différent de celui de la plupart des signaux attendus. Une quantité nommée SNRfrac a été élaborée : c'est, pour un trigger donné, la fraction la plus importante de SNR contenue dans un seul et unique bin de temps. Pour des signaux de bruits comme ceux décrits précédemment, cette valeur est très élevée, alors qu'elle vaut généralement moins de 50 % pour la plupart des signaux étudiés, la seule exception étant les EBBHs, dont une bonne partie de l'énergie est concentrée dans les toutes dernières secondes. Pour ces signaux précis, une sélection utilisant SNRfrac avec un seuil trop bas serait

coûteuse en termes d'efficacité de détection. Pour cette raison l'analyse a été séparée en deux : une analyse principale utilisant une coupure sur la valeur de SNRfrac des triggers à 50 % – *i.e.* seuls les triggers dont SNRfrac vaut moins de ce seuil sont préservés – et une analyse dédiée aux EBBHs utilisant une valeur de coupure sur SNRfrac de 99 %.

La deuxième sélection s'est faite en utilisant des vetos. Les vetos sont des listes de segments temporels fournis par des équipes de LIGO et Virgo de périodes où les données acquises par les interféromètres sont affectées par des sources de bruits identifiées. Un trigger survenant durant l'une de ces périodes est très probablement un trigger issu du bruit de fond. Toutefois des milliers de ces listes de vetos existent, tous n'étant pas pertinents selon l'analyse choisie. Une sélection de vetos adaptés à STAMPAS a été réalisée en utilisant les listes de vetos le plus souvent coïncidentes avec les cent plus importants triggers issus du bruit de fond, et dont le nombre de coincidences avec les dits trigger était significativement plus important qu'avec une sélection aléatoire de segments temporels. Au final les segments affectés par les vétos représentent environ 3 % des données de chaque interféromètre.

Une fois ces sélections appliquées sur les triggers du bruit de fond, on observe une réduction significative des triggers de SNR élevé. Dans le cas de l'analyse principale, qui utilise la sélection la plus stricte, la distribution de triggers est presque équivalente à celle obtenue en utilisant des données Gaussiennes générées *via* Monte-Carlo. La réduction du bruit de fond est moins significative dans le cas de l'étude dédiée aux signaux issus de binaires excentriques de trous noirs. L'efficacité de détection de ces signaux est d'ailleurs moins importante que celle obtenue pour les ADIs. Notons ici que les résultats présentés jusque là concernent uniquement des triggers issus de données "décalées" : toutes ces sélections sont établies en aveugle, et les triggers issus des données corrélées sans décalage temporel ne sont pas connus à ce stade de l'analyse. Plus de résultats sur l'étude du bruit de fond de l'analyse sont donnés dans le chapitre 5 de cette thèse.

Résultats

Une fois les moyens de sélection des données choisie, on les applique en aveugle sur les triggers issus des données corrélées sans décalage temporel. La distribution de triggers ainsi obtenue est compatible avec le bruit de fond estimé précédemment, et ce avec l'analyse principale et l'analyse dédiée aux EBBHs. Le trigger de SNR le plus élevé ne possède pas de caractéristique incompatible avec un signal issu du bruit de fond. Aucun signal d'onde gravitationnelle n'a donc été détecté.

En l'absence de détection, il est possible de fixer des limites hautes sur les taux d'ADIs et d'EBBHs observables, avec un indice de confiance de 90 %. Ces limites vont de $1,43 \cdot 10^{-4}$ $\mathrm{Mpc}^{-3}\mathrm{an}^{-1}$ à $3,77 \cdot 10^{-2}$ $\mathrm{Mpc}^{-3}\mathrm{an}^{-1}$ pour les ADIs, et de $5,15 \cdot 10^{-3}$ $\mathrm{Mpc}^{-3}\mathrm{an}^{-1}$ à $3,73 \cdot 10^{-2}$ $\mathrm{Mpc}^{-3}\mathrm{an}^{-1}$ pour les EBBHs. Les prévisions théoriques pour les taux d'ADIs sont de 10^{-6} $\mathrm{Mpc}^{-3}\mathrm{an}^{-1}$, ce qui reste plus faible que les limites fixées par l'analyse. Néanmoins ce résultat reste prometteur puisque la prochaine génération de détecteurs d'ondes gravitationnelles sera dix fois plus sensible que la génération actuelle, ce qui entraînera une augmentation d'un facteur 1000 du volume observable, et une diminution du même ordre des limites hautes que STAMPAS pourra établir. Ces limites seront dès lors du même ordre de grandeur que les prédictions astrophysiques, ce qui laisse l'espoir d'une détection, et en tout cas l'assurance de placer des limites contraignantes sur les modèles astrophysiques. Pour les EBBHs, les limites hautes fixées sont loin du taux prévu par les modèles, même le plus optimiste qui est de 10^{-6} $\mathrm{Mpc}^{-3}\mathrm{an}^{-1}$. En l'absence de changement dans le pipeline, cette situation demeurera lors de la prochaine génération de détecteurs. Les résultats complets de l'analyse sont présentés dans le chapitre 6 de cette thèse.

Le futur de STAMPAS

Malgré de très bons résultats, STAMPAS peut encore être amélioré. Plusieurs problèmes sont en effet apparus lors de la création de ce pipeline. Le plus important d'entre eux est un biais dans l'estimation de la variance de la quantité $Y(t, f)$. Cette dernière est en effet estimée pour un pixel donné en utilisant les

données des pixels voisins en fréquence. Or pour des signaux dont la fréquence est stable sur une échelle de quelques secondes, ces pixels voisins peuvent contenir du signal, ce qui biaise l'estimation de la variance de $Y(t, f)$ qui doit théoriquement être réalisée sur du bruit seul. Cela a pour conséquence de diminuer le SNR de certains signaux particuliers, dont certains ADIs utilisés pendant l'analyse. La détection de signaux totalement monochromatiques est par ailleurs pratiquement impossible à cause de cet effet.

Une solution à ce biais a été étudiée dans cette thèse. Une estimation alternative de la variance a été proposée. Pour cette estimation, chaque carte temps-fréquence est virtuellement coupée en deux cartes de durée égale. La variance d'un pixel donné est calculée non pas en utilisant les données des pixels voisins, mais celles des pixels situés au voisinage d'un pixel présent dans l'autre moitié de la carte temps-fréquence. Le gain en SNR des signaux monochromatiques et de certains ADIs est spectaculaire. Toutefois le bruit de fond augmente également significativement avec cette estimation. Cette technique n'a pas été utilisée au final dans l'analyse, à cause de cette augmentation du bruit de fond. Son étude et son perfectionnement continuent néanmoins, afin qu'elle puisse être appliquée dans le futur.

Un autre problème majeur de l'analyse est la faible sensibilité de cette dernière aux signaux issus des binaires excentriques de trous noirs. La ressemblance de ces derniers, aux yeux du pipeline, avec des événements de bruit de fond empêche une bonne réduction de ce dernier, ce qui diminue la sensibilité de STAMPAS. La structure de ces signaux, formés d'une succession de petits signaux très courts, n'est pas bien prise en compte par l'algorithme de regroupement des pixels. En concevant un algorithme alternatif, prenant en compte cette spécificité, l'efficacité de détection de ces signaux serait considérablement améliorée.

Enfin l'inclusion d'un troisième interféromètre à l'analyse, en l'occurrence Virgo, a également été étudiée. Si l'analyse de différentes paires d'interféromètres ne pose pas de problème, la combinaison des résultats de ces différentes analyses n'est pas triviale. Des études préliminaires sur la reconstruction spatiale de l'origine des signaux en utilisant les données des trois paires ont été effectuées,

mais leurs résultats pourront vraisemblablement être améliorés à l'avenir. Une nouvelle statistique regroupant simultanément les données des trois interféromètres est une autre solution, qui reste à explorer.

List of Figures

Introduction

Gravitational waves are perturbations of the geometry of space-time, induced by some of the most violent phenomena in the Universe: supernovæ, binary neutron stars merging, black holes merging and so forth. They are a prediction of Einstein's General Relativity. So far these waves have only been observed indirectly, notably through the observation of the Hulse-Taylor binary system [1], which period decreases with time due to loss of energy *via* emission of gravitational waves. We can also mention here the very recent results of the BICEP2 experiment [2], which observed the B-modes of the Cosmic Microwave Background. If confirmed, this observation would constitute another independent indirect proof of the existence of gravitational waves, these modes being a "smoking gun" of their presence during the inflation.

Gravitational waves are of course an excellent test for General Relativity, but they can also be an extremely valuable vector of information, in particular for astrophysics. Indeed, gravitational waves can be emitted by objects which do not emit light, or not much, like neutron stars and black holes, or which emit light that doesn't carry any information on their internal structure, like supernovæ. As a matter of fact, gravitational waves interact very weakly with matter, therefore they can carry information about their emitters without being contaminated or absorbed during their travel.

However, the weakness of their interaction with matter makes their detection a challenging task. The first attempts to detect such waves go back to the sixties, but it is only recently that technology has reached a level satisfying enough so scientists are confident that the first direct detection will happen before the end

of the decade. The most promising technique to detect gravitational waves is interferometry: gravitational waves affect the interference pattern of Michelson interferometers in such a way that the amplitude of the wave can be deduced from light intensity variations. It is the technique used by the LIGO and Virgo experiments [3, 4].

The subject of this thesis is to describe the functioning and the results of an analysis pipeline, STAMPAS, destined to analyze data from the LIGO and Virgo experiments. This pipeline is dedicated to the search for long transient gravitational wave signals *i.e.* signals lasting from $\mathcal{O}(1s)$ to $\mathcal{O}(100s)$. This category of signals has been neglected by the previous searches, despite of strong astrophysical motivations. STAMPAS is thus the very first attempt to systematically search for such signals in the LIGO and Virgo data.

In the chapter 1 of this thesis, I give a brief summary of General Relativity, insisting specifically on the main results it gives concerning gravitational waves. In chapter 2, I describe the functioning of current interferometric detectors, taking the example of Virgo. I detail its design, its main sources of noise and how can it reach the required sensitivity to claim a detection. In chapter 3, I give a review of the main sources of gravitational waves in the universe which we might detect using LIGO and Virgo, with a strong focus on the astrophysical sources of long transients. In chapter 4 I describe the STAMPAS pipeline, how it generates gravitational wave triggers, how it does analyze the entire celestial sphere at a reasonable computation cost. In the chapter 5, I detail the results of the first full size analysis run with STAMPAS and how the background and the efficiency are estimated. Finally in chapter 6 I describe the issues encountered with the current version of the pipeline and the ideas to correct them. I also present the main axis of the future development of the pipeline.

Chapter 1

General Relativity and Gravitational Waves

"Do not worry about your difficulties in Mathematics. I can assure you mine are still greater."

Albert Einstein

The purpose of this chapter is to introduce the basic notions needed to derive and understand the concept of gravitational waves. It is shamelessly inspired from reference books such as Weinberg, Misner, Hartle, Creighton [5, 6, 7, 8]... I do not intend here to give an extensive review of General Relativity, but rather a comprehensive introduction of the basic principles of the theory, needed to do the calculations related to the main subject of this thesis.

1.1 General Relativity in a nutshell

1.1.1 Historical introduction

General Relativity has been established by Albert Einstein, in an article published in 1916 [9]. It was the conclusion of a thinking process that had begun years before that, a remarkable synthesis of the work of both physicists and mathematicians (Maxwell, Gauss, Riemann, Lorentz, Poincaré, Hilbert and more).

Before I elaborate about this theory, let us take a step backward in time, at the end of the nineteenth century.

Newton's theory of gravitation had been a successful theory for the last two hundred years – one of its greater accomplishments being the prediction of the existence of Neptune *via* calculations before its actual observation.

However, Newton's gravitation has several drawbacks. First, some of its predictions, such as Mercury's perihelion precession, are not accurate. Even more important: classical mechanics are at some level inconsistent with the very recent – and successful – theory of electromagnetism, first published by J.C. Maxwell in 1865 [10]. According to Newton, there is a favored class of reference frames, called *inertial frames*, where the laws of mechanics takes the form given in the *Principia*. For instance, in such frames, the third law of Newton can be written as

$$\vec{F} = m_I \vec{a} \tag{1.1}$$

with m_I the inertial mass. This law is indeed invariant under the Galilean transformations (translation in space and time, rotation and velocity boost).

However, Maxwell's equations are not invariant under this class of transformation. In particular, the speed of light in the vacuum c should change depending on the reference frame. Maxwell thought at that time that his equations were only true in some inertial frames, at rest with respect to the *ether*, hypothetical medium through which light was supposed to propagate. But the experiment of Michelson and Morley (1887) [11] showed that light velocity is the same ($\pm 5\ \mathrm{km\,s^{-1}}$) when traveling along the direction of the Earth's orbit or transverse to it.

Based on the work of Lorentz, Poincaré and others, Einstein modified Newton's mechanics to be invariant under the Lorentz transformations, like Maxwell's equation. Special Relativity was born (1905) [12].

Later on, Einstein continued to work on this theory: indeed *all* laws of physics were now invariant under some class of transformation, but in inertial reference frames only; Einstein worked hard to complete his theory in order to make all physical equations invariant under *general* coordinate transformations. He

achieved is goal in 1916, when he published his paper: *The Foundation of the General Theory of Relativity* [9].

1.1.2 Gravitation and Geometry: Basics of General Relativity

General Relativity is a *geometrical* theory of gravitation: gravitation is not seen like a force as in the Newtonian approach, but rather as a consequence of the shape of the space-time in which particles are moving. In the framework of General Relativity, space-time is described as a four-dimensional manifold, on which can be defined at each point a *tensor* noted $g_{\mu\nu}$, called the *metric tensor*, determining distances between events on the manifold. The infinitesimal distance ds between two infinitely close points of space-time, which infinitesimal coordinates change is noted dx, is given as follows:

$$ds^2 = g_{\mu\nu} dx^\mu dx^\nu \tag{1.2}$$

where we use the Einstein summation convention. In flat space, one has

$$g_{\mu\nu} = \eta_{\mu\nu} = diag(-1, 1, 1, 1) \tag{1.3}$$

where η is the *Minkowski* metric, here expressed in a regular cartesian coordinates system (t, x, y, z). This represents the geometrical framework of Special Relativity.

As stated before, General Relativity is a geometrical theory of gravity: in (1.1) gravity is described as an external force acting on a system. In General Relativity, the movement of a massive test particle is described by the *geodesic* equation,

$$\ddot{x}^\alpha + \Gamma^\alpha_{\beta\gamma} \dot{x}^\beta \dot{x}^\gamma = 0 \tag{1.4}$$

where $\Gamma^{\alpha}_{\beta\gamma}$ are the Christoffel symbols, defined as

$$\Gamma^{\alpha}_{\beta\gamma} = \frac{1}{2} g^{\alpha\delta} \left(\frac{\partial g_{\delta\beta}}{\partial x^{\delta}} + \frac{\partial g_{\delta\gamma}}{\partial x^{\beta}} - \frac{\partial g_{\beta\gamma}}{\partial x^{\delta}} \right) \tag{1.5}$$

and the $\dot{x}$ notation stands for derivative with respect to the proper time of the particle. Christoffel symbols encode the information about how coordinate systems change throughout the manifold. Equation (1.4) can be seen as the equation of the "shortest" path possible, in space-time, for the considered particle, given the space-time geometry surrounding it.

Before the introduction of the linearized equations of General Relativity, and of the gravitational waves, the relation between the distribution of matter and energy in the universe must be established.

Curvature of space-time can also be represented by the *curvature tensor*, which describes vectors parallel displacement in space-time. It is defined as

$$R^{\alpha}_{\beta\mu\nu} = \frac{\partial \Gamma^{\alpha}_{\beta\nu}}{\partial x^{\mu}} - \frac{\partial \Gamma^{\alpha}_{\beta\mu}}{\partial x^{\nu}} + \Gamma^{\alpha}_{\sigma\mu}\Gamma^{\sigma}_{\beta\nu} - \Gamma^{\alpha}_{\sigma\nu}\Gamma^{\sigma}_{\beta\mu} \tag{1.6}$$

In a flat space-time, all components of this tensor are zero.

From this tensor, it is possible to construct the Ricci tensor,

$$R_{\alpha\beta} = R^{\sigma}_{\alpha\sigma\beta} \tag{1.7}$$

and from the Ricci tensor, the Ricci scalar (the so-called *curvature*),

$$R = g^{\alpha\beta} R_{\alpha\beta} \tag{1.8}$$

From these objects, we define the *Einstein tensor*,

$$G_{\alpha\beta} = R_{\alpha\beta} - \frac{1}{2} R g_{\alpha\beta} \tag{1.9}$$

It can be shown that the tensors $G_{\alpha\beta} + \Lambda g_{\alpha\beta}$, with Λ a constant, are the only symmetric tensors, of order 2, made from first and second order derivatives of

the metric tensor with null divergence. Λ is called the *cosmological constant*. In this thesis we consider $\Lambda = 0$.

It is now possible to establish the connection between distribution of matter and energy in the universe *via* the *Einstein's equations*,

$$G_{\mu\nu} = \frac{8\pi G}{c^4} T_{\mu\nu} \tag{1.10}$$

where G is the Newton constant, $G_{\mu\nu}$ is the *Einstein tensor* and $T_{\mu\nu}$ is the *stress-energy* tensor, which represents the distribution of matter, energy and momentum. More specifically, we note here that T_{00} is the energy density, which for a material body is equal to ρc^2 where ρ is the mass density of the material.

1.1.3 Linearized General Relativity: Generation of Gravitational Waves

Einstein's equations are difficult to solve in a general case. However, in the weak field regime, it is possible to linearize them.

In the weak field regime, we assume that

$$g_{\mu\nu} \simeq \eta_{\mu\nu} + h_{\mu\nu} \tag{1.11}$$

with $|h_{\mu\nu}| \ll 1$. Also, we suppose that tensor indices are raised and lowered with the Minkowski metric $\eta_{\mu\nu}$ instead of $g_{\mu\nu}$ *i.e.* that one can write: $h^{\alpha}_{\beta} = \eta^{\alpha\gamma} h_{\gamma\beta}$. This keeps the equations first order in h.

Using this property and equations (1.5), (1.6) and (1.7), we can therefore compute the linearized Ricci tensor,

$$R_{\alpha\beta} = \frac{1}{2}\left(-\frac{\partial^2 h}{\partial x^\alpha \partial x^\beta} + \frac{\partial^2 h^\mu_\beta}{\partial x^\alpha \partial x^\mu} + \frac{\partial^2 h^\mu_\alpha}{\partial x^\mu \partial x^\beta} - \eta^{\mu\nu} \frac{\partial^2 h_{\alpha\beta}}{\partial x^\mu \partial x^\nu} \right) \tag{1.12}$$

where $h = h^\mu_\mu$ is the trace of h^ν_μ. The linearized Ricci scalar can be written, using (1.8), as

$$R = \eta^{\alpha\beta} R_{\alpha\beta} + \mathcal{O}(h^2) = \frac{\partial^2 h^{\mu\nu}}{\partial x^\mu \partial x^\nu} - \eta^{\mu\nu} \frac{\partial^2 h}{\partial x^\mu \partial x^\nu} + \mathcal{O}(h^2) \tag{1.13}$$

With these quantities we can now write the linear form of the Einstein tensor:

$$G_{\alpha\beta} = R_{\alpha\beta} - \frac{1}{2}\eta_{\alpha\beta} R + \mathcal{O}(h^2) \tag{1.14}$$

$$= \frac{1}{2}\left(-\frac{\partial^2 h}{\partial x^\alpha \partial x^\beta} + \frac{\partial^2 h^\mu_\beta}{\partial x^\alpha \partial x^\mu} + \frac{\partial^2 h^\mu_\alpha}{\partial x^\mu \partial x^\beta} - \eta^{\mu\nu} \frac{\partial^2 h_{\alpha\beta}}{\partial x^\mu \partial x^\nu} \right) - \frac{1}{2}\eta_{\alpha\beta}\left(\frac{\partial^2 h^{\mu\nu}}{\partial x^\mu \partial x^\nu} - \eta^{\mu\nu} \frac{\partial^2 h}{\partial x^\mu \partial x^\nu} \right) \tag{1.15}$$

This equation can be simplified by introducing the *trace-reversed metric perturbation*,

$$\bar{h}_{\alpha\beta} = h_{\alpha\beta} - \frac{1}{2}\eta_{\alpha\beta} h \tag{1.16}$$

with $\bar{h} = \bar{h}^\mu_\mu = -h$.

After straightforward calculations, equation (1.15) becomes

$$-\eta^{\mu\nu} \frac{\partial^2 \bar{h}_{\alpha\beta}}{\partial x^\mu \partial x^\nu} - \eta_{\alpha\beta} \frac{\partial^2 \bar{h}^{\mu\nu}}{\partial x^\mu \partial x^\nu} + \frac{\partial^2 \bar{h}^\mu_\beta}{\partial x^\alpha \partial x^\mu} + \frac{\partial^2 \bar{h}^\mu_\alpha}{\partial x^\mu \partial x^\beta} = \frac{16\pi G}{c^4} T_{\alpha\beta} \tag{1.17}$$

The first term on the left-hand side of (1.17) is the opposite of the d'Alembertian operator applied to $\bar{h}_{\alpha\beta}$: $-\Box \bar{h}_{\alpha\beta}$. With the appropriate choice of coordinate system, using the Lorentz gauge, the left-hand side of the previous equation can be reduced to this term only, obtaining a wave equation. Indeed, if we consider an infinitesimal coordinate change $x \to x' = x + \xi$, it can be shown that, in the new coordinate system, we have

$$\bar{h}'_{\alpha\beta} = \bar{h}_{\alpha\beta} - \frac{\partial \xi_\beta}{\partial x^\alpha} - \frac{\partial \xi_\alpha}{\partial x^\beta} + \eta_{\alpha\beta}\eta^{\mu\nu} \frac{\partial \xi_\nu}{\partial x^\mu} \tag{1.18}$$

Now, if we require that in the new coordinate system: $\frac{\partial \bar{h}'^\mu_\beta}{\partial x'_\mu} = 0$ (Lorentz gauge), which is achieved by solving the equation

$$\Box \xi_\alpha = \frac{\partial \bar{h}^\mu_\alpha}{\partial x_\mu} \tag{1.19}$$

then the Einstein's equations can be put into the form

$$\Box\bar{h}_{\alpha\beta} = -\frac{16\pi G}{c^4}T_{\alpha\beta} \tag{1.20}$$

1.2 Gravitational waves

1.2.1 Equation

Now if we place ourselves in the vacuum, (1.20) becomes

$$\Box\bar{h}_{\alpha\beta} = 0 \tag{1.21}$$

which is nothing else but a wave propagation equation. Its simplest solutions are plane waves, which velocity can be immediately deduced from (1.21) as being the speed of light c. They can be expressed as

$$\bar{h}_{\alpha\beta} = \Re[A_{\alpha\beta}e^{ik_\mu x^\mu}] \tag{1.22}$$

with $A_{\alpha\beta}$ the amplitude of the wave and k_μ its wave vector, which respect the conditions:

$$k_\mu k^\mu = 0 \text{ (consequence from (1.21))} \tag{1.23}$$

$$A_{\alpha\mu}k^\mu = \frac{1}{2}k_\alpha A^\mu_\mu \text{ (consequence of Lorentz gauge)} \tag{1.24}$$

The amplitude of the wave $A_{\alpha\beta}$ is a symmetric tensor, and possesses therefore 10 degrees of freedom. Taking into account the previous equations, there are 6 degrees of freedom left.

However, the Lorentz gauge does not totally set the coordinate system, and further gauge choices can still be made. Every infinitesimal change of coordinates respecting (1.21), is possible. In particular, the coordinate change $\varepsilon^\mu(x) = \Re[ie^\mu \exp(ik_\lambda x^\lambda)]$ yields the transformation

$$A'_{\mu\nu} = A_{\mu\nu} + k_\mu e_\nu + k_\nu e_\mu \tag{1.25}$$

We can perform such a transformation so the wave amplitude is traceless, *i.e.* $A'^{\mu}_{\mu} = 0$ and orthogonal to a given observer (in an inertial reference frame) of velocity v: $A'_{\mu\nu}v^\nu = 0$. This gauge is called the *transverse-traceless* gauge. This transformation imposes 4 new constraints to the system, and leave only 2 components of $A_{\mu\nu}$ non zero. These components represent the two polarization states of gravitational waves, called *plus* and *cross* polarizations.

If one chooses a plane wave along the z axis, *i.e.* $k_\mu = (\omega, 0, 0, \omega/c)$, the solution of (1.21) can be written as

$$\bar{h}^{TT}_{\mu\nu} = \Re\left\{ \begin{pmatrix} 0 & 0 & 0 & 0 \\ 0 & A_+ & A_\times & 0 \\ 0 & A_\times & -A_+ & 0 \\ 0 & 0 & 0 & 0 \end{pmatrix} \exp(i\omega(z/c - t)) \right\} \tag{1.26}$$

where TT denotes the transverse-traceless gauge.

1.2.2 Generation of gravitational waves

The previous demonstration shows that gravitational waves can propagate in space-time. However gravitational waves must have sources to generate them. A source of gravitational waves, theoretically, consists of any amount of matter or energy undergoing an acceleration *i.e.* described by a stress-energy tensor T such as $\ddot{T} = 0$ where the dots stand for a double time derivative. In order to better characterize these sources, we will focus in this section on the linearized Einstein equation solutions with a source (1.20). The general solution of this equation is a difficult problem. For astrophysical studies it is nonetheless possible to formulate hypotheses which simplifies the resolution of (1.20). In this context, it is pertinent to consider only sources with a finite radius R – *i.e.* localized sources – seen from a large distance *i.e.* : $R \ll \lambda \ll r$ with λ the gravitational wave wavelength, and

r the distance to the source. This is called the *far-field approximation*. In this case solutions of (1.20) are the classical *retarded potential*,

$$\bar{h}^{\mu\nu}(t,\vec{x}) = \frac{4G}{c^4}\int_{\mathcal{S}} \frac{T^{\mu\nu}(t',x')}{||\vec{x}-\vec{x}'||}d^3\vec{x}' \tag{1.27}$$

where $\vec{x}$ is the spatial position of the observer, $\vec{x}'$ the position of a point belonging to the source $\mathcal{S}$, t' is the retarded time $t' = t - \frac{||\vec{x}-\vec{x}'||}{c}$. Note that in the far-field approximation, one can write $||\vec{x}-\vec{x}'|| \simeq r$.

Since we will compute the results in the TT gauge, we only need to calculate the spatial terms of $\bar{h}^{\mu\nu}$. In the weak-field regime, one can write

$$T^{ij} \simeq \frac{1}{2}\frac{\partial^2}{\partial t^2}(x^i x^j T^{00}) \tag{1.28}$$

an identity which follows from conservation laws. Then one has

$$\bar{h}^{ij} \simeq \frac{2G}{c^4 r}\frac{\partial^2}{\partial t^2}\int_{\mathcal{S}} x'^i x'^j T^{00}(t',\vec{x}')d^3\vec{x}' \tag{1.29}$$

We define the *quadrupole tensor* of the source $\mathcal{S}$,

$$I^{ij}(t) = \int_{\mathcal{S}} x^i x^j T^{00}(t',\vec{x}')d^3\vec{x} \tag{1.30}$$

Hence,

$$\bar{h}^{ij}(t,\vec{x}) \simeq \frac{2G}{c^4 r}\ddot{I}^{ij}(t') \tag{1.31}$$

where a dot means a derivative with respect to t.

We will now project the result into the TT gauge by using the *transverse-traceless projector*: $P^{ij} = \delta^{ij} - n^i n^j$ where $\vec{n} = \frac{\vec{x}}{||\vec{x}||}$ are unit vectors in the $\vec{x}$ direction.

We have: $I^{TT}_{ij} = P_{ik}I^{kl}P_{lj} - \frac{1}{2}P_{ij}P_{kl}I^{kl}$, giving $\bar{h}^{TT}_{ij}$ for a wave moving on the $\hat{n}$ direction

$$\bar{h}^{TT}_{ij} \simeq \frac{2G}{c^4 r}\ddot{I}^{TT}_{ij}(t') \tag{1.32}$$

1.2.3 Properties of gravitational waves

Velocity

From equation (1.21) we showed that the speed of propagation for gravitational waves is c, the speed of light.

Luminosity

Now that we have determined the amplitude of a gravitational wave, it is interesting to use this result to determine the amount of energy carried by such a wave.

The energy of a gravitational wave cannot be defined locally, since the very notion of local energy has no existence in General Relativity. However it is possible to calculate an average energy of a region of space-time big enough to contain several waves' wavelengths, but small enough to be able to define quantities such as tensors integrals.

The gravitational wave flux, or the amount of radiation energy dE passing through an element of area dA during a time dt is related to the stress-energy tensor associated to the wave by the relation

$$\frac{dE}{dAdt} = -\frac{1}{c}T_{00} \tag{1.33}$$

which can be written as

$$\frac{dE}{dAdt} = -\frac{c^3}{32\pi G}\langle \dot{\bar{h}}^{ij}_{TT}\dot{\bar{h}}^{TT}_{ij}\rangle \tag{1.34}$$

Using result obtained in (1.32), we can write

$$\frac{dE}{dAdt} = -\frac{G}{8\pi c^5 r^2}\langle \dddot{I}^{ij}_{TT}\dddot{I}^{TT}_{ij}\rangle \tag{1.35}$$

Integrated over all possible spatial directions, we obtain the *Einstein quadrupole formula*,

$$\frac{dE}{dt} = L_{GW} = \frac{1}{5}\frac{G}{c^5}\langle \dddot{I}_{ij}\dddot{I}^{ij}\rangle \tag{1.36}$$

It is possible to obtain an order of magnitude estimate for this quantity using essential properties of the source. If we admit that the source of spatial extent R, evolving on a time scale T, of mass M, the quadrupolar momentum of the object can be approximated by: $\dddot{I} = \varepsilon \frac{MR^2}{T^3}$ with ε the typical asphericity of I. If we now write $v = R/T$ speed of the object, and $M_S = \frac{2GM}{c^2}$ its Schwarzschild radius, we have approximately

$$L_{GW} \sim \frac{c^5}{G}\varepsilon^2 \left(\frac{R_S}{R}\right)^2 \left(\frac{v}{c}\right)^6 \tag{1.37}$$

An efficient source of gravitational waves must therefore be asymmetric ($\varepsilon \sim 1$), compact ($R \sim R_S$) and relativistic. This formula shows as well that it is impossible to generate a measurable amount of gravitational waves in the lab. Let us assume for a realistic lab source the following characteristics: $\varepsilon = 1$, $R = 1$ m, $v = 300$ ms^{-1} and $M = 10^3$ kg, we obtain $L_{GW} \sim 10^{-14}$ W.

The order of magnitude is completely different with an astrophysical source: a binary system of neutron stars orbiting at 10% of the speed of light generates a power of about 10^{42} W[1].

Polarization

From (1.26) we showed that gravitational waves are transverse waves with 2 degrees of freedom, *i.e.* with two polarization states. In the transverse-traceless gauge, let us consider a plane gravitational wave propagating along the z axis. This choice is pertinent knowing that plane gravitational waves are a good approximation for waves emitted by distant sources.

The amplitude of this wave can be written as

$$\bar{h}^{TT}_{\mu\nu} = \begin{pmatrix} 0 & 0 & 0 & 0 \\ 0 & h_+(t) & h_\times(t) & 0 \\ 0 & h_\times(t) & -h_+(t) & 0 \\ 0 & 0 & 0 & 0 \end{pmatrix} \tag{1.38}$$

[1]The distance to the source impacts detection probability. This issue will be addressed in the next chapters of this thesis.

A wave is said:

- +-polarized when $h_\times(t) = 0$
- ×-polarized when $h_+(t) = 0$
- *Circularly* polarized when $h_+(t) = \pm i h_\times(t)$
- *Elliptically* polarized otherwise.

Effect on test masses

To conclude this introductory chapter on General Relativity and gravitational waves, let us focus on their physical effect on matter, which will help us understand better the design of gravitational-wave detectors.

We consider a circular ring of test masses, arranged in the $z = 0$ plane (see figure 1.1). The spatial separation vector between a test mass and the x axis is: $\vec{\xi} = (\varepsilon\cos\theta, \varepsilon\sin\theta, 0)$ where θ is the angle between the mass and the x axis and ε the radius of the ring.

In the presence of a plane gravitational wave, propagating in the z direction, each particle follows the geodesics equation (1.4). The metric can be written in the transverse-traceless gauge, in the $z = 0$ plane as: $g^{TT}_{\mu\nu} = \eta_{\mu\nu} + \bar{h}^{TT}_{\mu\nu}$ The acceleration between the particles are then:

$$\frac{\partial^2}{\partial t^2}\xi_x = \frac{1}{2}\varepsilon\left(\cos\theta\frac{\partial^2}{\partial t^2}h_+(t) + \sin\theta\frac{\partial^2}{\partial t^2}h_\times(t)\right) \tag{1.39a}$$

$$\frac{\partial^2}{\partial t^2}\xi_y = \frac{1}{2}\varepsilon\left(\cos\theta\frac{\partial^2}{\partial t^2}h_\times(t) - \sin\theta\frac{\partial^2}{\partial t^2}h_+(t)\right) \tag{1.39b}$$

These equations can be integrated to obtain the equation of motion. In figure 1.1 the movement of the test masses is shown depending on the wave's polarization.

1.2.4 Observational evidence

Even if no direct observation of gravitational waves has been performed (yet), strong indirect evidences exist. The binary system PSR B1913+16 was discovered

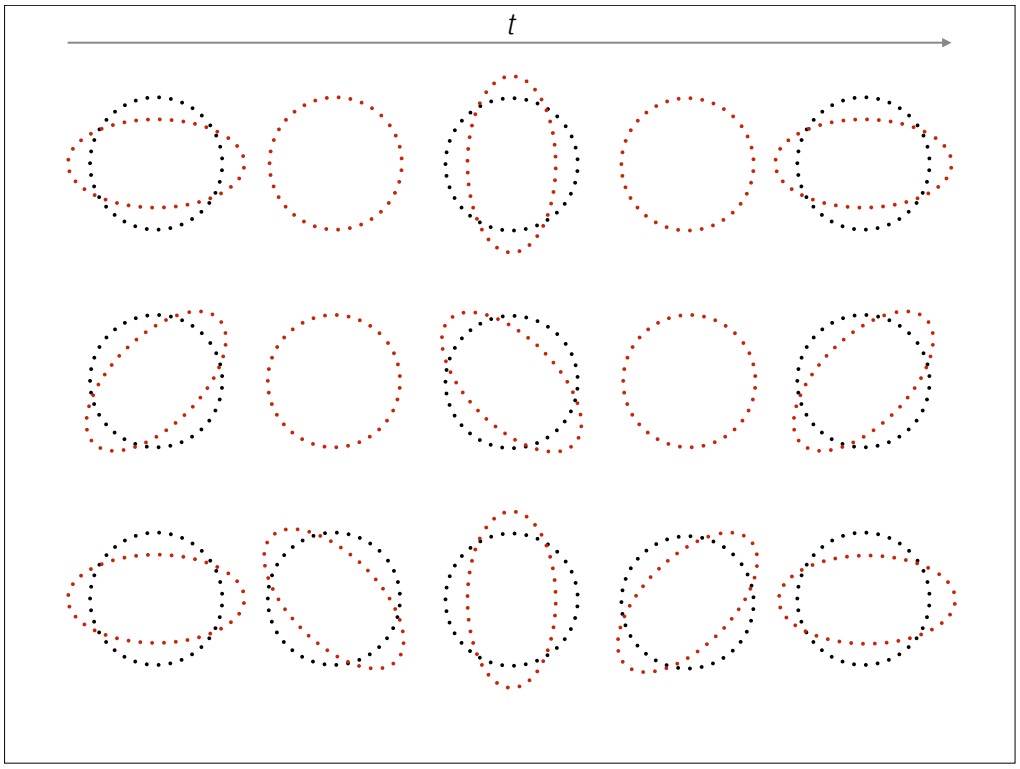

Figure 1.1: The effect of a gravitational wave propagating in the direction orthogonal to the page, depending on its polarization, on a ring of test-masses. The black points mark the initial position of the ring, and the red rings evolve through time from left to right. Top to bottom we present the effect of three different polarizations: $+, \times$ and circular.

by Hulse and Taylor in 1974 [13]. It is composed by a pulsar and an other compact object – presumably another neutron star due to its mass. Its physical characteristics, and especially its orbital period, have been continuously measured ever since. General Relativity predicts that such a system should lose energy *via* emission of gravitational waves. In figure 1.2 is plotted as a function of time, the cumulative shift of the periastron time[2] of the system. This measurement indicates that the period of the PSR B1913+16 binary is decreasing as predicted by General Relativity. Such system should indeed lose energy *via* emission of gravitational waves at rate compatible with observation.

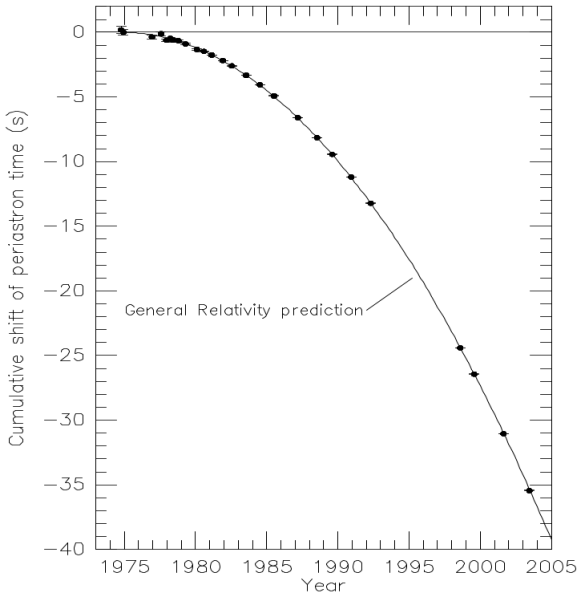

Figure 1.2: Measurement of the PSR B1913+16 system's periastron time cumulative shift from 1975 to 2004 [1]. Points are data with measurement error bars, the continuous curve is the General Relativity prediction.

This result is a strong motivation to pursue the search for direct detection of gravitational waves. Details on this scientific effort are given in the next chapter.

[2]Time between two successive passage of the system at his periastron, *i.e.* at the point where the two members are the closest.

Chapter 2

Gravitational Wave Detectors

"En fait, leur fusée n'était pas très, très au point, mais ils avaient calculé qu'elle avait quand même une chance sur un million de marcher. Et ils se depêchaient de bien rater les 999 999 premiers essais pour être sûrs que le millionième marche."

Les Shadoks

Now that gravitational waves have been properly introduced, let us focus on their detection. In this chapter we will, after a brief historical review, detail the functioning of interferometric detectors – such as the Virgo experiment – and their principal sources of noise. Unless stated otherwise, results exposed hereafter are mainly taken from [14].

2.1 History again

Gravitational waves are, as we seen in the previous chapter, a direct consequence of General Relativity. They can be emitted by any source of matter or energy with an accelerated movement, but are quite faint in the general case. Detectable gravitational waves might be emitted by a very specific class of astrophysical objects which, as we will see in detail in Chapter 3, are uncommon . The probability for such sources to be located in the cosmic neighborhood is weak. Despite the fact that the amplitude of the waves they emit is high, it is likely to be very weak

when they arrives on Earth. Detection experiments must then be extremely sensitive. For years physicists had no confidence that they would ever be detectable.

The first experiment was imagined and constructed by Joseph Weber [15] in the early sixties. It consisted of 1.5 m long bars of metal – aluminum in its first design – with piezo-electric crystals bonded to their surface. This solid bar would be stressed by the passing of a gravitational wave, stress which would be detected by the piezo-electric sensors.

This type of detector is sensitive to a wave with a frequency close the main resonant frequency of the bar, typically around 1000 Hz. This technology has been ameliorated through the years, and at the end of the last millennium, the sensitivity of these detectors, in terms of strain amplitude h, was of $h_{bars} \sim (5-10) \cdot 10^{-22}$ Hz$^{-1/2}$ in a 1 Hz band around 1000 Hz.

In the early seventies, a different approach to gravitational wave detection has been developed independently by Weiss [16] and Forward [17]. Their idea was to measure the distance variation between two pairs of two test-masses using interferometry, more specifically a Michelson interferometer. This apparatus offers, with respect to bar-likes experiment, several advantages – among which a broader sensitivity in frequency, sensitivity being also scaled with the length of the interferometer arm length. Technical progress has made this technology the more likely to give a first detection in the coming years. It is used by the Virgo and LIGO experiments [3, 4]; in the next part of this chapter, we will detail its principles. We will illustrate them using the example of the Virgo experiment and of its early results.

2.2 Detection principle

2.2.1 The Michelson interferometer

A Michelson interferometer consists of a source of light – in our case a laser – passing through a partially reflecting mirror – the *beam splitter* – and reflected on two end-course mirrors located in two orthogonal directions (see figure 2.1).

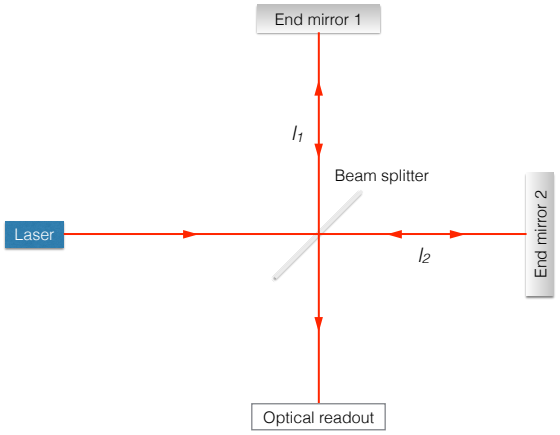

Figure 2.1: The optical scheme of a basic Michelson interferometer. A laser emits a light beam which is divided in two by the beam splitter. The distances between the beam splitter and each end-mirrors are noted l_1 and l_2.

The light reflected by these mirrors converge back to the beam splitter. At the output of the interferometer, the light beams interfere. If one notes I_0 the light intensity of two light beams, then the resulting light intensity at the output of the interferometer is given by the formula

$$I_{output} = 2I_0 \left(1 + \cos\left(2\pi f \frac{\delta l}{c}\right)\right) \tag{2.1}$$

where f is the frequency of the laser, and δl is the difference of distance traveled by the two beams. In absence of external perturbation, for beams traveling in vacuum, $\delta l = 2(l_2 - l_1)$, where l_1 and l_2 are the distances between each end-mirror and the beam-splitter. I_{output} can vary between $4I_0$ and 0 depending on the value of δl. If $I_{output} = 0$, interferences are destructive, and we say the interferometer is set on a *dark fringe*.

2.2.2 Application to gravitational waves detection

The interference pattern obtained depends on the phase difference between the two laser beams. However we know from the previous chapter that gravitational waves affect the "distances" (precisely light travel time) between freely falling masses orthogonal in direction to the propagation direction. This makes the Michelson's interferometer a well suited apparatus to detect this change: supposing that the mirrors of the experiment can be considered as freely falling masses, the distances between them – or the optical path of the light inside the interferometer – will change during the passing of a gravitational wave. This change can be detected at the output of the experiment using photodiodes. In the following we will discuss this mechanism in more details.

2.2.3 The example of Virgo

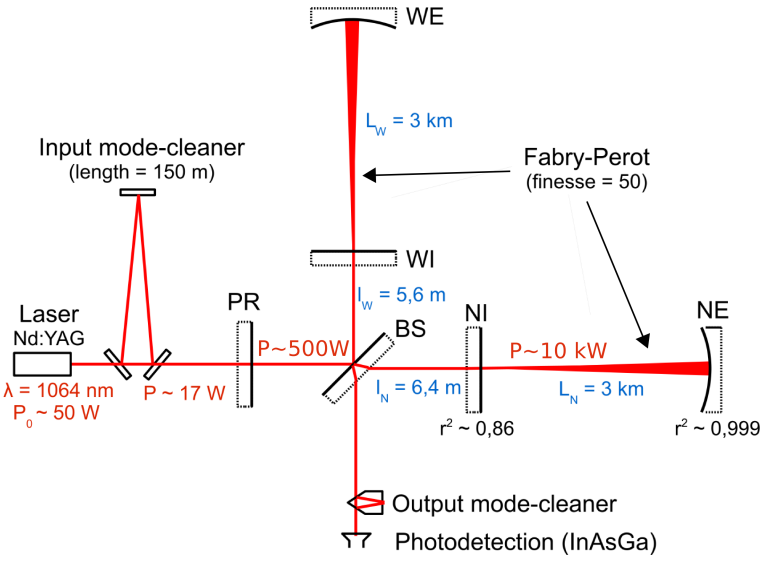

Figure 2.2: The Virgo optical scheme during its second science run, from [18]. (BS) is the beam-splitter, (WE) and (NE) (*resp.* West-End and North-End) are the two end mirrors, (NI) and (WI) the two input mirrors, and (PR) the power-recycling mirror. Solid lines on the mirrors correspond to their reflectively coated sides.

Display in figure 2.2 is a scheme of the Virgo optical scheme as of 2009. Virgo is a Franco-Italian experiment located in Cascina, near Pisa in Italy. It is an interferometric gravitational wave detectors with 3 km long arms. The laser used has a 1.064 μm wavelength. The beam first passes by a mode-cleaner cavity, then by the power rectcling mirror before reaching the beam-splitter. There the output beams are directed toward two 3 km long Fabry-Perot cavities, both formed by an input and an end-mirror. Light exiting a cavity returns to the beam-splitter. There, part of it is directed to the power recycling mirror which returns the light to the interferometer[1] – which increases power stored in the interferometer. The light exiting the interferometer passes by an output mode cleaner before reaching the photo-detector. Note here that the output of the interferometer is set on a dark fringe[2], *i.e.* in absence of perturbation, light interferences are destructive at the level of the photo-diodes.

2.2.4 The phase shift induced by a gravitational wave

Let us consider a simple Michelson interferometer composed only by a laser, a beam-splitter and two end-mirrors (see figure 2.1). The beam splitter is at the center of the reference frame, and the two arms aligned on the x and y axis. A gravitational wave propagates along the z axis. For the sake of simplicity, let us consider it +-polarized.

Now we consider the light propagating in the x arm. The optical path of a photon in the arm of the interferometer can be expressed as

$$L_x = c \int_0^{\tau_{end}} dt + c \int_{\tau_{end}}^{\tau_{BS}} dt \tag{2.2}$$

where τ_{end} is the time where the photon reaches the end of the arm, and τ_{BS} the time where, reflected, comes back to the beam splitter. Knowing that for

[1] Note that to set the interferometer on a dark fringe ensures that more light will be power recycled.

[2] Actually the interferometer is not set exactly on a dark fringe. Reasons why are beyond the scope of this thesis and we won't enter into details.

photons, the infinitesimal displacement in space-time $ds^2 = 0$, we can write:

$$\begin{aligned} ds^2 &= g_{\mu\nu}^{TT} dx^\mu dx^\nu \\ ds^2 &= (\eta_{\mu\nu} + h_{\mu\nu}) dx^2 \\ c^2 dt^2 &= (1 + h_+(t')) dx^2 \end{aligned} \tag{2.3}$$

with $h_{11} = -h_{22} = h_+(t')$, $t' = 2\pi f_{gw} t$, f_{gw} being the wave frequency. Therefore equation (2.2) can be written: $L_x = L_{x_1} + L_{x_2}$ where

$$L_{x_1} = \int_0^{L_{arm}} \sqrt{1 + h_+(t')} dx \simeq \int_0^{L_{arm}} \left(1 + \frac{1}{2} h_+(t')\right) dx \tag{2.4}$$

the binomial expansion of the square root being justified by the expected order of magnitude of $h_+(t')$. Similarly for a photon traveling in the y arm, one can obtain with the same notations,

$$L_{y_1} \simeq \int_0^{L_{arm}} \left(1 - \frac{1}{2} h_+(t')\right) dx \tag{2.5}$$

By doing the same reasoning for the return trip of the photon to the beam-splitter, one obtains:

$$L_x = 2L + \frac{1}{2} \int_0^{L_{arm}} h_+(t') dx - \frac{1}{2} \int_{L_{arm}}^0 h_+(t') dx \tag{2.6a}$$

$$L_y = 2L - \frac{1}{2} \int_0^{L_{arm}} h_+(t') dx + \frac{1}{2} \int_{L_{arm}}^0 h_+(t') dx \tag{2.6b}$$

Now if we consider $2\pi f_{gw} t \ll 1$ during the passage of the wave *i.e.* if $L \ll \lambda_{gw}$ with L the optical path of a photon during the propagation of the wave, and λ_{gw} the wave's wavelength, $h_+(t')$ can be considered constant during the propagation. Then, the difference in optical path between the two arms is

$$L_x - L_y = 2h_+ L \tag{2.7}$$

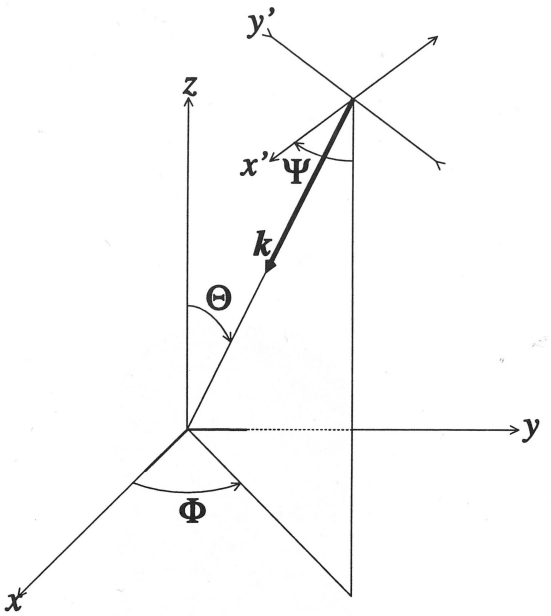

Figure 2.3: Coordinates used to describe antenna patter functions. (x, y, z) is the referential centered on the interferometer, its arms aligned on the x and y axis. (x', y', z') referential define the gravitational waves' polarization. From [19].

from which we can deduce the phase difference

$$\Delta\varphi = 4\pi \frac{L}{\lambda_l} h_+ \tag{2.8}$$

with λ_l the laser's wavelength. This relation teaches us that, as long as $L \ll \lambda_{gw}$, the phase difference at the output of the interferometer is *proportional* to the amplitude of the wave. For Virgo ($L_{arm} = 3$ km), this approximation is valid for waves of wavelength much greater than $L \sim 100$ km[3] *i.e.* of frequency $f_{gw} \ll 3 \cdot 10^3$ Hz. For a more complete treatment of the phase difference without assumption on the wave frequency, see [7] for instance.

We can now define a *gravitational wave signal*,

$$s(t) = h_+(t) = \frac{\lambda_l}{4\pi L} \Delta\varphi \tag{2.9}$$

[3]The optical path of the photons is greater than the arms' length. See section 2.3.2.

With the low frequency hypothesis, it is possible to generalize equation 2.9 for a wave coming from any direction (Θ, Φ) (see figure 2.3), without assumption on its polarization. Details of the calculation can be found in [20]. The result is

$$s(t) = F^{+}(\Theta, \Phi, \Psi)h_{+}(t) + F^{\times}(\Theta, \Phi, \Psi)h_{\times}(t) \tag{2.10}$$

where the F^{+} and $F^{\times}$ are the *antenna pattern* functions,

$$F^{+}(\Theta, \Phi, \Psi) = \frac{1}{2}(1 + \cos^2\Theta)\cos 2\Phi \cos 2\Psi - \cos\Theta \sin 2\Phi \sin 2\Psi \tag{2.11a}$$

$$F^{\times}(\Theta, \Phi, \Psi) = \frac{1}{2}(1 + \cos^2\Theta)\cos 2\Phi \sin 2\Psi + \cos\Theta \sin 2\Phi \cos 2\Psi \tag{2.11b}$$

and where Ψ is the angle between the projection of the x arm onto the plane orthogonal to the direction of propagation and the x' axis, which defines the +-polarization (see figure 2.3).

The interferometer's response to a signal depends on its origin in the sky. It is null along the bisector between the arms of the apparatus, and at directions which satisfy $F^{+}(\Theta, \Phi, \Psi)h_{+}(t)+F^{\times}(\Theta, \Phi, \Psi)h_{\times}(t) = 0$. Displayed in figure 2.4 is plotted the quantity $\sqrt{F^{+}_{mean}(\Theta, \Phi)^2 + F^{\times}_{mean}(\Theta, \Phi)^2}$, with $F^{+,\times}_{mean}(\Theta, \Phi)$ averaged values of $F^{+,\times}(\Theta, \Phi, \Psi)$ over all the polarization angles Ψ. This quantity represents the sensitivity of an interferometer averaged over all gravitational waves' polarizations.

This pattern is roughly isotropic, which means that with a single interferometer, it is impossible to determine precisely the source of a signal. To achieve spatial reconstruction of sources (among other parameter estimations), triangulation between different detectors is necessary.

2.3 Noise sources

2.3.1 Generalities

At the output of the interferometer, the phase difference between the two beams reflected by the cavities is evaluated with a light intensity measurement. Indeed,

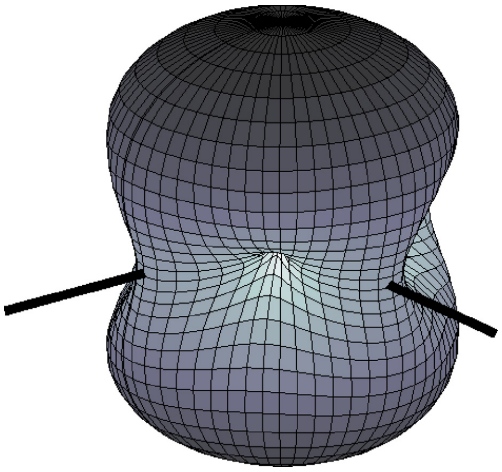

Figure 2.4: Sensitivity of an interferometric detector depending on source location, averaged over all polarization states [19]. The bars represent the arms of the interferometer.

the phase difference determines the interference pattern, the evolution of which is evaluated measuring light intensity variation at the level of a specific fringe *via* equation (2.1) – in Virgo the measure is done on a *dark fringe*.

Correctly calibrated, the signal of the photo-diodes is proportional to the gravitational wave signal $h(t)$ in the absence of noise. This signal is called the *detector strain* time series,

$$d(t) = F^{+}(\Theta, \Phi, \Psi)h_{+}(t) + F^{\times}(\Theta, \Phi, \Psi)h_{\times}(t) + n(t) \tag{2.12}$$

where $n(t)$ is the noise term.

Using equation (2.8), for a laser with $\lambda_l = 1.064$ μm of power $P_0 \sim 10$ W and arms of length $L = 3$ km, one obtains for a gravitational wave of dimensionless amplitude $h_+ = 10^{-21}$: $\Delta\varphi \simeq 10^{-11}$ rad. To understand – and possibly suppress – the noise is therefore one the most important aspects of gravitational waves detector design.

Noise sources can be classified into three main categories:

- *Fundamental* noises, due to the physical processes involved in the measurement,
- *Technical* noises, due to the equipment itself (laser power fluctuation...),
- *Environmental* noises, due to external perturbation of the experiment (seismic noise, bad weather conditions, airplanes...).

The noise reduction work has multiple goals: reducing the impact of the environmental noise with the relevant attenuation devices, improving the design of the experiment to reduce or suppress technical noise etc... A review of Virgo noise characterization work can be found in [21]. Here we will simply introduce the main sources of noise, environmental and fundamental, for an interferometer such as Virgo. We again refer to [21] for a review about technical sources of Virgo noise.

2.3.2 Fundamental sources

Power Spectral Density

Before going further, it is useful here to introduce a quantity used to characterize spectral properties of noise, the *power spectral density* [14].

If we consider random process $s(t)$, let us note

$$C_i(\tau) = \lim_{T\to+\infty} \frac{1}{T} \int_{-T/2}^{+T/2} s(t)s(t-\tau)dt \tag{2.13}$$

the autocorrelation of the process s with a time-delay τ. It is possible to take the Fourier transform of this quantity,

$$P_s^{two\text{-}sided}(f) = \frac{1}{\sqrt{2\pi}} \int_{-\infty}^{+\infty} C_i(t)e^{-2i\pi ft}dt \tag{2.14}$$

which is called power spectral density with $f \in]-\infty;+\infty[$. This spectrum can be seen as a measure of the amount of time variation in $s(t)$ that occurs with

frequency f. When $s(t)$ is a Gaussian stationary process, the power spectral density characterizes completely $s(t)$.

The power spectral density is in practice estimated on finite time segments as

$$P_s^{two\text{-}sided}(f) = \frac{1}{T_0\sqrt{2\pi}} \left(\int_0^{T_0} s(t) e^{-2i\pi ft} dt \right)^2 \tag{2.15}$$

Since $s(t)$ is real, it is possible to define a *one-sided power spectral density*, which considers only positive frequencies,

$$P_s(f) = \begin{cases} 2P_s^{two-sided}(f), \text{ if } f \geq 0 \\ 0, \text{ otherwise} \end{cases} \tag{2.16}$$

Finally one can define the *amplitude spectral density*,

$$A_s(f) = \sqrt{P_s(f)} \tag{2.17}$$

expressed in $[s]^2\text{Hz}^{-1/2}$ if $[s]$ is the unity of $s(t)$. This amplitude is used to describe detector noise, among other things because it is easier to compare to gravitational wave total energy.

Shot noise

Fundamental sources of noise come from the physics involved in the measurement. The main fundamental source of noise is the *shot noise*.

Let us remind here that the physical channel of an interferometric detector is a light power measurement. From a quantum point of view, the laser beam can be considered as a bunch of photons carrying each a quantum of energy $\frac{2\pi\hbar c}{\lambda_l}$ where $\hbar$ is the reduced Planck constant, c the speed of light and λ_l the laser wavelength. A light power measurement is nothing else in this context than a simple "photon counting", which is subject to a statistical error $\sqrt{N}$, N being the mean number of detected photons.

The output power of an interferometer depends on the phase difference $\Delta\varphi$ between its two arms as

$$P_{out} = P_{in} \sin^2 (\Delta\varphi/2) \tag{2.18}$$

If one writes $\Delta\varphi = \alpha + \pi + \sigma_\varphi$ with α a tuning parameter[4], and σ_φ a phase shift (due to noise or signal), with $\sigma_\varphi \ll 1$ one can approximate equation (2.18) by

$$P_{out} \simeq P_{in} \left[\sin^2 \left(\frac{\alpha}{2} \right) + \frac{1}{2} \sin(\alpha) \sigma_\varphi \right] \tag{2.19}$$

The number of photons counted per unit of time $n = N/\tau$ follows a Poisson distribution, and has a probability distribution of: $p(n) = \frac{\langle n \rangle^n e^{-\langle n \rangle}}{n!}$ with $\langle N \rangle$ the mean number of the process. For an average output power P_0, the number of photons counted during a time τ is on average

$$\langle N \rangle = \frac{\lambda_l \tau}{2\pi\hbar c} P_0 \tag{2.20}$$

The standard deviation associated with this measurement is $\sigma_N = \sqrt{\langle N \rangle}$. In terms of power, it becomes

$$\langle P \rangle = P_0 \qquad \sigma_P = P_0 \frac{\sigma_N}{\langle N \rangle} = \sqrt{P_0 \frac{2\pi\hbar c}{\lambda_l \tau}} \tag{2.21}$$

Power standard deviation can be associated with the phase shift standard deviation σ_φ in equation (2.19)

$$\sigma_P = \frac{P_{in}}{2} \sin(\alpha) \sigma_\varphi \tag{2.22}$$

Hence,

$$\sigma_\varphi = \frac{2}{P_{in} \sin(\alpha)} \sqrt{P_0 \frac{2\pi\hbar c}{\lambda_l \tau}} \tag{2.23}$$

[4]Which has for optimal value $\alpha = 0$, see (2.24).

In the absence of gravitational wave, using equation (2.18), the output power is $P_0 = P_{in} \sin^2\left(\frac{\alpha}{2}\right)$. Therefore,

$$\sigma_\varphi = \frac{1}{\cos\left(\frac{\alpha}{2}\right)} \sqrt{\frac{2\pi\hbar c}{P_{in}\lambda_l \tau}} \tag{2.24}$$

σ_φ is minimized when $\alpha = 0$. Using equation (2.9) it is straightforward to convert the phase standard deviation in terms of gravitational wave amplitude spectral density (see [14] and references within for more details):

$$h_{shot}(f) = \frac{1}{L} \sqrt{\frac{c\hbar\lambda_l}{4\pi P_{in}}} \tag{2.25}$$

In the case of Virgo, with a laser of power $P_{in} = 20$ W, we have: $h_{shot} \sim 4 \times 10^{-21}$ Hz$^{-1/2}$. To lower this noise, we can clearly see two courses of action: to increase the laser power, or to increase the arms' length. These two means are used in Virgo. To understand how it is done, it is necessary to take into account two elements of the Virgo optical scheme (figure 2.2) that we did not consider so far. First, a power recycling mirror (PR) is placed before the beam splitter in order to reinject in the interferometer the power coming back from the beam splitter – this is possible because the interferometer is tuned at a dark fringe. The power added to interferometer increases P_{in} by a factor $g_{rec} \sim 30$. Then, two inputs mirrors – (WI) and (NI) on the scheme – form Fabry-Perot cavities with the end mirrors. These cavities, when correctly tuned, increase significantly the optical path to about $L_{opt} \sim 100$ km [5].

Let us do the math: considering an ideal Fabry-Perot cavity, without any loss. The first mirror possesses a reflectivity $r \sim 0.94$ and a transmittance t such as $r^2 + t^2 = 1$. We consider that the end mirror has a perfect reflectivity $r_{end} = 1$. An electromagnetic field E_0 enters the cavity. We are interested in $E_{exit} = RE_0$ the value of the field reflected by the cavity. This field is composed by the field immediately reflected by the first mirror of the cavity, and by all the fields reflected n inside the cavity and transmitted through the input mirror (see

[5] We have $L_{opt} \sim \frac{2\mathcal{F}}{\pi} L$ with $\mathcal{F}$ the *finesse* of the cavity: $\mathcal{F} = \frac{\pi\sqrt{r r_{end}}}{1 - r r_{end}}$ with our notations.

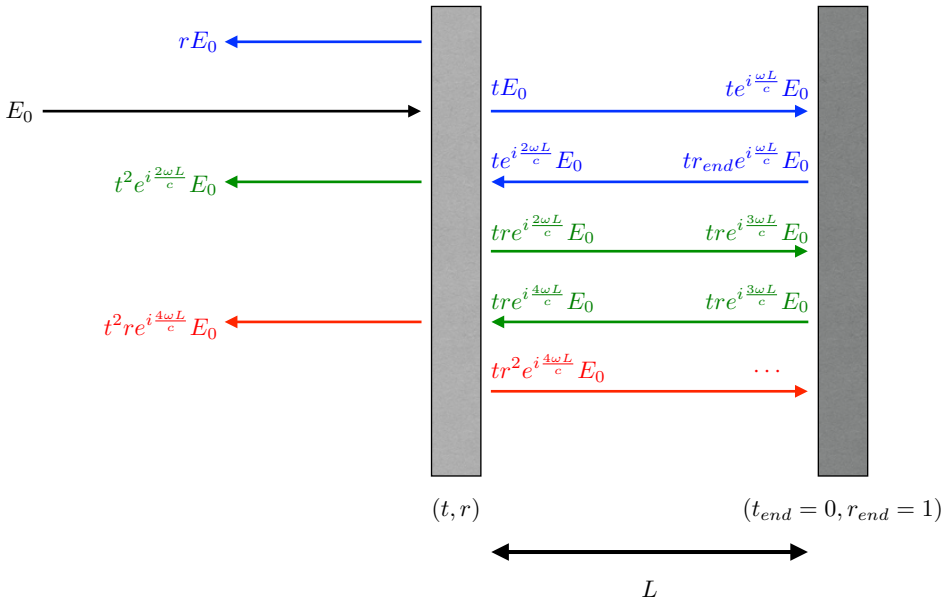

Figure 2.5: Scheme of the light path inside a Fabry-Perot cavity. Light amplitude is indicated at several points of light's trip in the cavity. Light rays represented are physically superposed. For understanding purposes they have been separated.

figure 2.5). If we denote L the length of the cavity and ω the angular frequency of the electromagnetic field, we have:

$$E_{exit} = RE_0 = E_0\left(-r + te^{i\frac{2\omega L}{c}}t + te^{i\frac{2\omega L}{c}}re^{i\frac{2\omega L}{c}}t + \dots\right) \tag{2.26a}$$

$$= E_0\left(-r + t^2\sum_{n=1}^{+\infty} r^{n-1}e^{i\frac{2\omega L}{c}n}\right) \tag{2.26b}$$

We have consequently

$$R = -r + \frac{t^2e^{i\frac{2\omega L}{c}}}{1 - re^{i\frac{2\omega L}{c}}} = \frac{-r + e^{i\frac{2\omega L}{c}}}{1 - re^{i\frac{2\omega L}{c}}} \tag{2.27}$$

Assuming the cavity length, in absence of any signal, is tuned to be a multiple of half the wavelength of the laser: $L = n\frac{\lambda_l}{2}$, we have $e^{i\frac{2\omega L}{c}} = 1$. The laser light is in *resonance* within the cavities. The reflectivity of the cavity is then $R = 1$. In presence of a signal, we can write

$$\frac{2\omega L}{c} = \frac{2\omega L_0}{c} + \varphi(t) \tag{2.28}$$

with $\varphi(t)$ the phase change induced by the gravitational wave signal, and L_0 the unaltered length of the cavity. For extremely small phase shifts, we have

$$R = \frac{e^{i\varphi(t)} - r}{1 - re^{i\varphi(t)}} \simeq \frac{1 - r + i\varphi(t)}{1 - r - ir\varphi(t)} \tag{2.29}$$

The output phase of the laser beam exiting the cavity $\arg(RE_0) = \arg(R)$ is then

$$\arg(R) = \tan\left(\frac{\varphi(t)}{1-r}\right) - \tan\left(\frac{-r\varphi(t)}{1-r}\right) \simeq \frac{1+r}{1-r}\varphi(t) \tag{2.30}$$

The phase difference between the two arms is then multiplied by $\frac{1+r}{1-r} \sim 30$ in the case of Virgo. Using equation (2.8) we can interpret this amplification as an increase of the optical path L.

The previous calculations assume that the arm lengths are constant during the whole process. However this assumption is correct only when no gravitational wave is present. When considering gravitational waves of wavelength larger than to the effective optical path of the photons inside the cavity *i.e.* waves of frequency less than the inverse of the cavity storage time $1/\tau_s \sim \frac{1-r}{1+r}\frac{c}{2L}$, assuming constant arm lengths is a good enough approximation. The calculations which includes arms length variation are quite complex [22]. When we take into account this variation, a frequency dependency of the output phase of the laser appears and we have

$$\arg(R) = \frac{1+r}{1-r}\frac{1}{\sqrt{1+\frac{f^2}{f_c^2}}}\varphi(t) \tag{2.31}$$

where $f_c = \frac{c}{2\pi L}\frac{1-r}{2\sqrt{r}} \sim 500$ Hz the high frequency cut-off. As a result of all these calculations, the shot noise spectral amplitude becomes

$$h_{shot}(f) = \frac{1}{L_0}\sqrt{\frac{c\hbar\lambda_l}{4\pi g_{rec} P_{in}}}\frac{1-r}{1+r}\sqrt{1+\frac{f^2}{f_c^2}} \tag{2.32}$$

which in the case of Virgo yields $h_{shot}(f) \sim 2 \times 10^{-23}\sqrt{1+\frac{f^2}{f_c^2}}$ Hz$^{-1/2}$.

Thermal noise

Another fundamental source of noise which is important to describe here is the *thermal noise*. Indeed all materials used undergo fluctuations due to the Brownian motion of the mechanical degrees of freedom. In the frequency range $10 - 1000$ Hz, the dominant fluctuations come from the mirror surfaces and the thermal excitation of the pendular motion of the wires. These effects can be modeled using the internally damped oscillator's motion equation (2.40), considering only an effective external Brownian force F_{th},

$$m\left(\omega_0^2 - \omega^2 + \omega_0^2\frac{i}{Q}\right)x(\omega) = \chi(\omega)x(\omega) = F_{th}(\omega). \tag{2.33}$$

In this case the fluctuation-dissipation theorem [23] teaches us that the effective thermal force F_{th} has a one-sided power spectral density of

$$F_{th}^2(\omega) = \frac{4k_B T}{\omega}\mathrm{Im}(\chi(\omega)) \tag{2.34}$$

with k_B the Boltzmann constant and T the temperature. The position fluctuation spectral density is then [24]

$$\sqrt{x^2(\omega)} = \frac{\sqrt{F_{th}^2(\omega)}}{|\chi(\omega)|} = \frac{\omega_0^2}{\sqrt{(\omega_0^2-\omega^2)^2 + \frac{\omega_0^4}{Q^2}}}\sqrt{\frac{\omega_0}{\omega}}\sqrt{\frac{4k_B T}{mQ\omega_0^3}} \tag{2.35}$$

To decrease it we see that we need to use materials with a high quality factor for the mirrors and the pendulum. Increasing the value of Q in (2.35) concentrates the noise around the resonance ω_0, and reduces it everywhere else.

Translated into gravitational wave strain amplitude, we obtain for mirrors of mass $m = 20$ kg and quality factor $Q = 5 \times 10^5$, we have:

$$h_{therm}(f) = \frac{2}{L_0}\sqrt{x^2(f)} \sim 1.7 \times 10^{-18} \left(\frac{1\ \mathrm{Hz}^{3/2}}{f_0 f^{1/2}}\right) \mathrm{Hz}^{-1/2} \qquad \text{for } f \ll f_0 \tag{2.36a}$$

$$\sim 1.7 \times 10^{-18} \left(\frac{f_0 \times 1\ \mathrm{Hz}^{3/2}}{f^{5/2}}\right) \mathrm{Hz}^{-1/2} \qquad \text{for } f \gg f_0 \tag{2.36b}$$

where the factor 2 comes from the quadratic sum of the contributions of the 4 mirrors forming the Fabry-Perot cavities.

For the pendulum motion of the mirrors, the main oscillation mode is $f_0 \simeq 0.6$ Hz, and the first internal eigen-mode of the mirrors – characterizing surfaces's fluctuation – is around $f_0 \simeq 5.7$ kHz. In the frequency band $10 - 1000$ Hz, the pendulum modes are described by equation (2.36b), and surface modes by equation (2.36a).

2.3.3 Environmental sources

Environmental sources are exterior to the experiment. They are various in nature: we can cite for instance the lightning which provoke magnetic perturbations. There is also the *gravitational gradient noise*, caused by density fluctuations of the ground surrounding the experiment, accelerating the mirrors through classical Newtonian force.

However the main environmental noise affecting the measurement is seismic noise. It has multiple origins, due to both natural processes and human activities. On the Virgo site [25], the displacement spectral density roughly follows

$$x(f) = 10^{-7} \left(\frac{1\mathrm{Hz}}{f}\right)^2 \ \mathrm{m/Hz}^{1/2}, \ \text{for } f > 10 \text{ Hz} \tag{2.37}$$

The movement this noise would induce on the mirrors is far to great compared to the sensitivity we want to achieve. Indeed, such a noise gives an equivalent gravitational wave signal amplitude of about

$$h_{seismic} \sim \frac{x(t)}{L} \sim 7 \times 10^{-11} \left(\frac{1 \text{ Hz}}{f} \right)^2 \tag{2.38}$$

with L length of one interferometer arm [6]. At 10 Hz, we want to achieve $h \sim 10^{-21}$ Hz$^{-1/2}$ in order to make a detection (see Chapter 3). We must damp the noise by about ten orders of magnitude.

To attenuate vibrations at the mirror level, the simplest thing to do is to attach them to a *pendulum*. To better understand why, let us write the one-dimension equation of motion of a mass m attached with a spring of constant k to the ground, with x_g the reference position of the ground and x the position of the mass, one obtains

$$\ddot{x} + k(x - x_g) = F \tag{2.39}$$

with F the sum of all external forces – except the spring restoring force. For small oscillations with respect to the length of the pendulum, this equation is a good approximation of the pendulum movement equation in the horizontal direction. In the framework of gravitational wave experiments, the system is in vacuum, so the damping due to fluid friction is negligible. Internal friction in the spring is the dominant damping factor, modeled by a spring constant $k(1 + i\phi)$ in the frequency domain [24], with ϕ a constant and small "loss angle" which represents the phase lag between the applied external force and the response of the spring.

Replacing $x(t)$ by $x(\omega)e^{i\omega t}$, we can write (2.39) in the frequency domain. After some straightforward calculations, we get

$$\left(\omega_0^2 - \omega^2 + \omega_0^2 \frac{i}{Q} \right) x = \frac{1}{m} F(\omega) + x_g \omega_0^2 \left(1 + \frac{i}{Q} \right) \tag{2.40}$$

with $Q = \frac{1}{\phi}$ the quality factor and $\omega_0^2 = \frac{k}{m}$.

If we consider only the ground motion term in (2.40) – in other words if we focus only on seismic noise –, we can deduce the amplitude transfer function of the spring,

$$T(\omega) = \left| \frac{x(\omega)}{x_g(\omega)} \right| = \frac{\omega_0^2 \sqrt{1 + \frac{1}{Q^2}}}{\sqrt{(\omega_0^2 - \omega^2)^2 + \frac{\omega_0^4}{Q^2}}} \tag{2.41}$$

For $Q \gg 1$, it is possible to approximate this function in the three following cases:

$$T(\omega) \simeq 1 \qquad \text{if } \omega \ll \omega_0 \tag{2.42a}$$

$$T(\omega) \simeq Q \qquad \text{if } \omega = \omega_0 \tag{2.42b}$$

$$T(\omega) \simeq \frac{\omega_0^2}{\omega^2} \qquad \text{if } \omega \gg \omega_0 \tag{2.42c}$$

With an harmonic oscillator, the seismic noise is therefore suppressed at high frequencies, and amplified around the resonant frequency ω_0. The same equations apply to the case of the pendulum, as long as its oscillation angle is small, in the horizontal direction.

Given these results, we can deduce that with a single pendulum, with a high quality factor Q and a resonant frequency as low as possible (typically around 1 Hz), seismic noise as calculated in (2.37) can be reduced by a factor $\frac{\omega_0^2}{\omega^2}$ at frequencies above the resonant frequency, *i.e.*

$$x(f) \simeq 10^{-7} \left(\frac{1\text{Hz}}{f} \right)^4 \text{ m/Hz}^{1/2}, \text{ for } f > 10 \text{ Hz} \tag{2.43}$$

This effect is still not sufficient, but it is possible to make it even better by using a chain of pendulums. Their transfer functions can be approximated by $\left(\frac{\omega_0^2}{\omega^2}\right)^N$ with N the number of stages considered in the chain.

It is the system chosen in the Virgo experiment: each mirror is suspended to a *superattenuator*, which is basically a five-stage pendulum supported by an inverted pendulum (see figure 2.6) [26]. Each of the pendulums masses is in fact a mechanical filter designed, among other things, to attenuate vertical vibration

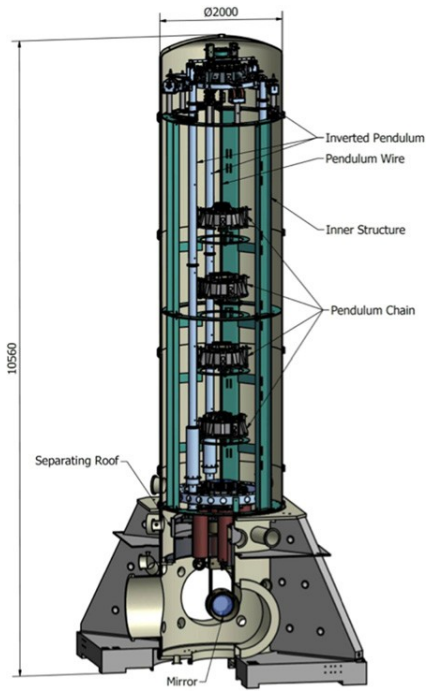

Figure 2.6: Rendering of the Virgo superattenuator [19].

modes – which couple to horizontal modes. Resonant frequencies of the structure are all below 2 Hz, which is well below the intended Virgo sensitive band 10 Hz – 10 kHz [27].

Optics are not free in the vertical direction, but above the pendulum frequency (600 mHz), mirrors can be considered free in the horizontal direction. Indeed if we come back to equation (2.40) considering only the external forces, we find that at high frequencies ($\omega \gg \omega_0$):

$$\frac{1}{m}F(\omega) \simeq -\omega^2 x(\omega) \tag{2.44a}$$

$$\frac{1}{m}F(t) \simeq \ddot{x}(t) \tag{2.44b}$$

which is the equation of a mass only subject to F. In other words, in absence of external forces, the pendulum mass can be considered free at high frequencies. In our case, the mirrors are free in the horizontal direction for frequencies above

a few Hz, which is a mandatory requirement for any measurement related to space-time metrics.

All things considered, with a five stage pendulum, it is possible to achieve a seismic noise reduction of about 14 orders of magnitude in the Virgo sensitive band (see figure 2.7). At 10 Hz we achieve [27]

$$x(f) \sim 10^{-22} \text{ m/Hz}^{1/2} \tag{2.45}$$

which corresponds to a signal amplitude of about: $h_{seismic} \sim 10^{-25}$ Hz$^{-1/2}$, and lower above 10Hz.

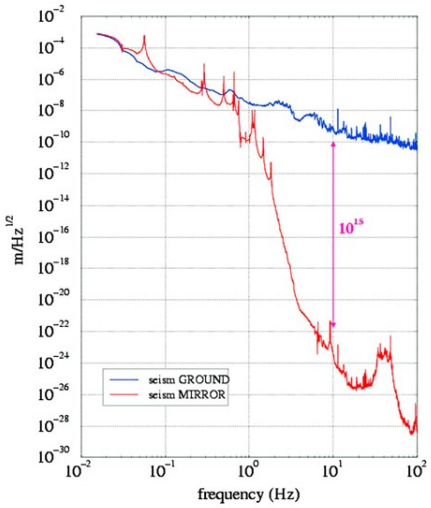

Figure 2.7: Seismic noise spectrum at Virgo in blue, and transmitted noise spectrum using the superattenuator in red [19].

2.3.4 Final sensitivity

From the previous calculations, it is possible to construct a theoretical *noise budget*, a predicted amplitude spectral density of the noise term $n(t)$. It describes at each frequency the sensitivity of the interferometer considering the noise sources we studied. It is simply the quadratic sum of the noises which have been studied. The seismic noise dominates at frequencies lower to 10 Hz, thermal noise

dominates from ten to a few hundred Hz, and shot noise dominates above 1 kHz. This theoretical budget is present in figure 2.8.

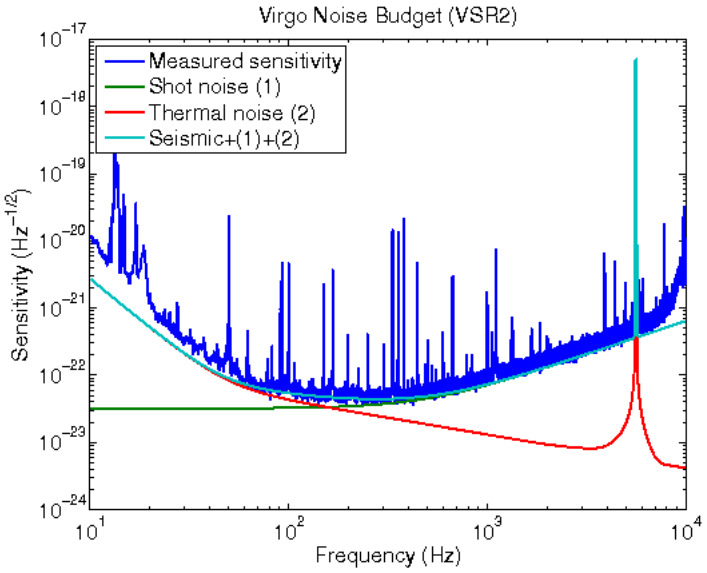

Figure 2.8: Noise budget for Virgo, using theoretical predictions (green, red and cyan curves) and a real sensitivity curve (blue) obtained during the second science run of Virgo during a calm day [28]. The seismic noise, while included in the cyan curve, is totally negligible in this frequency range.

A real noise budget for Virgo is also displayed in figure 2.8. It was taken during its second science run (VSR2). Some contributions here have not been detailed within this chapter. For instance we did not mention technical noises, such as laser power fluctuations, or scattered light, which can dominate the noise at the frequencies of interest. A significant number of fundamental sources has not been described, but the features we developed in this chapter are sufficient to get a global understanding of Virgo sensitivity. It can be seen, however, than the sum of known noises contributions approximates nicely the measured noise.

Finally a sensitivity curve does not give all the information about transient noises (or *glitches*), short power excesses which can appear in the dark fringe, and can be due to a large number of material failures and environmental perturbations. They can seriously affect the efficiency of the signal search, because

their characteristics are similar to signals. This is especially true for the long transient search that we present later in this thesis. In figure 2.9, a selection of such power excesses in the dark fringe channel is shown. They are presented in time-frequency maps, where their amplitude spectrum is plotted in function of time.

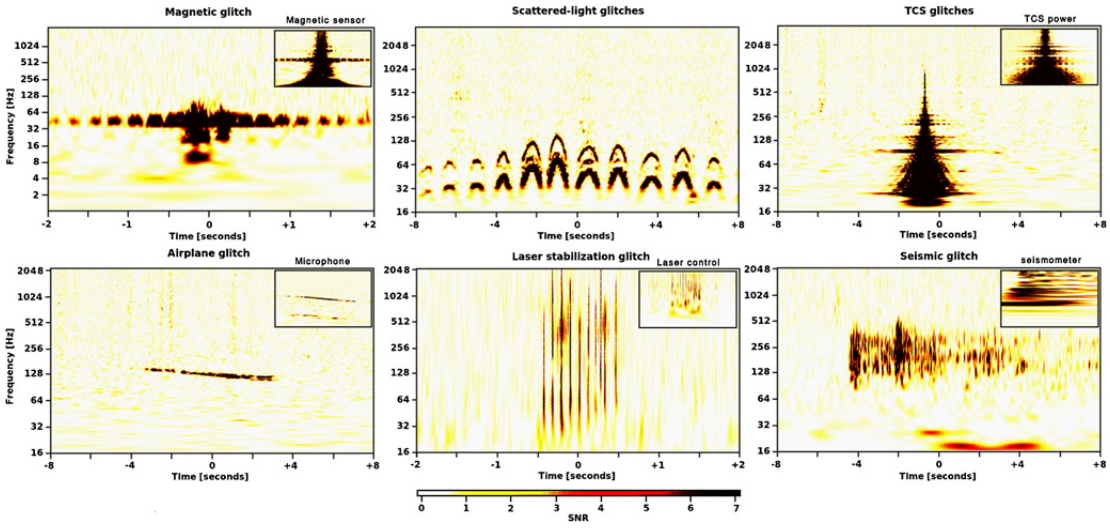

Figure 2.9: Selection of dark fringe glitches represented in time-frequency maps [21].

As it can be seen, the glitches can be several seconds long and could be misidentified as gravitational wave long transient (see chapter 3). Identifying these glitches is an important part of any data analysis process. See [21] for more details about glitches and data quality studies.

2.4 The LIGO-Virgo network

The LIGO interferometers are two inteferometric gravitational waves detectors, like Virgo. They are located in the U.S.A., in Hanford[6] (Washington) and Liv-

[6]A second interferometer, of 2 km long arms, was also present at Hanford, sharing the same facility with the 4 km experiment. In October 2007 the choice was made not to use it any longer.

ingston (Louisiana). Their design is essentially similar to Virgo's, the main difference being the arms length, which is 4 km for both LIGO detectors.

Together, these three observatories form a detector network, which is a crucial feature for gravitational waves detection. We discussed in section 2.11 the antenna factors of an interferometric detector. With a single interferometer, even a powerful gravitational wave emission can be missed if it happens in a zone where the detector response is null. The LIGO experiments have different orientations with respect to Virgo, and very different locations on the Earth. Therefore, their antenna factors are different (see figure 2.10) and the entire sky is covered at any time.

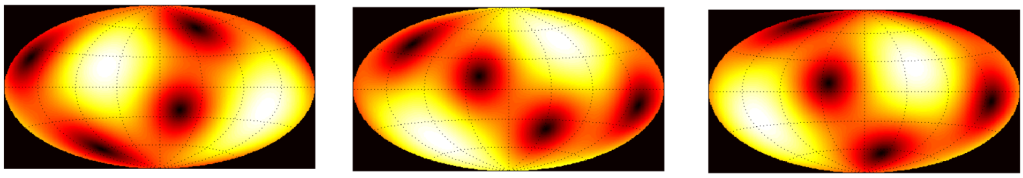

Figure 2.10: Antenna patterns, from left to right, of Virgo, LIGO-Hanford and LIGO-Livingston experiments, at the same time. The maps use the galactic coordinates system. Areas of low sensitivity are dark, areas of optimal sensitivity are white.

A network of interferometers also allows for the spatial reconstruction of a gravitational wave source. Indeed, we showed in 2.2.4 that an interferometer cannot locate the localization in the sky of a signal. With using the data of several experiments though, this is possible with triangulation. When a signal is detected by two or more detectors, depending on the provenance of the signal, this detection won't happen simultaneously in all the experiments. The delay between the detection times in each interferometer depends only on the localization of the source, and can be used to determine it. This delay varies from 0s to a maximal value which is the light time travel between two detectors (see table 2.2). We introduce in table 2.1 the standard abbreviations used in the collaboration to designate each interferometer.

Finally, using a network of interferometers is also a good way to reject false alarms. Indeed, a signal detected simultaneously in two or more detectors is

LIGO-Hanford - 4 km	H1
LIGO-Hanford - 2 km	H2
LIGO-Livingston	L1
Virgo	V1

Table 2.1: Usual abbreviations for detectors

Interferometers pairs	H1L1	L1V1	V1H1
Light time travel	10 ms	26 ms	27 ms

Table 2.2: Light time travel between the different interferometers of the LIGO-Virgo network.

much more significant than a signal detected in only one detector. Several search pipelines combine results from multiple interferometers, this will be the case of the one presented in this thesis.

Chapter 3

Gravitational Wave Sources

"In the beginning the Universe was created. This has made a lot of people very angry and been widely regarded as a bad move."

Douglas Adams

3.1 What is a good gravitational wave source?

In the first chapter we established that a powerful gravitational waves emitter must have three characteristics: it must be compact, it must possess a high velocity, and it must be asymmetric (see equation (1.37)). In addition to the raw luminosity emitted by such bodies, it is important for a detection to be made that the frequencies of the signals be in the detection band of the interferometers. As we have seen in chapter 2, an experiment such as Virgo reaches its maximal sensitivity at frequencies between 10 Hz and 10 kHz, the maximum being reached around 100 Hz for LIGO and 250 Hz for Virgo.

Astrophysical sources of gravitational waves must also be located close enough to us so that the amplitude of the waves they emit – which decreases like the inverse of the distance – is still observable. And within this reach the sources must be numerous enough so the observable event rate is compatible with the observation time of the different experiments.

Gravitational waves sources can be classified in four categories [8]:

- *Continuous* sources, which emit gravitational waves for a duration much longer than the observation time and typically at a constant frequency.

- *Compact binary coalescences*, merging of two compact bodies such as neutron stars and black holes.

- The *stochastic background* which is composed of the superposition of gravitational waves produced by localized sources in the local universe, and of a cosmological background of gravitational waves emitted during the inflation.

- *Transient sources*, which emit signals of duration much shorter than the observation time.

In this chapter, we will review the main gravitational waves sources belonging to each of the categories which are plausible candidates for detection by ground-based interferometers. We will focus our attention on long duration transient sources, for which detection is the subject of this thesis.

Before going further, it is convenient to define the *root square sum* amplitude of a wave, defined as

$$h_{rss} = \sqrt{\int_0^{t_s} h^2(t)dt} = \sqrt{\int_0^{+\infty} \tilde{h}^2(f)df} \tag{3.1}$$

with t_s the duration of the signal, $h(t)$ its amplitude and $\tilde{h}(f)$ its Fourier transform. This quantity, usually expressed in $\mathrm{Hz}^{-1/2}$, can be directly compared to the amplitude spectral density of an interferometer (its *sensitivity*) and hence used to determine whether a signal – given its waveform – is powerful enough to be detected.

3.2 Continuous sources

A source of continuous gravitational waves emits for a duration longer than the observation time, at a near constant frequency. They are usually rotating systems with a stable rotational motion and a steady frequency [8].

A continuous source of gravitational waves could be neutron stars (either isolated or member of a binary system). To be emittors of gravitational waves, there are two possibilities. First, their matter distribution is non-axisymmetric, due to a deformation of their crust – a *mountain*. It is predicted that neutron star structure can support a deformation of about 1 cm over a typical radius of 10 km. In this case the emitted gravitational waves will have a frequency 2ω, where ω is the rotation frequency.

A second possibility is for the neutron star to precess, *i.e.* to have a rotational axis different from its symmetry axis. In that case waves will produced at both ω and 2ω frequencies.

Observable gravitational waves sources should therefore have a rotation period of a few milliseconds to emit waves in the detectable band of ground-based experiments. Such neutron stars are either young neutron stars – like the Crab and the Vela pulsars – or old neutron stars which have been spun-up *via* matter transfer from another body.

These signals can be theoretically detected even if their amplitude is less or comparable with the noise amplitude in the interferometers. Their signal being quasi-monochromatic (the rotation frequency of a neutron star decreases over time with a rate $\dot{\omega}$), a power excess can appear if the data are integrated over a sufficiently long period of time.

The detail of the searches depends however of the knowledge we possess on the potential source. For known pulsars, such as the Vela and the Crab pulsar, ω, $\dot{\omega}$ and their sky position are known *via* constant radio surveys (see table 3.1 for numerical values). A very precise model of the gravitational waves received at Earth-level can be made, and therefore efficient searches lead (*targeted searches*) [29]. In the case where only the source position is known, a greater parameter

space must be investigated, since neither ω or $\dot{\omega}$ are known (*directed searches*). Finally, it is possible, but computationally costly, to search for unknown pulsars.

	Crab pulsar	Vela pulsar
Period P (ms)	33.1	89.3
Period first derivative $\dot{P}$ (unitless)	$4.23 \cdot 10^{-13}$	$1.25 \cdot 10^{-13}$
Rotation frequency ω (Hz)	30.23	11.19
Rotation frequency first derivative $\dot{\omega}$ (s^{-2})	$-3.86 \cdot 10^{-10}$	$-1.57 \cdot 10^{-11}$

Table 3.1: Crab and Vela pulsars physical characteristics [30]

3.3 Stochastic background

The *stochastic gravitational-wave background* is the incoherent superposition of the gravitational waves emission from various sources across the universe. The central limit theorem guarantees that the sum of a large number of incoherent signals, whatever their nature, is a random variable drawn from a Gaussian distribution, hence the name of stochastic background.

Such a background can be difficult to observe: by correlating the data of two interferometers, we might expect a correlation larger than the correlation foreseen with noise only[1]. Indeed, the stochastic background should be the same for both detectors and then a stronger correlation than uncorrelated detector noise should appear in the data after some period of time. By integrating the results for a large period of time, the separation between the noise and the stochastic background can be possible.

Among the sources of this stochastic background, we can cite: the multiple astrophysical sources sources across the universe [31], the primordial gravitational wave background, constituted by the waves emitted during the early ages of the universe, and even cosmic strings [32], one-dimensional objects that may have resulted from a phase transition in the early universe.

[1]The pipeline presented in this thesis is inspired from stochastic searches, and uses as well data correlation from two detectors.

3.4 Compact binary coalescence

Binaries of compact objects are among the most promising sources of waves. They continuously emit gravitational waves and lose energy, and by doing so, the members of such systems continuously get closer to each other. They eventually merge, creating a black hole and emitting a powerful and short burst of gravitational waves [33].

The gravitational wave signal of a binary system can be decomposed in three phases: the *inspiral*, the *merger* and the *ringdown*. The inspiral phase corresponds to the period of time when the members of the system orbits around each other, losing energy by the emission of gravitational waves and getting closer to one another [8].

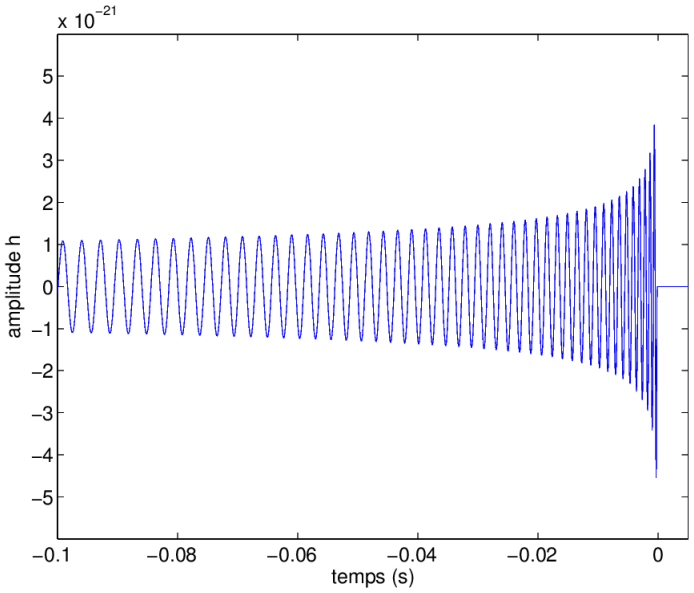

Figure 3.1: Analytic waveform of a (1.4 $M_\odot$,1.4 $M_\odot$) binary neutron star coalescence during inspiral phase [34]. x axis is time (in seconds), and y axis is the amplitude of the wave.

The gravitational waves emitted by the system at this point are well predicted by General Relativity, and their waveform can be analytically computed (see

figure 3.1 as an example of such waveform). The knowledge of the waveforms allows one to search for the signals very efficiently. The *match filtering* technique which is used in this case consists of calculating the correlation between the data and the computed waveform. This method guarantees an optimal detection efficiency, but can only be used when simulated waveforms are available [35, 36].

The inspiral signal is continuous, however its frequency enters the detection band of ground-based interferometers in its final stage (the time depending on the mass of the system). Depending on the mass and nature (neutron stars or black holes) of the binary members, the signal stays in the detection band for tens of seconds to tens of minutes.

During the merging of the system, gravitational waves waveforms are difficult to compute analytically. Efforts are on-going to compute them numerically, though the large parameter space these waveforms should cover would make match-filtering techniques computationally intensive. Unmodeled searches, like transient searches (see 3.5.1 and 3.5.2) are more suited to look for such signals.

Finally, if the system becomes a black-hole, it stabilizes by emitting a *ring-down* radiation – an exponentially damped sinusoidal signal – which can be modeled analytically.

Binary mergers of two neutron stars have an event rate of about $1\,\mathrm{Myr}^{-1}\mathrm{Mpc}^{-3}$, which corresponds to a detection rate of about $0.4 - 400$ events per year – most likely 40 – with the expected sensitivity of the future generation of ground-based interferometers [37]. These rates can be extrapolated from the number of known binary systems in our galaxy for which merging will happen in a time shorter than the age of the Universe. At the time of writing, six neutron stars binary systems are known in the Galaxy [33].

Neutron star + black hole and black hole + black hole systems are also possibles sources of short transients, even if they event rate is more speculative.

3.5 Transient sources

A source of gravitational waves shorter than the observation time are *transient* sources. They usually are violent, highly energetic and short lived events. The duration of the signals emitted by such sources can vary from sub-seconds to week-like durations. The analysis techniques used for these signals depend on the signal duration. We will first make a short review of short duration sources, and then we will focus more specifically on sources emitting signals of duration $> 1s$, the subject of this thesis.

3.5.1 Short duration transient sources

Gravitational collapse

Gravitational waves can also be emitted during *stellar collapses* resulting in a supernova [8, 38]. There are two main categories of supernovae. *Type Ia supernovæ* happen when a neutron star, member of a binary system with a regular star, accretes matter enough from its companion and increases its mass beyond the Chandrasekhar mass (1.44 $M_\odot$ for a neutron star). Then nuclear reactions can detonate the star. *Type Ib, Ic and II* supernovæ result from stars of mass greater than 8 $M_\odot$, when nuclear burning in their core cannot counterbalance gravitational force. The core of the star turns into a proto-neutron star. Then external layers of the star can collapse and rebounce on the core, which might in some circumstances produce an explosion[2].

Gravitational waves can be emitted during the creation of the proto-neutron star, whose rotation speed and eccentricity may be sufficient to emit gravitational waves. They can also occur during the initial collapse because of the magneto-hydro-dynamic instabilities (see figure 3.2 for an example of waveform simulation). Finally, when a supernova results in the creation of a black hole, ringdown radiation can be emitted [38].

[2]The initial bounce does not itself result in the supernova, its energy being transferred into a massive production of neutrinos. But the initial shock can be rejuvenated and can produce the explosion.

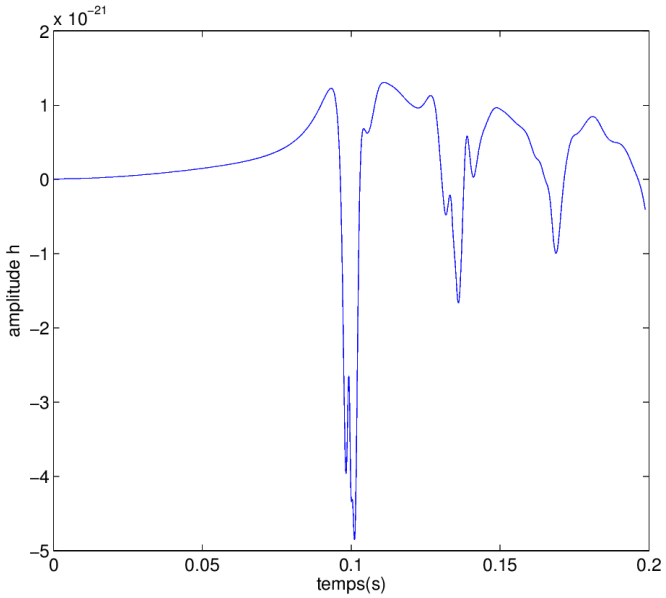

Figure 3.2: Simulated waveforms of gravitational wave emitted during a core collapse supernova [39, 40]. x axis is time (in seconds), and y axis is the amplitude of the wave.

The luminosity of supernovæ signals should restrain our detection capabilities. Therefore the expected detection rate is low, since the supernovæ rate in our galaxy if of the order of one in thirty years.

Other sources

Other violent phenomena could be gravitational waves emitters, like pulsar glitches, flares from soft gamma-ray repeaters, and even more exotic objects like cosmic strings cusps or kinks [8, 32]. It is also possible that events producing gravitational waves cannot be observed by means other than gravitational wave detection. They may be too faint, or may not even have an electromagnetic counterpart. Unknown objects might be discovered thanks to gravitational wave detection. It is therefore important to elaborate analyses capable to look for unanticipated signals. As we will now see, search techniques are different whether or not we are capable of observe a the sources *via* a different technique than gravitational wave detection.

Analysis techniques

To detect gravitational waves without prior knowledge of their structure, search pipelines specialized in the detection of short transient usually look for almost simultaneous[3] power excesses in a network of interferometers. If a gravitational wave reaches the Earth, it can be detected by all the interferometers taking data at that time. Indeed astrophysical sources are far enough from us so the spatial extent of the gravitational waves they emit is much larger than the Earth when the waves reach us. If a power excess is detected at the same time by several experiment, it can be a gravitational wave signal. The efficiency of such searches can be increased if the origin of the signal is known. In the case of a supernovæ its detection in the electromagnetic spectrum can provide the signal time and origin. This information is used to restrain the search to a short period of time. Also it gives the exact detection delays for each couple of interferometer used for the analysis, which is useful to separate the signal from the background. Such searches are called *triggered* searches, in contrast to the *all-sky* searches, which look for signals in the entire sets of data, anywhere in the sky.

3.5.2 Long duration transient sources

In this section we will detail long transient gravitational wave sources, especially sources which are expected to be detectable with the current or the next generation of ground-based detectors.

Protoneutron stars convection

Proto-neutron stars (PNSs) emitted by a stellar collapse, as described in 3.5.1, can also be a source of long transient gravitational waves. Because of fallback accretion [41], a PNS can become a powerful convective engine, driven by both lepton and temperature gradient, possibly during tens of seconds [42, 43, 44, 45].

[3]Depending on the origin of the signal, these detection won't be exactly simultaneous, because gravitational waves propagates at the speed of light. The time separation $\delta_{IJ}t$ between the detection of a signal by two experiments I and J is such that: $0 \leq \delta_{IJ}t \leq D_{IJ}/c$ where D_{IJ} is the distance between the two experiments.

Current models of gravitational wave emission from PNS convection cover only the first second after the core bounce [38, 46, 47], however features that translate to later times has been found. PNS convection is turbulent and therefore leads to an incoherent gravitational wave signal. In the slowly rotating case, it is randomly polarized. In the fast rotating case, rotationally-driven meridional currents may polarize the signal, though this effects still has to be studied with numerical simulations.

Current models suggest, in the first second after the core bounce, PNS gravitational wave signals of strain amplitudes at Earth level of about $h_{PNS} \sim 10^{-23}$ for sources at a distance of 10 kpc. The time-frequency structure of such waves is non trivial, with a broad spectral peak at ~ 300 Hz that shifts to higher frequencies during the first second after core bounce as the PNS becomes more compact [38, 46]. This behavior is expected to continue after this period. Based on the available simulations [43, 46], if we assume that the gravitational wave emission continues with a strength comparable to the early stages of the emission, then we expect a total emitted energy of the order of $E_{gw} \sim 4 \times 10^{-9}(\Delta t/30\text{s})M_{\odot}c^2$. A sufficiently long signal may well be detectable by ground-based interferometers if the source is located within our galaxy.

Rotational instabilities

PNS are most likely at their birth composed of an inner-core in solid rotation, and an outer region strongly differentially rotating [48]. PNSs in near-solid body rotation, when their rotational kinetic to potential energy ratio, $T/|W|$ reaches values between ~ 0.14 and ~ 0.27 can undergo a non-axisymmetric deformation caused by viscosity driven instability or secular gravitational-radiation [49, 50]. The timescale of both phenomena – which ultimately depend on PNS dynamics and viscosity – is estimated to be $\mathcal{O}(1\text{s})$. The secular instability could potentially last for $10 - 100$ s [49, 51].

The initially axisymmetric PNS slowly deforms into a bar shape and evolves toward null angular velocity $\Omega = 0$, its remaining rotational energy being stored as fluid's motion inside the bar [49, 52]. The gravitational wave amplitude h_{RI}

is proportional to Ω^2 and to the ellipticity ε characterizing the amplitude of the bar deformation. The wave strain will initially rise then slowly decay as Ω diminishes [49, 52]. The gravitational waves should be elliptically polarized, and their amplitude should be $h_{RI} \sim 6 \times 10^{-22} \left(\frac{30 \text{ Mpc}}{D}\right) \left(\frac{M}{1.4\ M_\odot}\right)^{3/4} \left(\frac{R}{10 \text{ km}}\right)^{1/4} \left(\frac{f}{100 \text{ Hz}}\right)^{1/2}$.

Neutron stars' r-modes

r-modes are quasi-toroidal oscillations that have the Coriolis force as their restoring force. They may be generated in accreting, newborn or rapidly spinning neutron stars [53, 54, 55]. They emit gravitational waves with frequency $f_{r\text{-}modes} = \frac{4}{3}\left(\frac{\Omega_{NS}}{2\pi}\right)$ and typical strain amplitudes of $h_{r-modes} \sim 4.4{\times}10^{-24}\alpha \left(\frac{\Omega_{NS}}{\sqrt{\pi G\bar{\rho}}}\right)^3 (\frac{20 \text{ Mpc}}{D})$, where Ω_{NS} is the neutron star angular velocity, D the distance to the source and $\bar{\rho}$ the mean neutron star density, and $\alpha \in [0, 1]$ the dimensionless saturation amplitude of the r-modes [55].

r-modes are expected to be a source of very long-lasting gravitational wave emission, but long transients may be possible in case of high saturation amplitude α [56]. However recent work suggests $\alpha \ll 0.1$ [54, 57], therefore r-modes are not our best candidates.

Accretion disk instabilities (ADIs)

During the collapse of a massive star, it is possible that its core, when its mass reaches $\sim 3M_\odot$ collapses directly into a black hole – this type of event is name a *collapsar*. Infalling matter will then form an accretion disk/torus of typically $\sim 1M_\odot$.

This torus is cooled by several mechanisms (neutrino emission...). Piro and Pfahl in [58] describe how nuclear cooling – through Helium photodisintegration – allows fragments to be formed inside the outer region of the disk. These fragments grow until forming little neutron stars of mass $\sim 0.1\ M_\odot$. When formed inside the same region, they can merge and reach a mass of $\sim 1\ M_\odot$. These fragments travel toward the central black hole because of viscous friction and emission of gravitational waves. The inspiral phase, and therefore the associated wave emission, is expected to last 10 to 100s. The typical gravitational waves amplitude

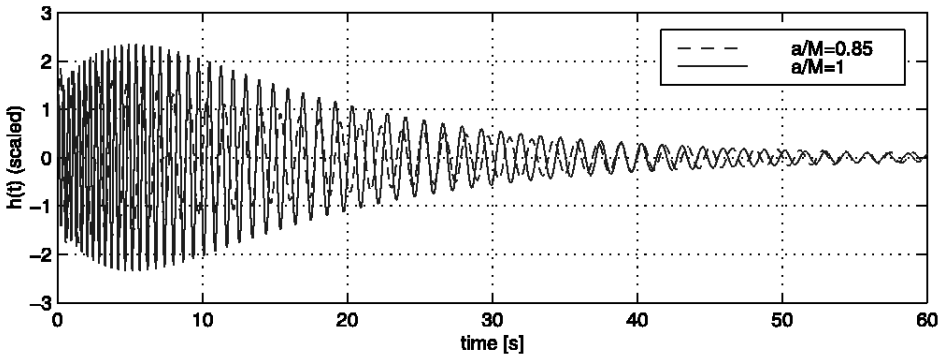

Figure 3.3: Simulated gravitational-wave waveform of an ADI signal [59], with two different set of parameters (a, M), a being the spin energy of the black hole and M its mass. Displayed frequency is a factor 1000 smaller than the waveform frequency, for illustrative purposes.

depends on whether viscous torques or gravitational wave emission dominates are the most important sources of energy loss. In a case where viscous forces dominate until rotation frequency reaches $f_{eq} = 100$ Hz, Piro and Pfahl show that the amplitude of the wave will grow as $f^{2/3}$ until f_{eq}, reaching a maximum of about $h_{Piro} \sim 10^{-22}$ at $f_{gw} \sim f_{eq}$, for a system with a central black hole of mass 8 $M_\odot$, a fragment of mass 1 $M_\odot$ and a source distance of 100 Mpc. These sources are then good candidates for detection of long duration signals by ground-based interferometers.

Another model of accretion disk instabilities was proposed by Van Putten in [59, 60, 61]. This model considers the case of a rotating black hole [59] surrounded by a strong magnetic field. This magnetic field couples with the torus' field, and tends to a state of minimal energy. The magnetic field can generate magneto-hydrodynamic instabilities inside the torus, which can lead to the emission of gravitational waves and gamma-ray bursts (GRBs).

This system should emit elliptically polarized gravitational waves, with a frequency between $(1 - 2$ kHz). They could last for seconds to minutes, duration comparable to the duration of the GRBs [59, 62]. With the energy foreseen in [59], a source at a distance of 100 Mpc could produce a strain of amplitude

$h_{vanPutten} \sim 10^{-23}$. Examples of waveforms are presented in figure 3.3. In the model described in [59], the signal has a characteristic chirp[4] signature: a signal with exponentially decreasing frequency, and decreasing amplitude (see figure 3.4).

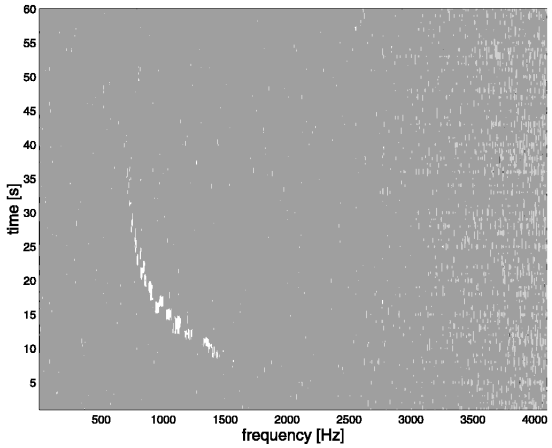

Figure 3.4: Simulated gravitational-wave waveform of an ADI signal [59], in the time-frequency domain.

Eccentric black holes binaries

We saw in section 3.4 that compact objects binaries are a source of short transients. The great majority of the models used in the framework of short transient searches use waveforms calculated based on the assumption that the eccentricity is zero [63, 64]. Indeed most of these systems are expected to have a circular orbit at the time of their merging [65], having lost their eccentricity *via* gravitational waves emission. However astrophysical motivations exist to consider eccentricity in binary systems. Regions surrounding supermassive black holes are expected to contain density cusps of stars and black holes. The density of compact objects in this environment makes possible close encounters of black holes with a fast

[4] A chirp is a signal which frequency increases or decreases with time. Compact binary systems in their inspiral phase are a classical example of chirp emittor.

release of energy, leading to their capture and to a rapid merging. In this case, mergers almost always possess non-null eccentricity [66].

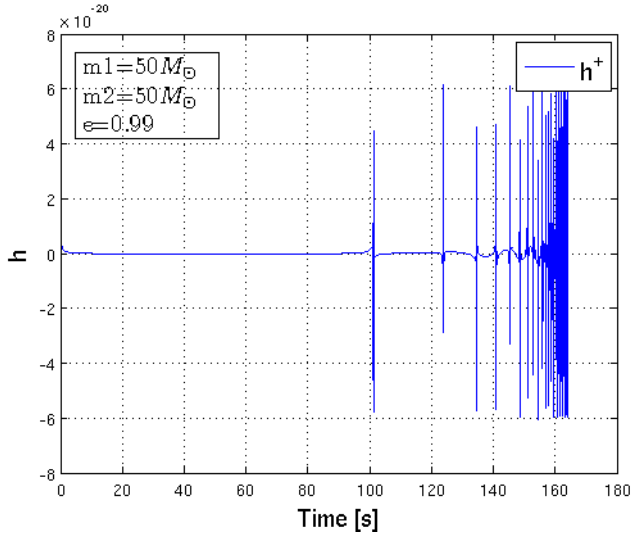

Figure 3.5: Simulated gravitational-wave waveform of an eccentric binary signal generated with the code presented in [67]. The black holes have a mass of 50 $M_\odot$ and the system possesses an initial eccentricity $e = 0.99$.

During the inspiral phase of such systems, gravitational wave bursts should be emitted each time the system reaches its periastron. This succession of short transient signals should last from several hours to several minutes depending on the binary parameters [66].

Recent studies estimate the rate of binary black holes close encounters to $\sim 0.01 - 1\ \mathrm{yr}^{-1}\mathrm{Gpc}^{-3}$, which corresponds to a detection rate of $1 - 100\ \mathrm{yr}^{-1}$ with advanced detectors [66, 68]. Figure 3.5 shows an example of waveforms expected with eccentric binary systems. Match filtering techniques can hardly be used to detect such signals. Indeed the structure of these waveforms is rather complex and the parameter space to investigate is important. Match filtering would be very computationally costly. Therefore, unmodeled searches, such as the one we will present in the next chapter, are more indicated to detect this category of signals.

Chapter 4

The STAMPAS pipeline

"Oh, Gravity, thou art a heartless bitch!"

Sheldon L. Cooper, PhD

As stated in the previous chapter, the search for long transient signals has a strong scientific motivation. However the existing transient analysis search pipelines (as a non exhaustive list of such pipelines, we can cite [69, 70, 71, 72, 73, 74, 75, 76]; the list of all the LIGO-Virgo search papers can be found in [77]) are not well suited for this task, and these signals never have been investigated with an all-sky pipeline, except in the very recent PhD thesis of Mark Edwards [78]. In this thesis we introduce a new search pipeline, STAMPAS, whose purpose is specifically to look for transient signals of duration $\mathcal{O}(1)$s to $\mathcal{O}(500)$s. It is an all-sky pipeline, which is able to find signals anytime, anywhere in the sky, without prior information on its location or time. In the first part on this chapter we will describe how we adapted a tool suited for targeted search to run an all-sky survey, then we will describe the pipeline itself, detailing its main technical features.

4.1 From targeted to all-sky search

4.1.1 STAMP

The STAMPAS pipeline is based on STAMP. STAMP, for Stochastic Transient Analysis Multi-detector Pipeline [79], is an analysis tool which calculates the correlation between data strains from two different interferometers[1] I_1 and I_2, : $s_{I_1}(t) \otimes s_{I_2}(t)$. This correlation is actually calculated in the frequency domain. STAMP first performs Fourier transforms of the $s_{I_1}(t)$ and $s_{I_2}(t)$ data strains. These transforms are performed on 1s long data chunks.

These Fourier transforms are multiplied together, and after some normalization, form an estimator of the power spectrum of the signal: $\tilde{h}(t,f)$. A phase shift is applied to the quantity: $\tilde{h}(t,f) = \tilde{h}(t,f)e^{2i\pi f\frac{\tau}{c}}$. According to the Wiener-Khinchin theorem [81], this is equivalent to study the correlation function $h(t) = s_{I_1}(t) \otimes s_{I_2}(t+t')$ with t' a time shift corresponding to the expected time difference between signal detection in the two different interferometers. Each t' value corresponds in practice to a *ring* of sky positions. As explained in section 2.4, a signal is, in general, not detected simultaneously by different detectors, but with a time delay which depends on its position in the sky. With a pair of interferometers, a given time delay corresponds to several positions in the sky, which form a ring on the celestial sphere.

After appropriate normalization of the results, taking into account the antenna factors associated with the investigated sky position (see 2.11), we obtain the pipeline statistics $Y(t,f)$ (see below). This quantity is calculated for each (t,f) pixel. The resolution used in the analysis is 1s $\times$ 1Hz. The Y variance, $\sigma_Y^2(t,f)$, is estimated for each pixel from its neighboring frequency pixels. The ratio $Y(t,f)/\sigma_Y(t,f)$ is the STAMP Signal-to-Noise Ratio (SNR), that we will use to characterize the signals. Note here that, contrarily to what is done in the short transient pipelines, the STAMP SNR compares the estimated "energy" of

[1]Note here that correlation between two data strains have already been used in searches for short gravitational wave transients [80].

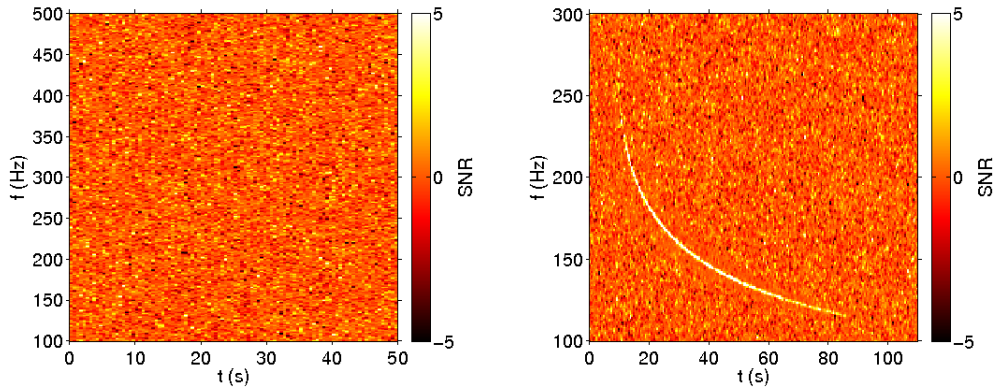

(a) Noise only (b) Simulated signal in the data

Figure 4.1: STAMP SNR maps with simulated data. The left map contains noise only, the right map also contains a simulated signal.

the signal $\left(\text{SNR} \sim \frac{\int h^2(t)dt}{P_s(t)}\right)$ to the estimated noise power, and not their respective estimated amplitudes $\left(\text{SNR} \sim \frac{h(t)}{A_s(t)}\right)$.

At the end of the process, a *frequency-time* map (later referred to as *ft*-map) is generated: it is a 2D array, which abscissa represents time, the ordinate the frequency, and each (t, f) pixel is assigned a $\text{SNR}(t, f)$. SNR can be positive in case of correlated data, and negative in case of anti-correlated data. In figure 4.1a is an example of *ft*-map generated by STAMP with Monte-Carlo (MC) data. In figure 4.1b a simulated signal has been added to the same data. The size of the *ft*-map in time and frequency is limited only by the memory required to run the clustering algorithm (see 4.1.2).

In the next section we will give a numerical overview of the STAMP pipeline.

Numerical overview

The quantities used by STAMP [79] are built to estimate the one-sided power spectrum of a gravitational wave signal, without any assumption on the signal shape or polarization. If we consider a gravitational wave signal $(h_+(t), h_\times(t))$,

then the one-sided power spectrum of this signal can be written as

$$H(t,f) = \sum_{A,A' \in \{+,\times\}} \left\langle 2\tilde{h}^*_A(t,f)\tilde{h}_{A'}(t,f) \right\rangle_{\delta t} \tag{4.1}$$

where $\sim$ denotes the Fourier transform[2], $*$ the complex conjugate, τ the start time of the δts analyzed, the brackets symbolizing the estimation of the quantity over δts. The factor of 2 comes from the fact that we use a one-sided power spectra.

STAMP is designed to search for long-duration signals. The power spectrum is estimated for period of T seconds, corresponding to the temporal resolution of the analysis. Furthermore, despite the fact we don't want to make assumptions on the signals, an assumption on the signal polarization is needed to be able to make an estimator of H. To stay as general as possible, we consider now that we are dealing with unpolarized signals. This allows us to consider in equation (4.1) only the $(+,+)$ and $(\times,\times)$ terms. The quantity we want to estimate is therefore

$$H(\tau,f) = 2 \sum_{A \in \{+,\times\}} \left\langle \tilde{h}^*_A(\tau,f)\tilde{h}_A(\tau,f) \right\rangle_{\delta t} \tag{4.2}$$

In the following calculations, all Fourier transforms are estimated over δts time segments, so we won't use the brackets to simplify the notation. Let us note here that the spectrum will have a frequency resolution of $\delta f = 1/\delta t$. In STAMPAS, we used a 1s $\times$ 1Hz resolution.

STAMP estimates $H(\tau,f)$ by calculating the cross-correlation of the data of two interferometers I and J, $s_I(t)$ and $s_J(t)$. The estimator of $H(\tau,f)$ is

$$Y(\tau,f,\vec{\Omega}) = \mathrm{Re}\left[C_{IJ}(\tau,f)Q_{IJ}(\tau,f,\vec{\Omega})\right] \tag{4.3}$$

with

$$C_{IJ}(\tau,f) = 2\tilde{s}^*(\tau,f)\tilde{s}_J(\tau,f) \tag{4.4}$$

[2]In practice we use a discrete Fourier transform, the data being sampled at a frequency $f_s = 4096$ Hz.

the cross-correlation of the two datasets and

$$Q_{IJ}(\tau, f, \vec{\Omega}) = \left(\frac{1}{2} \sum_{A \in \{+,\times\}} F_I^A(\tau, \vec{\Omega}) F_J^A(\tau, \vec{\Omega}) \right)^{-1} e^{2i\pi f \vec{\Omega} \cdot \Delta \vec{x}_{IJ}/c}. \tag{4.5}$$

The F_I^A are the antenna factors as defined in section 2.11, $\vec{\Omega}$ the unitary vector directed from the center of the Earth to the investigated sky position, and $\Delta\vec{x}_{IJ}$ the spatial separation between detectors I and J. The Q function is designed to maximize the value of Y when a signal is present and when $\vec{\Omega}$ corresponds to its true location in the sky, taking into account the detectors relative orientation (when a signal is weak in an interferometer because of the antenna factors, this weakness is compensated in some extent by filter function). Let us note here that since the estimator is constructed for unpolarized signals, to be as general as possible, this filter may not be optimal for polarized signals, which may induce imprecision in the spatial reconstruction in the case of polarized signals (see figure 4.4).

The Y quantity is calculated for each pixel (τ, f) of a given time-frequency map. In practice, we look a cluster of pixels, which constitute the triggers. To characterize the triggers, we build a Signal-to-Noise Ratio (SNR) from the Y quantity. First, we construct an SNR for each individual pixel. To do so we must estimate for each pixel the variance of the Y quantity. In [79] it is shown that an estimator of $Y(\tau, f)$ variance is

$$\sigma_Y^2(\tau, f, \vec{\Omega}) = \frac{1}{2} \left| Q_{IJ}(\tau, f, \vec{\Omega}) \right|^2 P_I^{adj}(\tau, f) P_J^{adj}(\tau, f) \tag{4.6}$$

where $P_I^{adj} = 2\overline{|\tilde{s}_I(\tau, f)|^2}$ is the one-sided power spectrum obtained with the auto-correlation of data from a given interferometer, averaged on the neighboring pixels at a given frequency. The more pixels are used, the better the variance estimation will get. However more calculations are needed. A compromise has to be done between the quality of the variance estimation, and computational exigences. In figure 4.2 shows plots illustrating the evolution of the SNR estimation with

respect to the chosen number of neighboring pixels, and the evolution of the pipeline efficiency depending on this number.

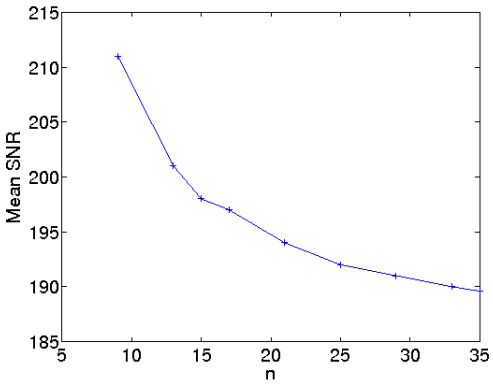

(a) Average SNR of 1000 injections of an accretion disk instability waveform, with respect to the number of pixels used to estimate the Y variance. n represent the total number of pixels used for this estimate, including the pixel where the variance is estimated.

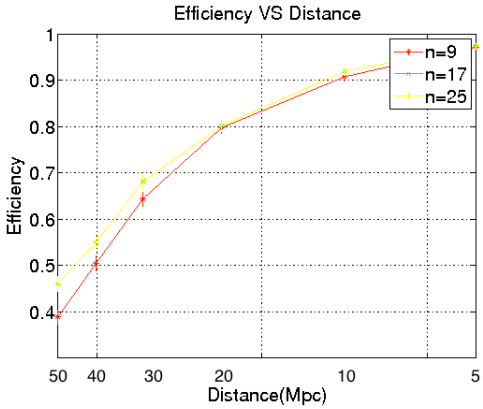

(b) Efficiency of the pipeline, for the same waveform, depending on the injection amplitude: strong injections are on the right of the plot. The plot is done for three values of the number of pixels used for the variance estimation. The efficiency is increased from $n = 9$ to $n = 17$, but does not change significantly with higher values of n.

Figure 4.2: Plots illustrating the choice of the number of pixels used for the Y statistic variance estimation. The search efficiency does not change significantly from $n = 17$. This value has been chosen for STAMPAS.

The estimate is done with 16 pixels following and preceding the considered pixel. The SNR for a single pixel is then given by

$$\mathrm{SNR}(\tau, f, \vec{\Omega}) \equiv \frac{Y(\tau, f, \vec{\Omega})}{\sigma(\tau, f, \vec{\Omega})} \tag{4.7}$$

For a cluster of pixels Γ, it is possible to calculate a global SNR, SNR_Γ. First, we want to build an estimator of the averaged gravitational wave power for a given cluster of N pixels,

$$H_\Gamma = \frac{1}{N} \sum_{(\tau,f)\in\Gamma} H(\tau, f) \tag{4.8}$$

An estimator of minimal variance of this quantity is a weighted sum of the Y quantity associated to the pixels of the cluster,

$$\mathcal{Y}_\Gamma(\vec{\Omega}) = \frac{\sum_{(\tau,f)\in\Gamma} Y(\tau, f, \vec{\Omega}) \sigma_Y(\tau, f, \vec{\Omega})^{-2}}{\sum_{(\tau,f,\vec{\Omega})\in\Gamma} \sigma_Y(\tau, f, \vec{\Omega})^{-2}} \tag{4.9}$$

The variance of $\mathcal{Y}_\Gamma$ being estimated as

$$\sigma^2_\Gamma(\vec{\Omega}) = \left(\sum_{(\tau,f)\in\Gamma} \sigma_Y(\tau, f, \vec{\Omega})^{-2} \right)^{-1} \tag{4.10}$$

The "energy" SNR_Γ is given by

$$\mathrm{SNR}_\Gamma(\vec{\Omega}) = \frac{\mathcal{Y}_\Gamma(\vec{\Omega})}{\sigma_\Gamma(\vec{\Omega})} \tag{4.11}$$

The "amplitude" SNR usually calculated in other pipelines is roughly the square root of SNR_Γ.

4.1.2 Clustering algorithm

Triggers are extracted from *ft*-maps using the "next-nearest neighbours" clustering algorithm *burstegard*[3] [82], which groups pixels of significant positive SNR together. This algorithm has five parameters:

- A pixel SNR threshold, SNR_t.
- A minimal number of pixels per cluster, n_p.
- A clustering radius R and two metrics parameters X_m and Y_m which parametrize the ellipses that will be used during the clustering.

[3] *burstegard* has been developed by Tanner Prestegard. His last name was used by Eric Thrane to forge the algorithm's name.

We will explain 4.1.2 the functioning of the algorithm using a simple example. Let us consider the *ft*-map in figure 4.3a. Parameters used on the figures are: $(\mathrm{SNR}_t, n_p, R, X_m, Y_m) = (4, 4, 2, 1, 1)$.

First, the algorithm considers only pixels with individual SNR superior to SNR_t, presented on the figure 4.3b. The algorithm loops over all the pre-selected *seeds* pixels not already members of a cluster.

1. The seed is pixel 0, and is the first pixel of the temporary cluster. An ellipse (E_0), of implicit equation: $X_m^2 x_0^2 + Y_m^2 y_0^2 \leq R^2$, where (x_0, y_0) are the coordinates of the pixel in the map, is considered around pixel 0. The algorithm loops over all the seed pixels from left to right and top to bottom, as long as they are not members of a cluster.

   (a) The algorithm tries to cluster pixel 0 with pixel 1. Pixel 1 is inside E_0, so it is clustered altogether with pixel 0 (see fig 4.3c).

   (b) The algorithm tries to cluster pixel 0 with pixel 2. Pixel 2 is inside E_0, so it is clustered altogether with pixel 0.

   (c) The algorithm tries to cluster pixel 0 with pixel 3. Pixel 3 is outside E_0, it is passed (see fig 4.3d).

   (d) The algorithm tries to cluster pixel 0 with pixel 4. Pixel 4 is outside E_0, it is passed. From this point no pixel in the loop can enter E_0, since pixel 4 has a vertical separation from pixel 0 of more than two pixels. The algorithm passes to the next seed pixel.

2. Pixel 1 is the seed. An ellipse (E_1) is considered around pixel 1. The algorithm will not try to cluster pixel 2, since it is already a member of the current cluster. It will try to cluster pixels 3 and 4, but will pass them.

3. Pixel 2 is the seed. An ellipse (E_2) is considered around pixel 2. Pixel 4 is added to the cluster (see figure 4.3e). Pixels 5 and 6 are passed.

4. There is no more seed in the cluster to be used. The temporary cluster is complete and possesses $n \geq n_p$ pixels, it is saved.

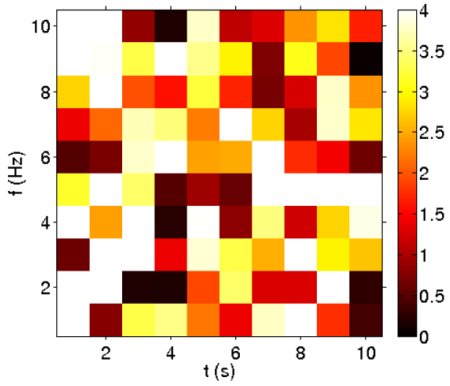

(a) Example of STAMP *ft*-map

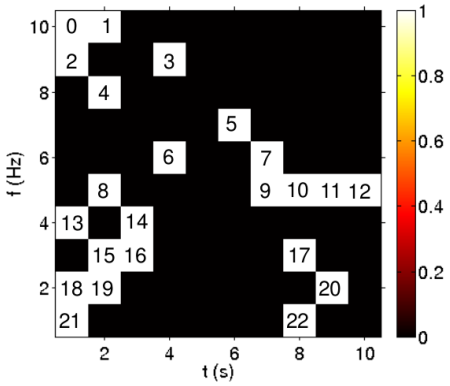

(b) Seed pixels

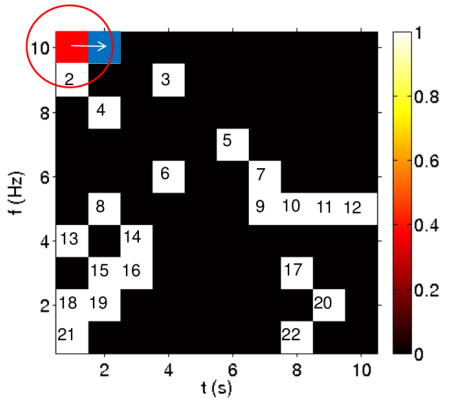

(c) Pixel 1 is clustered with Pixel 0

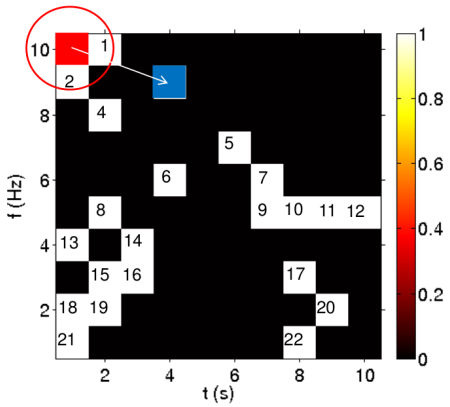

(d) Pixel 3 not clustered with pixel 1

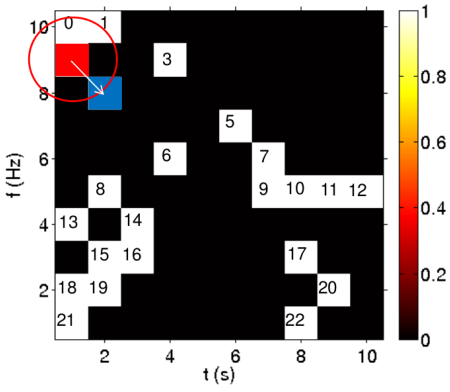

(e) Pixel 4 is clustered with pixel 2

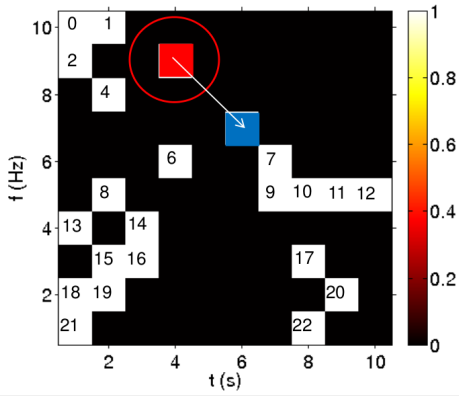

(f) Pixel 4 not clustered with pixel 3

Figure 4.3: Example of *burstegard* clustering.

5. The seed is pixel 3, and forms the new temporary cluster. Since pixels 0,1 and 2 are members of a cluster, the algorithm won't try to cluster them with pixel 3. An ellipse (E_3) is considered around pixel 3.

   (a) The algorithm tries to cluster pixel 0 with pixel 4 (see figure 4.3f). Pixel 4 is outside E_3, it is passed. From this point no pixel in the loop can enter E_3. There is no more seed pixel in the temporary cluster. It is complete and possesses $n = 1 \leq n_p$ pixels, it is not saved. But pixel 3 won't be used again for clustering since it is part of a cluster.

The algorithm continues until all seed pixels have been used. In the end, three clusters will be extracted from the map:

- Cluster 0, $\Gamma_0 = \{0, 1, 2, 4\}$
- Cluster 1, $\Gamma_1 = \{5, 7, 9, 10, 11, 12\}$
- Cluster 2, $\Gamma_2 = \{8, 13, 14, 15, 16, 18, 19, 21\}$

For each of these clusters, a global SNR – SNR_{Γ_i} – is calculated following equation (4.11).

4.1.3 Angular resolution

If we consider the STAMP Y quantity, which is the estimator of the signal power spectrum (see section 4.1.1), then we know from (4.3) that it can be written as

$$Y(\tau, f, \vec{\Omega}) = \mathrm{Re}\left[\frac{C_{IJ}(\tau, f)}{\varepsilon(\tau, f, \vec{\Omega})} \exp\left(\frac{2i\pi f \Delta\vec{x} \cdot \vec{\Omega}}{c}\right)\right] \tag{4.12}$$

with $\vec{\Omega}$ the unitary vector originating from the center of the Earth and pointing to the investigated sky direction, ε a function which depends on the antenna factors, $C_{IJ}(\tau, f)$ the result of the data cross-correlation of the considered pair of detectors, and $\Delta\vec{x}$ the spatial separation vector of the detector pair.

When there is a gravitational wave signal in the data, the simple cross-correlation $C_{IJ}(\tau, f)$ might not be maximal. Indeed, signals in both interferometers are separated by a small time-shift, which depends on the spatial localization

of the source. The exponential factor in the previous equation adds a phase shift which takes into account the phase factor corresponding to this spatial separation of the detectors.

Therefore to generate *ft*-map, one needs a precise sky location. To build an all-sky pipeline, it is necessary to explore all possible locations at a given time. The number of locations we will analyze directly depends on the maximal SNR loss we are ready to accept due to position mismatch. The relation between angular resolution and maximal SNR loss can be analytically computed.

We have: $\Delta\vec{x} \cdot \vec{\Omega} = |\Delta\vec{x}| \cos\alpha$ with α the angle between vectors $\vec{\Omega}$ and $\Delta\vec{x}$. Let us assume there is a signal present in the data at time t, and let us note α_0 the angle corresponding to the true direction of it source. If we generate a *ft*-map in a direction α, we have:

$$Y(\tau, f, \vec{\Omega}) = \mathrm{Re}\left[\frac{C_{IJ}(\tau, f)}{\varepsilon(\tau, f, \vec{\Omega})} \exp\left(\frac{2i\pi f|\Delta\vec{x}|\cos(\alpha)}{c}\right)\right] \tag{4.13a}$$

$$= \mathrm{Re}\left[\frac{|C_{IJ}(\tau, f)|}{\varepsilon(\tau, f, \vec{\Omega})} \exp\left(\frac{2i\pi f|\Delta\vec{x}|\cos(\alpha)}{c} + \theta_0\right)\right] \tag{4.13b}$$

$$\propto \cos\left(\frac{2\pi f|\Delta\vec{x}|\cos(\alpha)}{c} + \theta_0\right) \tag{4.13c}$$

where θ_0 is the phase that maximizes $Y(\tau, f)$ (we neglect the impact of the efficiency term $\varepsilon(\tau, f, \vec{\Omega})$):

$$\cos\left(\frac{2\pi f|\Delta\vec{x}|\cos(\alpha)}{c} + \theta_0\right) = 1 \tag{4.14}$$

Now consider if we generate a *ft*-map in a direction $\alpha = \alpha_0 + \delta\alpha$, $\delta\alpha$ being a small direction mismatch. We want to calculate the maximal angular mismatch $\delta\alpha_X$ one can tolerate if the maximal admissible loss in SNR is $X\%$ of the SNR recovered in the optimal case $\alpha = \alpha_0$. In the case where $\alpha = \alpha_0 + \delta\alpha_X$, one will

Interferometer pairs	H1L1	L1V1	V1H1
Angular resolution	0.7°	0.3°	0.3°
Raw number of positions to investigate	∼84000	∼458000	∼458000
Number of rings to investigate	161	425	437

Table 4.1: Angular resolution of a STAMP search for all three pairs of detectors with upper frequency limit of 1000 Hz.

have:

$$\cos\left(\frac{2\pi f|\Delta\vec{x}|\cos(\alpha_X)}{c}+\theta_0\right)=\frac{X}{100} \tag{4.15a}$$

$$\frac{2\pi f|\Delta\vec{x}|\cos(\alpha_X)}{c}+\theta_0=2k\pi\pm\cos^{-1}\left(\frac{X}{100}\right) \tag{4.15b}$$

where $k\in\mathbb{Z}$. One can then write

$$\frac{2\pi f|\Delta\vec{x}|}{c}(\cos\alpha-\cos(\alpha_X))=\pm\cos^{-1}\left(\frac{X}{100}\right) \tag{4.16}$$

In STAMPAS, $X=70\%$ has been chosen as a good compromise between resolution and search efficiency. Straightforward calculations lead to

$$\delta\alpha_{70}\leq\frac{c}{8f|\Delta\vec{x}|} \tag{4.17}$$

Angular resolution depends on the interferometer pair used and on the maximal frequency range of the *ft*-map we create. The table 4.1 summarizes the angular resolution with 70% SNR loss for all three pairs of LIGO-Virgo detectors, using a maximal frequency of 1000 Hz. These angular resolutions have been experimentally checked by injecting a strong signal in Monte-Carlo data, and then running a simple STAMP search on several sky positions centered on the true location of the injection. Figure 4.4 shows for the investigated sky patch, the maximal SNR recovered at each direction: the width of the ring inside which SNR values are above 70% of the optimal value corresponds to the analytically predicted value in the table.

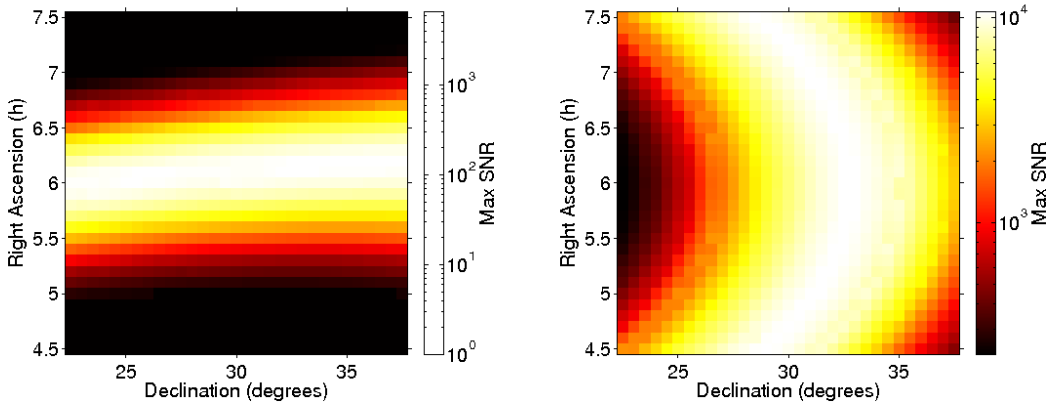

(a) At $(6\text{h}, 30\,^\circ)$, the recovered SNR is maximal.

(b) At $(6\text{h}, 30\,^\circ)$, the recovered SNR is not maximal.

Figure 4.4: The same polarized signal has been injected at the same spatial location, but at two distinct times. Sky patches of the sky centered on sky coordinates $(6\text{h}, 30\,^\circ)$ have been realized for each injection: ft-maps have been realized for several positions around the injection true location. The x and y axis represent respectively declination and right ascension, pixels color indicates the SNR of the recovered injection: a white/yellow pixel corresponds to a strong SNR, a red/black pixel to a weak SNR . Such maps have been used to check the loss in SNR due to position mismatch, and to study the position mismatch of polarized signals. Depending on the relative position of the two interferometers, a polarized injection may not be maximally recovered when investigating its true location, as it can be seen of the right map.

Given these numbers, it is possible to estimate, for these angular resolutions, the theoretical total number of sky positions we want to investigate: $N_{pos} \simeq 4\pi/a^2$ where a^2 is the angular resolution squared, in steradians. Results are given in table 4.1. Such number of ft-maps to analyze would take too much computation time, and the search wouldn't be viable.

However, it is possible to greatly reduce this number. Indeed, the STAMP algorithm is based on cross-correlating results of a pair of interferometer. As we stated in 2.4, several detectors are needed to localize a signal in the sky. With two of them, this localization is not unique. Indeed, a given time-delay between

two detectors is equivalent to a ring of directions in the sky. Therefore, scanning all different sky positions is useless in STAMP, since the result will be highly degenerate. Only one position per ring is needed. This reduces by a factor $\sim 10^3$ the number of positions to investigate effectively in the framework of STAMPAS analysis. Results for each pair are given in table 4.1.

4.1.4 Zebragard

In the previous section we calculated the number of positions needed to run a full all-sky search, using the STAMP algorithm, for a given time segment. It is possible to reduce this number even more. In the case where a signal is present at a given time, it can appear in a time-frequency map even when the statistic's optimal filter is calculated using the wrong sky direction : instead of being fully correlated, the signals present in each interferometer will alternately be correlated and anti-correlated due to the incorrect optimal filter.

This effect can be seen on the STAMP *ft*-map: when looking at a wrong direction, the signal appears to alternate with positive and negative SNR (see figure 4.5).

Zebragard is a clustering procedure based on *burstegard* (see 4.1.2). The principle is the following: first clustering is done using *burstegard* with a specific set of values of the SNR_t and n_p parameters, to be sensitive to smaller clusters. The same operation is done on the pixels which SNR is negative – which corresponds to anti-correlated data – usually rejected due to the SNR threshold, positive. These operations constitute the first stage of the clustering.

Clusters of the same category (with positive SNR or negative SNR) are then clustered together once more. Indeed a relevant cluster can be split into several parts due to a notched frequency line for instance. It is possible that the first stage of the clustering wouldn't recover entirely this kind of cluster. To this end, the clustering radius R is increased in this second stage – along with n_p to reduce the number of noise clusters.

The final stage of the clustering consists in clustering clusters of positive SNR with negative SNR clusters with adapted SNR threshold SNR_t and minimal

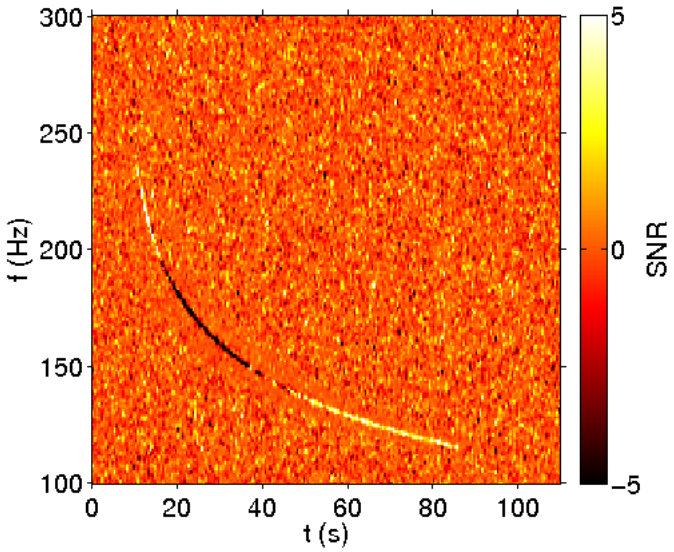

Figure 4.5: Signal recovered at a sky direction different from its true position. The "zebras" correspond to correlated and anti-correlated signal, which are clearly visible.

number of pixels n_p. We note that to reduce noise triggers, positive SNR clusters must be clustered to negative SNR only, and *vice versa*. Indeed a signal will always be alternatively constituted of positive and negative SNR clusters, due to the alternance between correlated and anti-correlated signals[4]. The numerical values of *burstegard* parameters for all clustering levels, are given in table 4.2.

It is therefore theoretically possible to detect a gravitational wave signal, wherever it might originate from, studying only one sky direction. The efficiency of the algorithm is however reduced by two factors. First, at the transition between positive and negative SNR regions of the same signal, SNR is about 0. These pixels are lost for the clustering, which decreases the recovered SNR. Then, the stripes constituting the signal might be too little to be recovered by the initial stage of *zebragard*.

To make a compromise between increasing the speed of the search, and limiting the loss in efficiency, STAMPAS analyzes, using *zebragard*, a limited number of different sky positions, randomly chosen. The figure 4.6 illustrates the anal-

[4]This striped appearance gave its name to the algorithm.

Burstegard parameters	*Zebragard* first stage	*Zebragard* second stage	*Zebragard* final stage
SNR_t	1	1	1
n_p	20	30	80
R	2	4	25
(X_m, Y_m)	(1,1)	(1,1)	(1,1)

Table 4.2: Values of the *burstegard* parameters used at the different stages of *zebragard*. SNR_t is the individual pixel threshold, n_p the minimal number of pixels inside a cluster, R the clustering radius and (X_m, Y_m) are metrics parameters.

ysis time evolution with respect to the number of positions used by STAMPAS. It is overall linear with the number of positions. The evolution of the search efficiency however, is not linear at all. Using 5 positions instead of one increases the efficiency by 80%, but using 10 positions instead of 5 increases the efficiency by only 10%.

Finally using 5 sky positions is the best compromise: we gain a factor 100 in processing speed, for a $\sim 10\%$ loss in efficiency.

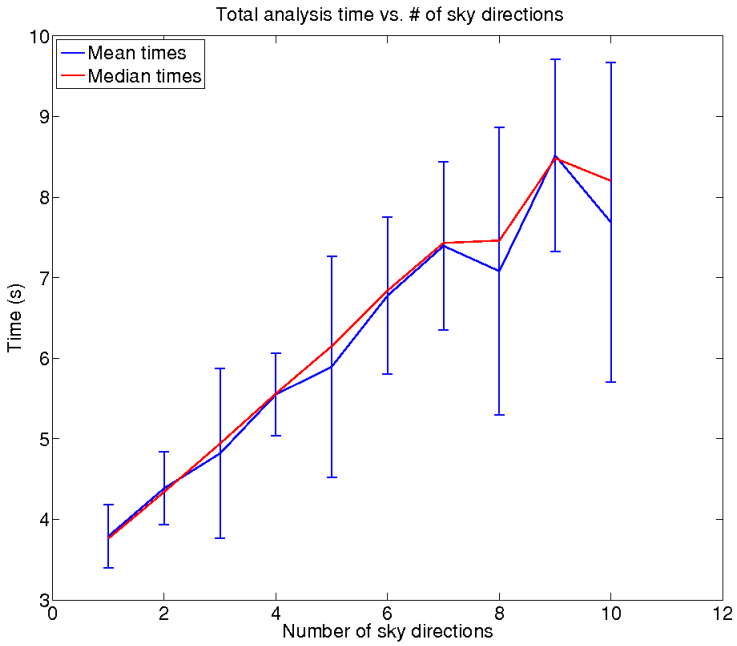

Figure 4.6: The time needed to run *zebragard* on one *ft*-map depending on the number of positions analyzed, varies linearly, which is not surprising. 100 trials per different number of sky directions used have been made.

4.2 The STAMPAS pipeline

4.2.1 Pipeline structure

The STAMPAS pipeline has a simple structure. Once the dataset is chosen, the analysis is done in three steps:

1. Pre-processing: On each data stream, Fourier transforms of 1s segments are done and saved. Each segment will be used more than once, for background estimation (see section 5.2.1 for more details).

2. Processing: The dataset is divided in 500s long time windows. For each of these time windows, 5 sky positions, randomly chosen, are investigated using the STAMP and the *zebragard* clustering algorithm. The duration of the time windows can be adapted if a trigger is detected at the very end of a map: it's the variable windows algorithm, described in 4.2.2. Some time segments can be removed by STAMP internal glitch cut, described in 4.2.4. Clusters found in each of these maps are saved.

3. Post-processing: The triggers obtained will undergo a selection based on different criteria, defined after a complete study of the background. Only triggers passing all these selections will be considered as gravitational wave candidates.

In section 4.2 we will describe the processing step of the pipeline. The post-processing will be detailed in the next chapter.

4.2.2 Analysis windows

STAMPAS goal is to detect, whatever their source, long duration transient signals. The frequency range investigated is [40, 1000 Hz], as broad as possible, knowing that the interometers' spectral density is very high under 40 Hz, and according to the existing theoretical models, we do not expect long duration transients to be found at frequencies higher than 1000 Hz. The maximal duration of the signals it is able to optimally recover depends directly on the size of the

ft-maps used. The amount of time covered by a single map is limited by the time required to run the clustering algorithm.

Furthermore, data division in several *ft*-maps is arbitrary, and a signal may well be found in-between two different maps. In this case the signal won't be optimally recovered. Worse, it can be totally lost, its components in the first and the second being too small to be clustered.

A solution to this issue is to apply a constant overlap between each *ft*-map considered – usually corresponding to 50% of the duration of the maps. To analyze the time segment [0s, 1000s] using 500s long maps, one can split the segments in [0s, 500s], [250s, 750s] and [750s, 1000s] instead of simply analyzing [0s, 500s] and [500s, 1000s]. Using this strategy with a 50% overlap, one is certain to completely recover any signal of duration up to $T/2$, T being the duration of the map. However, this technique doubles the computation time needed to run the search. Depending on the trigger rate of the search, it can also be quite inefficient.

In the dataset we analyzed (see next chapter for more details), the average trigger rate, without any selection applied on the triggers, is about $3 \cdot 10^{-3}$ Hz, which corresponds to about 1 trigger per map of 500s. The rate of triggers happening at the border of two maps R_{cut} is approximately

$$R_{cut} = T_{trigger} \times R_{trigger} \times \frac{1}{T_{map}} \tag{4.18}$$

$T_{trigger}$ being the average duration of a trigger, $R_{trigger}$ the trigger rate and T_{map} the duration of the maps. For 10s triggers, with the above trigger rate, $R_{cut} \sim 5 \cdot 10^{-5}$ s, or $R_{cut} \sim 0.03$ per map. This situation would be rather uncommon, and therefore the efficiency of the constant overlap quite low.

4.2.3 Variable windows

The solution STAMPAS is using is to use windows with variable duration – technique later referred to as *variable windows*. This algorithm works as follow:

- A first window $[0, T]$ is analyzed. Its duration is T seconds, the "standard" duration.
- If no trigger is found ending in the last 10 seconds of the map, the following map will be $[T-10, 2T-10]$. Its duration is T seconds and it has an overlap of 10 seconds with the current *ft*-map.
- If a trigger is ending in the last 10 seconds of the map:
  - If, among the triggers ending in the last 10s of the map, the earliest beginning trigger begins after $T - 10$, nothing is done[5].
  - If, among these triggers, the earliest trigger begins before $T - 10$, at a time noted t_{new}, the beginning of the following map will be changed from $T - 10$ to t_{new}. Note that it is possible for the time t_{new} to correspond to the beginning of the analyzed map.
- If there are triggers which begin before t_{new} and end after t_{new} *i.e.* triggers which would be in-between the current map and the following map, t_{new} is changed to be the start time of the earliest happening trigger. This step is applied recursively until no trigger is found in-between the two maps.
- If the duration reached by the following map goes beyond T_{limit}, its duration will remain T, otherwise its duration is adjusted. Any trigger found starting after t_{new} are dismissed at this point, and will be considered only as part of the following map.
- The following map is analyzed, and the duration of the map following it is adjusted following the same procedure.

[5]The 10s minimal overlap is here to catch signals which, because they happened in-between two maps, couldn't generate a cluster in the first map.

Put in different words, the size of the analysis windows grows dynamically depending on the triggers found inside the map. Of course, a limit is put to this extension. With this algorithm, it is theoretically possible to optimally recover any signal of duration $t_{signal} < T_{limit}$, since such a signal can be contained in a single map. The limit T_{limit} is due to the clustering algorithm which cannot manage too large maps for memory reasons. In this study, we have chosen $T_{limit} =$ 600s. This algorithm reduces the computation time needed to run the study, and insures that no signal will be lost because of the arbitrary analysis windows. The map duration being increased only when needed, its usage is optimal. According to the results of the analysis described in chapter 5, the variable windows affected 1.94% of the total number of analysis windows, the time added to the maps being in average of 12s (on 500s long maps), and at maximum 65s. Figure 4.7 summarizes the behavior of the variable windows.

4.2.4 The glitch cut

As it has been discussed in 2.9, a STAMPAS analysis can be spoiled by the presence of glitches (short power excesses due to an environmental disturbance or a technical malfunction) in the data. Loud excesses of power in a single interferometer can induce a non-null cross-correlation between the data, even though there is only little power in the other interferometer. If the power in these glitches is high, and if they last for $\sim$ 1s *i.e.* the pixel time resolution, they can be misinterpreted as a signal.

To suppress the glitches, the STAMP algorithm possesses an internal process which identifies and suppress the time period in the maps contaminated by such glitches. This identification code is called the *glitch cut*, its functioning is detailed in [83].

It is possible to estimate the power in a given detector, over δt seconds, by self-correlating its data. For a given time-frequency pixel (τ, f), one has

$$P_I(\tau, f) = 2 \left\langle \tilde{s}_I^*(\tau, f) \tilde{s}_I(\tau, f) \right\rangle_{\delta t} \tag{4.19}$$

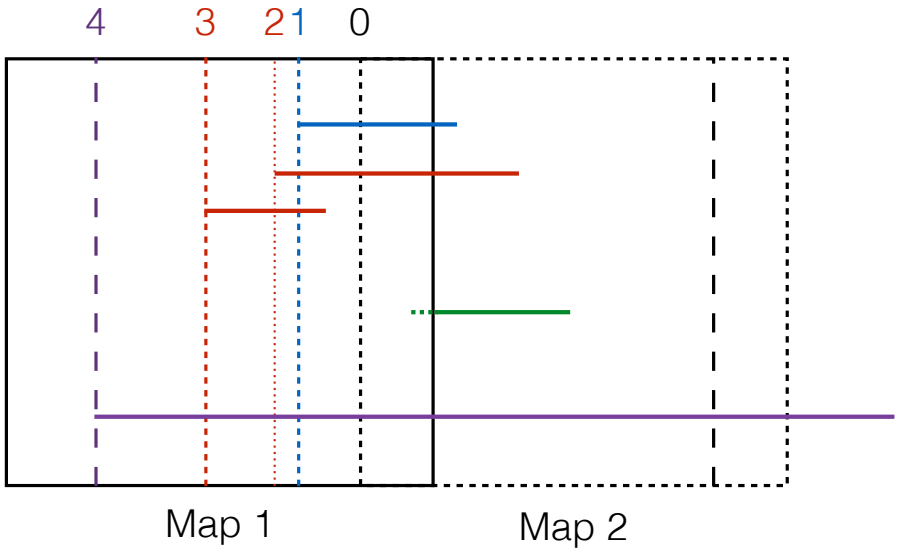

Figure 4.7: This scheme represents two consecutive *ft*-maps, called map 1 and map 2, with different situation. When no trigger is inside map 1, the dashed black line (position 0) is the beginning of map 2. It overlaps map 1 by 10s. In the case where the trigger in green is present, this start time won't change. It is possible that this trigger isn't seen in map 1, because it is too small. This is why we introduce a minimal 10s overlap, which allows map 2 to recover the green trigger entirely. If the blue trigger is present in map 1, then the start time of map 2 is moved to the dashed blue line (position 1). If the triggers in red are present, the start time of map 2 is moved to the dotted red line (position 2). Since a trigger is present at this level, the start time is further shifted to the dotted red line (position 3). Finally if the purple trigger is present, map 2 start time is moved to the purple dashed line (position 4), and map 3 start time (black dotted dashed line) will also be moved to position 4.

If we assume the noise to be stationary around the considered pixel, it is possible to estimate the fraction of this power due to a genuine gravitational wave signal. Consider the average power in the neighboring pixels in frequency,

$$P'_I(\tau, f) = \frac{1}{2n} \sum_{t=\tau-\delta t}^{t=\tau+n\delta t} P_I(t, f) - \frac{1}{2n} P_I(\tau, f) \tag{4.20}$$

with n the number of pixels used before and after the central pixel, τ the central time and δt the time resolution (in STAMPAS, it is 1s). If the noise is stationary, and if we consider that no gravitational wave power (or few) is present at time τ, then $P'_I(\tau, f)$ is an estimation of the noise present at time τ. Gravitational wave power present at time τ can be estimated as

$$P_I^{gw}(\tau, f) = \frac{P_I(\tau, f) - P'_I(\tau, f)}{\varepsilon_{II}} \tag{4.21}$$

with ε_{II} the interferometer orientation factor.

If a gravitational wave signal is responsible for an increase in power, it should appear in both detectors, at an amplitude modulated by the antenna factors. The difference of power should be close to ~ 0. If a power raise is due to a glitch happening in only one interferometer, this difference will be significantly different from 0.

We therefore construct the following quantity:

$$\Xi(\tau, f) = P_I^{gw}(\tau, f) - P_J^{gw}(\tau, f) \tag{4.22}$$

It is possible to build from this statistic a SNR – the SNR_Ξ – calculated for each pixel of the *ft*-map [83]. At a given time, an excess of pixels with $0.93 < |\mathrm{SNR}_\Xi| < 1.07$ is typical of a glitch[6], and a group of $\mathrm{SNR}_\Xi \sim 0$ pixels is typical of power present in data streams of the two interferometers. In addition to this criteria, another quantity estimating the stationarity of the power in each interferometer

[6]Depending if $\mathrm{SNR}_\Xi(\tau, f) < 0$ or > 0, it is possible to deduce in which interferometer the excess appeared

is calculated,

$$R_I(\tau) = \frac{1}{N_f} \sum_f \frac{P_I(\tau, f)}{P'_I(\tau, f)} \tag{4.23}$$

with N_f the number of pixels by column in the *ft*-map. Indeed, pixels surrounding a glitch, due to the variance estimation, may also have SNR_Ξ close to ± 1. In the case where a power excess happens at time τ in interferometer I, $R_I(\tau) > 1$. If the excess appears at $\tau \pm \delta t$, then $R_I(\tau) < 1$. This quantity, calculated for both interferometers, is used to avoid the vetoing of times surrounding a glitch.

A pixel (τ, f) is considered spoiled by a glitch if and only if:

$$\begin{cases} 0.93 < \mathrm{SNR}_\Xi(\tau, f) < 1.07, \text{ if a glitch occurs in } I \\ -0.93 > \mathrm{SNR}_\Xi(\tau, f) > -1.07, \text{ if a glitch occurs in } J \end{cases}$$

A time τ will be vetoed if more than $X\%$ of triggers are considered "glitchy", and if:

$$\begin{cases} R_I(\tau) > R_g \text{ and } R_J(\tau) \leq R_g \text{ if a glitch occurs in } I \\ R_J(\tau) > R_g \text{ and } R_I\tau) \leq R_g \text{ if a glitch occurs in } J \end{cases}$$

R_g and X can be tuned to obtain a better efficiency and avoid to remove signal. In STAMPAS, we found that setting $R_g = 2$ and $X = 2.7\%$ yields a good glitch rejection rate: the majority if glitches present in 1 in real data (not containing physical signal) were successfully removed by the glitch cut [83]. The glitch cut is also safe with respect to physical signals.

The version of the glitch cut used in STAMPAS has been updated since [83]. The above criteria take into account the entire frequency band at a given time. But it may happen that a glitch happening in a narrow frequency band passes these thresholds. In STAMPAS the glitch cut criteria are estimated over three different frequency ranges, rather than the whole frequency range of the map, to better remove glitches happening in a short frequency range – especially low frequencies between 40 and 150 Hz. The percentage of pixels above the SNR_Ξ threshold and the R_I values are estimated on several smaller frequency bands, which pave the entire frequency range at a given time and overlaps each other by

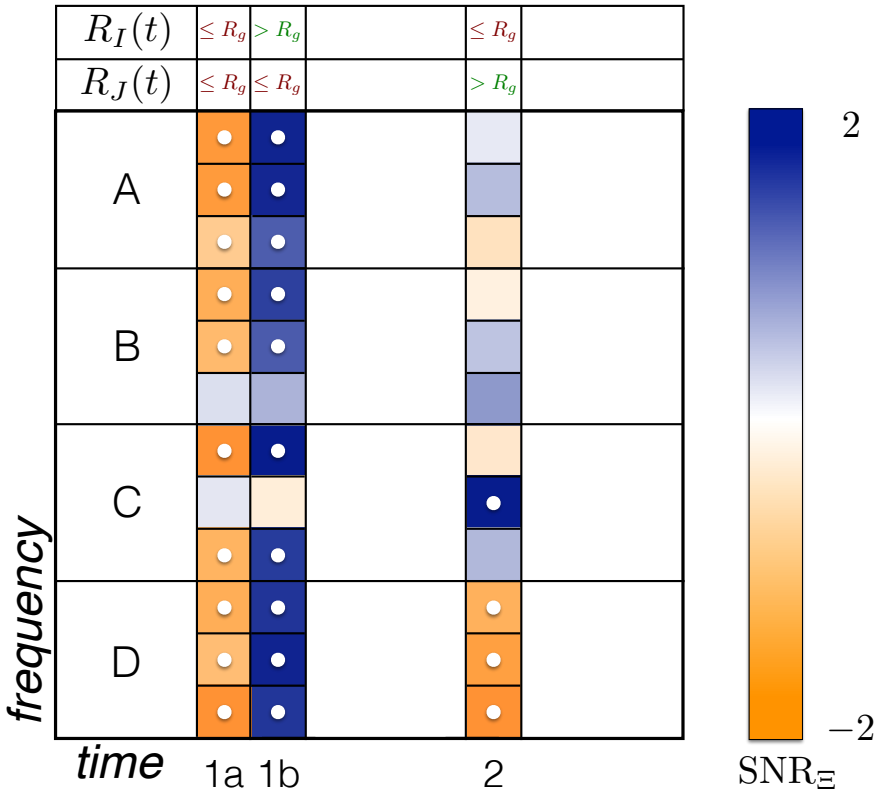

Figure 4.8: This scheme represents a *ft*-map, with three different times: 1a,1b and 2, and four different frequency bands: A,B,C and D. The color scale represents SNR_Ξ for each pixel. A pixel is marked with a white dot if its SNR_Ξ has a value compatible with the value induced by a glitch ($|\mathrm{SNR}_\Xi| \sim 1$). For this example, the fraction of "glitch-like" pixels required to veto a given time is 30%. Column 1a has enough glitchy pixels to be vetoed, but if we consider the $R_{I,J}(t)$ values at that time, we see that they are consistent with regular noise. 1a is not vetoed. Column 1b has enough glitchy pixels to be considered, and the $R_{I,J}(t)$ are consistent with a glitch present in 1b, occurring in interferometer I. The sign of the glitchy pixels' SNR_Ξ is consistent with this information. The 1b column will be vetoed. The column 2, taken as a whole, does not have enough glitchy pixels to trigger the glitch cut, even though the $R_{I,J}(t)$ are consistent with a glitch in interferometer J. Indeed, one pixel among the four marked with a white dot has an SNR_Ξ which sign is inconsistent with the $R_{I,J}(t)$ values, it is not taken into account. But if we calculate the fraction of glitchy SNR_Ξ in each of the 4 frequency bands, we can see that in the band A, the fraction of glitchy triggers is above the 30% threshold. Column 2 will be vetoed. Note that the frequency bands actually overlaps each other by half, which is not the case on this scheme for simplicity reasons.

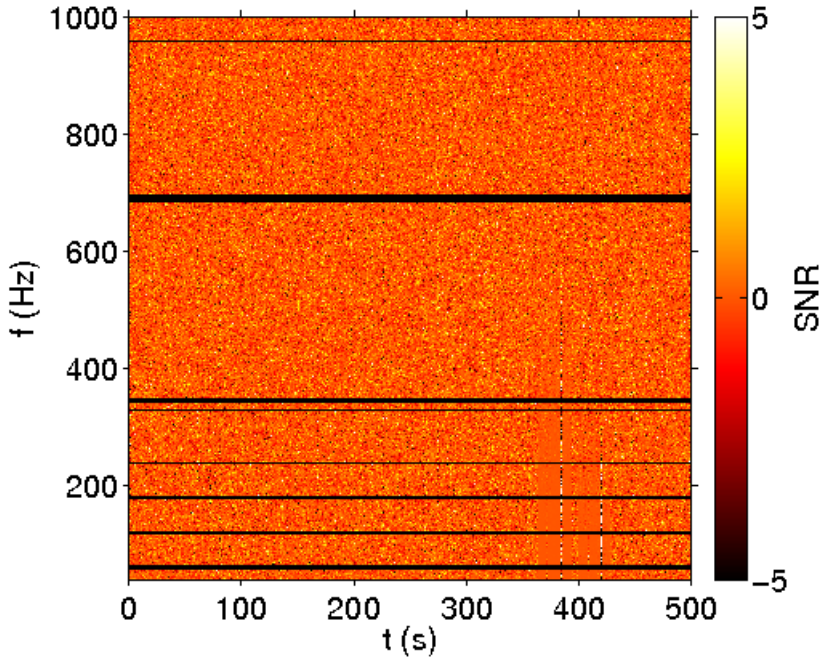

(a) Glitches present in the data

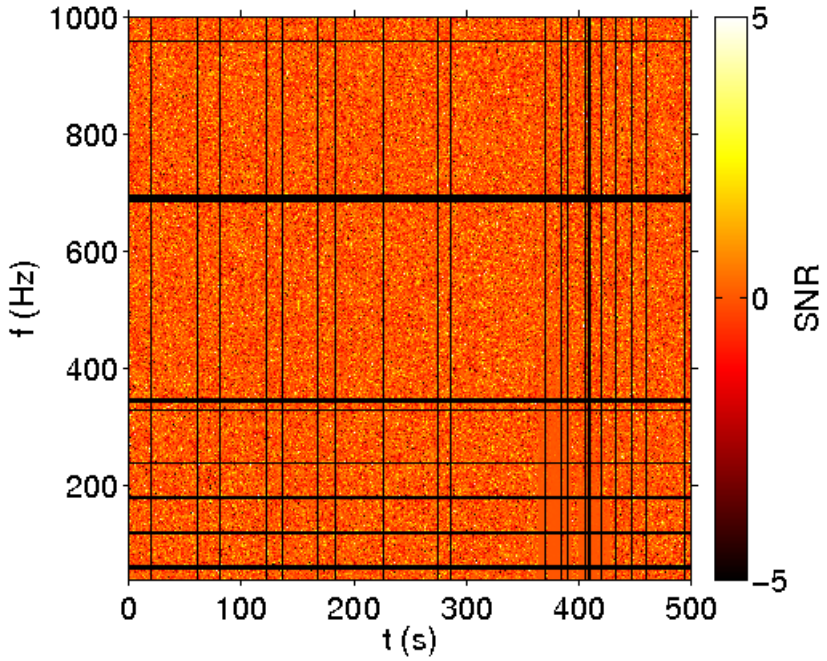

(b) All the glitches are vetoed

Figure 4.9: STAMP SNR maps of 500s duration with real data. The glitch cut is not activated on the left map, and it is on the right map.

50%. In STAMPAS, the glitch cut is calculated on the following bands: [40 Hz, 482 Hz], [242 Hz, 723 Hz] and [482 Hz, 1000 Hz]. See figure 4.8 for an example.

In figure 4.9a, is presented a *ft*-map containing such a glitch, and in 4.9b the *ft*-map obtained when the glitch cut is applied.

4.2.5 Injections

To estimate the efficiency of the pipeline, in the absence of known gravitational wave signals in the data, it is necessary to perform what we call *injections*. An injection consists in adding to the dark fringe signals of both interferometers a simulated gravitational wave signal. This operation is repeated at random times. Then, the STAMPAS pipeline runs on these modified data. The efficiency is characterized by the fraction of injections that have been detected. In this section we will detail the way injections are done in STAMPAS.

Amplitude of the waveforms

For a given waveform (*i.e.* a given analytical simulation of gravitational wave signal), the detection varies with its amplitude. A strong signal will be detected almost certainly, a weak signal will be missed most of the times. It is important to know at which amplitude a given waveform can be detected on average. In this perspective, for a given waveform, injections in STAMPAS are be done using different amplitudes, and the efficiency – the fraction of recovered injection signals – is estimated for each of these amplitudes.

Marginalization procedures

Also, each different injection is done at a random sky position, to take into account the impact of the antenna factors on the efficiency. The waveform polarization is also randomly chosen for each trial.

The injection routine

Injections are done on a time slide – *i.e.* on data which has been time shifted before being correlated – to make sure that no genuine physical event is present in the study. To save computation, each injection is done randomly in a time window 3 times longer than a default analysis window – later referred as to the injection window. On this time segment, the STAMPAS search is run normally: the injection window will, by construction, be divided in three different *ft*-maps. The point of dividing the injection window in several maps is that the signal can fall in-between two maps, like a genuine signal could in the actual dataset. Injection studies and background are therefore done the same way (especially they both use the variable windows algorithm described in 4.2.3).

Over the total trigger list generated, the triggers which time and frequency are consistent with the time and frequencies of the injection are considered, to make sure that no noise trigger happening in the same time-frequency window is falsely identified as an injection.

The injection windows are then analyzed without any injection, and any trigger present in the window with and without injection is excluded, since only a noise trigger can be present in both maps.

Finally, any trigger selection procedure used for the data analysis is applied to the list of remaining triggers. For a given injection window, an injection is considered recovered if a trigger passed all the previous selections.

At this stage, it is possible to plot *efficiency curves*, which for a given set of selection procedures, plots the ratio of recovered injections over the total number of injections for each waveform amplitude used. An example of such curve is given in figure 4.10.

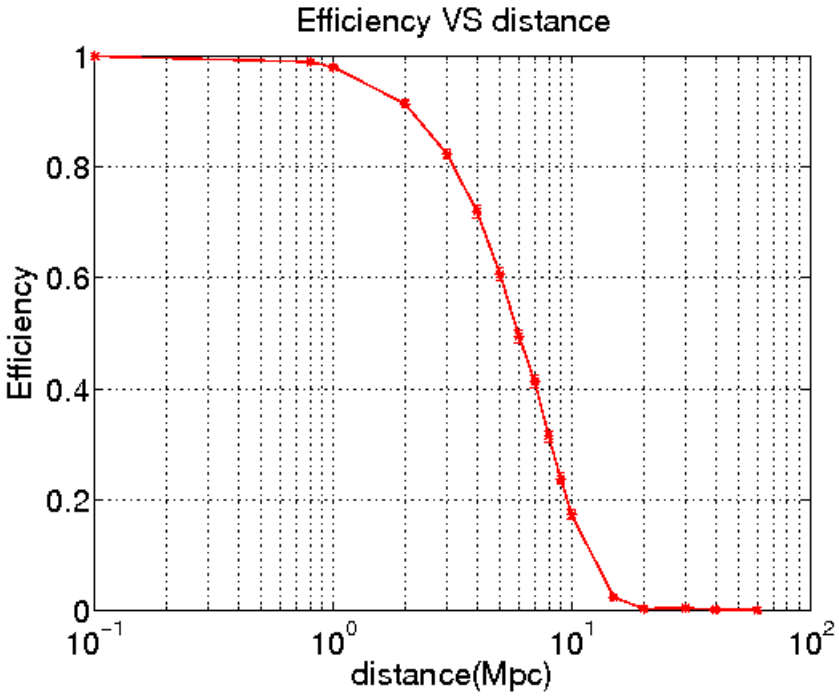

Figure 4.10: The efficiency curve associated to an ADI waveform (see next chapter for a definition of ADI signals), It goes from 1 when injections are done at low distances (very strong signals), to 0 when the injections are done at great distances (very weak signals). The 50% efficiency is here reached at 6.0 Mpc.

Chapter 5

S5 analysis

"Mieux vaut allumer une bougie que maudire l'obscurité."

Proverbe chinois (?)

In this chapter we will present the first results obtained using the STAMPAS pipeline. We will first introduce the data set we used to run the analysis, then describe the waveforms used for tests purposes, and finally describe the post-processing of the data given by STAMPAS.

5.1 Dataset

The data we used are taken from the fifth science run of the LIGO experiments (later referred to as S5), which took place from November 4th 2005 to October 1st 2007 [3]. During this period, we are only interested in times when data has been acquired by the two detectors simultaneously. These time periods will be referred to as *science segments*. Inexploitable data from H1 and L1 have also been removed (see 5.4.1 for details).

STAMPAS uses data from a couple of interferometers. To run the first STAMPAS study so far, we decided to only use the pair H1L1. The LIGO interferometers are equally sensitive, and had globally a better power spectral density than

Virgo during this time period. Furthermore, the common data acquisition periods between H1 and L1 was much greater than between V1 and any LIGO experiment (respectively about 1 year and two months) during S5.

We removed (or notched) from the analysis – *i.e.* from the *ft*-maps – a list of frequency lines, which are known to be subject to high non-stationary noise[1]. Among them are notched 60Hz harmonics, violin modes or calibration lines [3]. The STAMP statistics were not calculated at these frequencies, and they were ignored during the trigger search.

In figure 5.1a, is shown a typical noise spectral density of H1, H2, L1 and V1, and in figure 5.1b is presented a curve retracing the evolution of the overall sensitivity of the different experiments during S5, using a figure of merit called *horizon distance*. The horizon distance is the distance to which each experiment is sensitive to a specific signal, here a binary coalescence during the end of the inspiral phase, with SNR = 8 (in amplitude) and with an optimal orientation of the detectors.

Furthermore, we use time windows 500s long, so science segments shorter than 500s haven't been considered for the analysis.

5.2 Background estimation

5.2.1 The timeshifts method

When a pipeline returns a trigger, we have to be able to know if this trigger is due to noise, or if it has a reasonable chance of being the signature of a genuine gravitational wave. It is therefore crucial to characterize the noise background of the data.

To do this the simpler method would be to study a subset of data, where we know that no gravitational wave is present. This is in our case impossible to accomplish. Indeed, STAMPAS is an all-sky pipeline. It is interested in signals

[1]List of notched frequencies: 57, 58, 59, 60, 61, 62, 63, 118, 119, 120, 121, 122, 178, 179, 180, 181, 182, 239, 240, 241, 328, 329, 330, 331, 341, 342, 343, 344, 345, 346, 348, 349, 599, 685, 686, 687, 688, 689, 690, 691, 692, 693, 694, 695, 696, 697 and 959 Hz

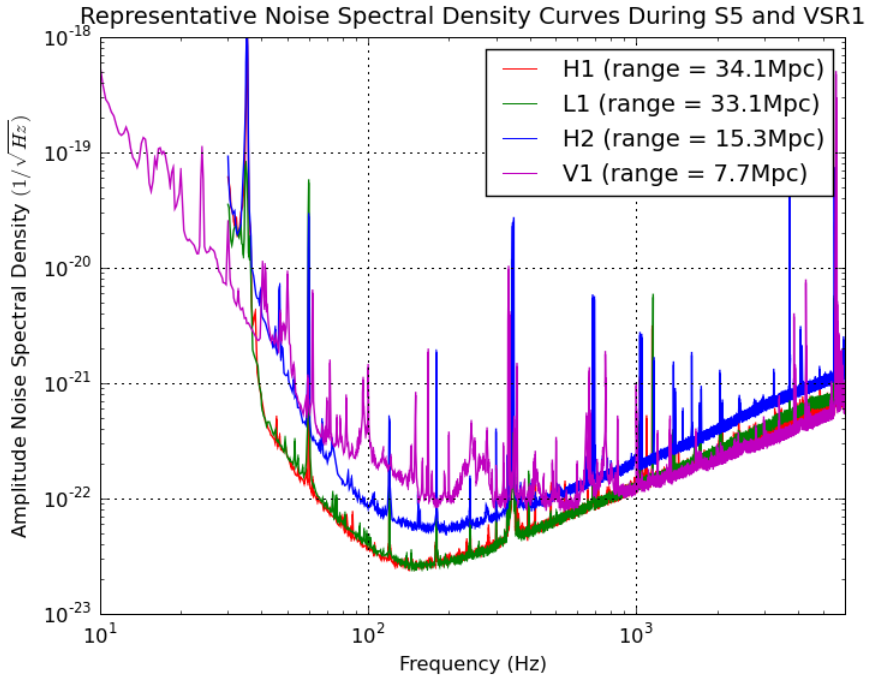

(a) Typical noise spectral density of H1 (red), H2 (blue), L1 (green) and V1 (purple), during S5 [84]. These spectral density curves correspond to July 21, 2007 (GPS 869040003) for H1, March 16, 2007 (GPS 858087370) for L1, September 30, 2007 (GPS 875211248) for H2 and June 13, 2007 (GPS 865748914) for V1.

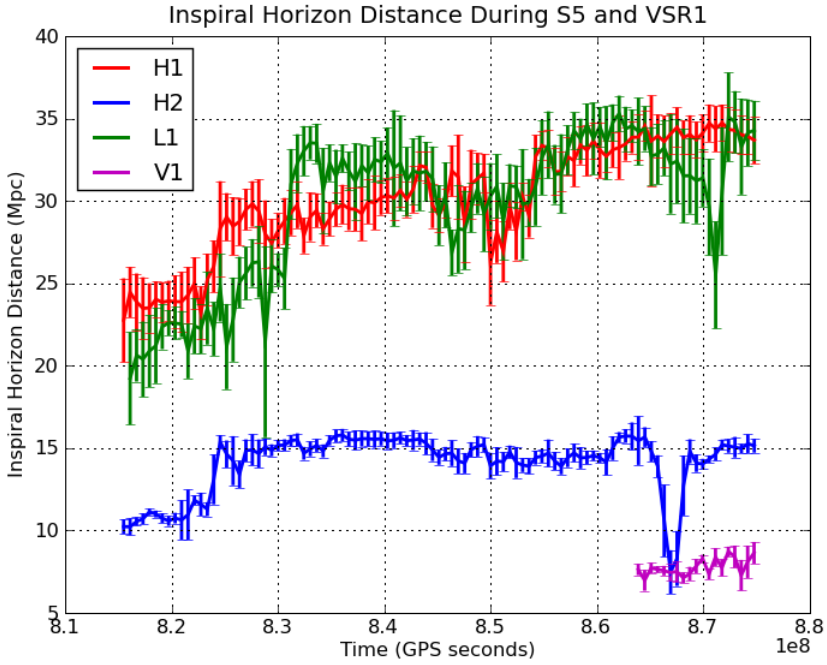

(b) Average inspiral horizon distances for each week in S5 and Virgo first science run (VSR1), for H1 (red), H2 (blue), L1 (green) and V1 (purple) [84].

Figure 5.1: Figures illustrating the network sensitivity during the S5 science run.

coming from every direction in the sky, happening at any moment. We cannot guarantee that no signal is present, no matter the time segment we study.

To study the background, we use a classical technique in gravitational wave data analysis, which is called the *time slide*. To obtain a dataset without any gravitational wave signal present in it, we apply before correlating the data of the two interferometers, a time shift T_0 between each data set. For a given time shift, the cross-correlation of the two data sets gives

$$C_{IJ}^{timeshifted}(\tau, f) = 2\tilde{s}_I^*(\tau, f)\tilde{s}_J(\tau + T_0, f) \tag{5.1}$$

using the same notation as equation (4.4). If the time shift T_0 is longer than the maximal duration T_{max} of the signals we expect, then any significant value of $C_{IJ}^{timeshifted}$ will be due to noise. Any correlation due to gravitational waves is suppressed in the process.

It is possible to show [85, 86] that the triggers generated with timeshifted data behave like an independent realization of the background. This realization will be called a *lag* or a *timeslide*. It is therefore possible to use such data to estimate the noise in this study. This method has an other advantage: despite the fact that our dataset is limited, it is possible to increase its size – also called *lifetime* – by doing several time shifts on the data. If the time difference T_{ij} between time shift i and time shift j is superior to T_{max}, each lag is independent, and its results can be added to the others. Even if the background estimation accuracy cannot be increased indefinitely by performing more timeshifts, as shown in [85, 86], the gain in effective lifetime can be substantial.

In STAMPAS, this method is implemented as follows: the science segments on which we analyze are divided in 500s long windows, overlapping with each other by 10s. The data present at the end of the initial science segments is not used if it can't form a 500s window. This science segments are noted n_i with $i \in [1, N_{tot}]$. In table 5.1 we estimate the loss of data induced by this procedure. The lag l is generated by correlating data from interferometer I from science segment n_i with data from interferometer J from science segment n_{i+l}. The correlated data are *at least* $500 \times l$ seconds apart. The timeshifts are made circularly, *i.e.* when

running the lag p, when the correlation of segments n_i and n_{i+p} is not possible because $i + p > N_{tot}$, then segment n_i will be correlated to segment $n_{i+p-N_{tot}}$.

	Lifetime (years)	Percentage of available data
S5 science time (H1L1)	0.91	100
S5 science segments (H1L1, duration> 500s)	0.82	90.94
Analyzed science segments (zero lag)	0.75	82.18
Total background lifetime (with 200 lags)	149.62	16440

Table 5.1: Lifetime of available data, with different selection.

Note here that the variable windows algorithm can change the duration of the science segments analyzed. This change does not affect the time separation between segments n_i and n_j, because both their sizes are modified by the algorithm.

5.2.2 Computing requirements

We run the background studies on the Caltech computing center. We had at our disposal, on average, 300 computing nodes with 2400 Mb of memory each. To run the entire study, 10 real days were necessary.

5.3 Waveforms and Injections

5.3.1 Waveforms

To study the efficiency of the pipeline, we selected first two families of simulated signals: Accretion Disk Instabilities (ADI) waveforms, for which the model (from Van Putten) is described in [59, 87] and waveform generator is described in [88]; and Eccentric Binary Black Holes waveforms (EBBH), described in [67] and which analytic generator, called *cbwaves* can be found at [89].

The ADI waveforms based on the Van Putten model have a simple chirp behavior, and variable extension in time and frequency. They are good benchmarks for a long-transient search. It has to be noted though that the analytic model

we use, according to its creators [88], may be far from actual ADI signals, which will also be the case of the limits we will set on these signals.

The EBBH waveforms are physically relevant waveforms, but with complexity which prevents them, at the time of writing, to be used in standard transient pipelines using match-filtering techniques. They are quite different in morphology: a succession of short signals progressively leading to an inspiral waveform, with several harmonics present in the time-frequency map.

In figure 5.3 are presented *ft*-maps with the 5 set of parameters chosen for each waveform family. On tables 5.2 and 5.3, are presented the main characteristics of each waveforms.

5.3.2 Injections

With these 10 waveforms, 1500 injections per waveform per distance has been performed randomly over the whole S5 run, using the protocol introduced in 4.2.5. 17 different distances, from 0.1 Mpc to 60 Mpc have beem tested. These injections has been performed on time shifted data.

5.4 Post-processing

For the S5 analysis, we used 200 different time slides. The effective lifetime was ~ 150 years.

The list of triggers obtained underwent a first selection: since for each time window investigated, 5 different sky positions were used, it is possible that some triggers have been counted several times. To take into account this effect, for a given frequency-time time, several triggers are coinciding in time and frequency, only the stronger is conserved.

After this first selection, it is possible to visualize the background distribution by plotting the *False Alarm Rate* (FAR) curve: FAR(SNR). FAR(s) is the number of background triggers which SNR is superior to s, divided by the total *lifetime*. It estimates the rate of "false alarms" we would have if we considered each trigger with SNR $> s$ as a gravitational wave candidate. Plotted in figure

Waveform (ADI)	M ($M_\odot$)	a^*	ε	m_{disk} ($M_\odot$)	Duration (s)	Frequencies (Hz)	d_{SNR40} (Mpc)
A	5	0.3	0.05	1.5	39	135-166	3
B	10	0.95	0.2	1.5	9.4	110-209	35
C	10	0.95	0.04	1.5	236	130-251	15
D	3	0.7	0.035	1.5	142	119-173	0.5
E	8	0.99	0.065	1.5	76	111-234	20

Table 5.2: Physical characteristics of the ADI waveforms (Van Putten model) used as injections. M is the central black hole mass, a^* the dimensionless Kerr spin parameter of the central black hole, ε the fraction of disk mass that forms clumps, m_{disk} the mass of the accretion disk [88], and d_{SNR40} the distance at which the waveform leads in average to a trigger of SNR 40 with STAMPAS.

Waveform (EBBH)	M_1 ($M_\odot$)	M_2 ($M_\odot$)	ε	Duration (s)	Frequencies (Hz)	d_{SNR40} (Mpc)
A	2	2	0.99	100*	40-370	8
B	4	3	0.91	100*	40-250	9
C	8	3	0.96	100*	40-240	13
D	6	6	0.94	100*	40-220	15
E	18	10	0.85	24.1	40-113	7

Table 5.3: Physical characteristics of the EBBH waveforms used as injections. In the RMKI group model [89], M_i are the masses of the two black holes, ε is the initial eccentricity of the binary orbit, and d_{SNR40} the distance at which the waveform leads in average to a trigger of SNR 40 with STAMPAS. $*$: waveforms used set to be 100s, even though they can be physically much longer.

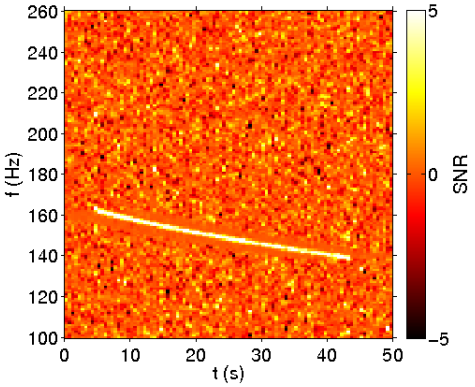

(a) ADI A waveform

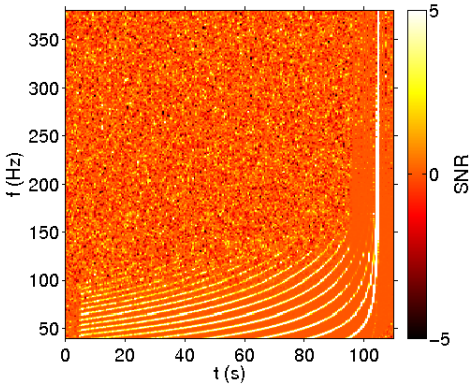

(b) EBBH A waveform

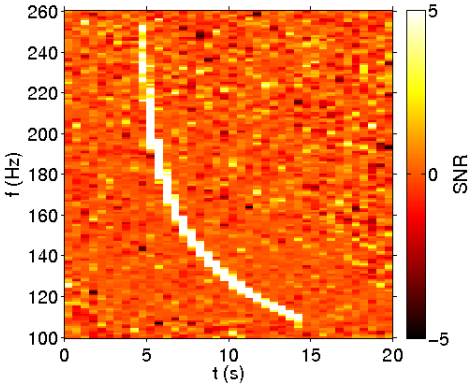

(c) ADI B waveform

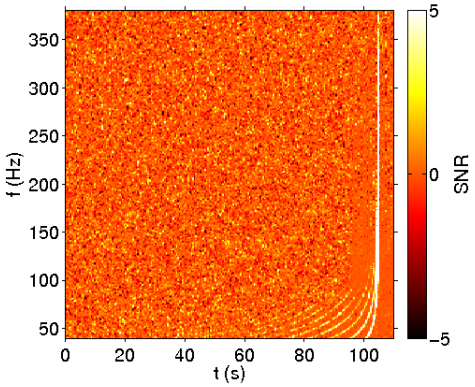

(d) EBBH B waveform

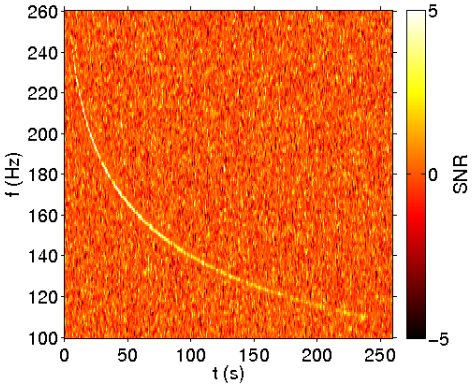

(e) ADI C waveform

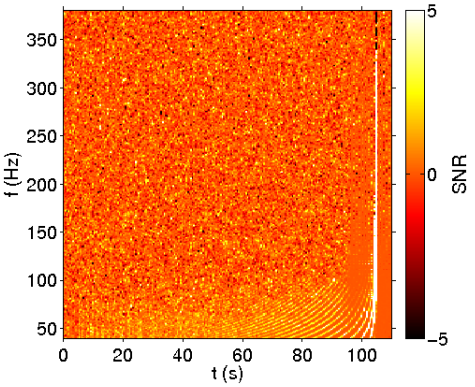

(f) EBBH C waveform

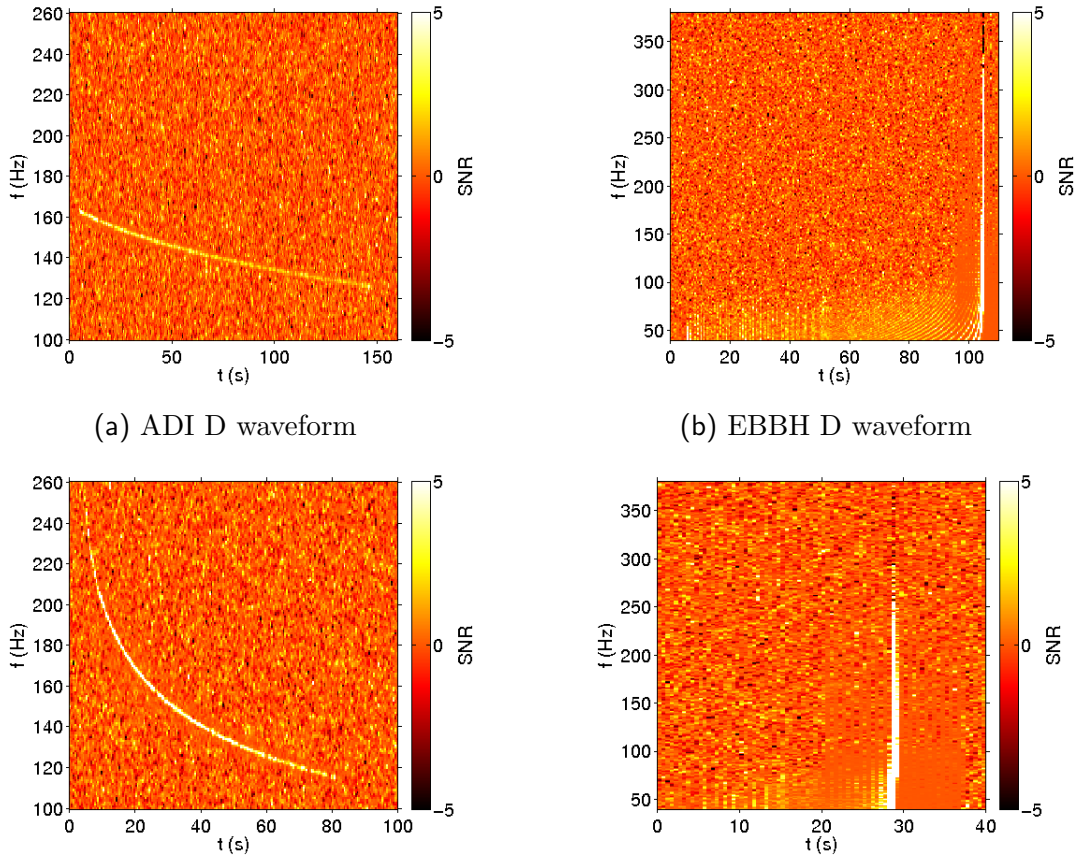

(a) ADI D waveform

(b) EBBH D waveform

(c) ADI E waveform

(d) EBBH E waveform

Figure 5.3: ADI and EBBH waveforms injected in gaussian noise. The time scale is different for every injection, but the frequency range is identical for each waveform family. In EBBH waveform maps, the presence of several distinct chirps is due to the presence of strong high-order harmonics in the waveform.

5.4 is the FAR curve with no data selection other than the suppression of the redundant triggers. For comparison purposes, the same curve has been plotted using triggers issued from 2 weeks of simulated data, with 100 timeshifts. Around SNR 30, the grey curve deviates from the expected behavior of the background in the case where the noise has a gaussian distribution. This is due to the presence of non-gaussian triggers in the data, or glitches. The purpose of the post-processing is to remove as many of these loud triggers as possible by using selection methods which affect glitches and not physical signals.

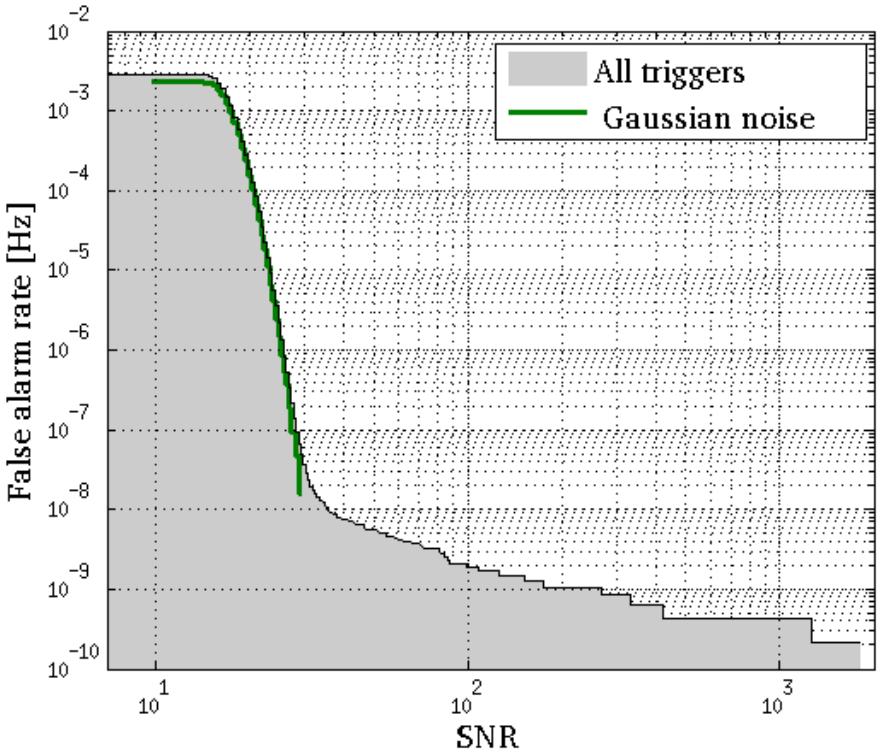

Figure 5.4: FAR distribution obtained without prior trigger selection, for real and simulated data. Let us remember here that the SNR is an "energy" SNR.

In appendix A can be found the list of the 100 loudest background triggers, along with their characteristics and the cuts applied on them.

5.4.1 Data quality flags selection

It is possible that the triggers present in the data are caused by known features of the data. As explained in section 2.3.4, technical problems or environmental perturbations can induce strong responses in the dark fringe channel of one interferometer. These power outbursts can be mistaken for a genuine signal. In our case, if two power excesses happen at the same time (taking into account a potential time shift of the data) in two different interferometers, the cross-correlation of the data will certainly show an excess which could result in the generation of a trigger in the STAMPAS output. It can also be the case if only one interferometer shows a power outburst, if it is strong enough, because of a large random event in the other interferometer.

The Virgo and LIGO interferometers are equipped with numerous sensors designed to characterize the environment of the experiments, and to find correlations between power seen in the dark fringe and environmental conditions. When such correlations are detected, the time periods when the dark fringe signal may have been influenced by an environmental or a technical source are identified. These identifications are called *data quality flags* (DQs): they consists of several lists of time where a set of sensors had an abnormal behavior, which are known to be causally connected to fluctuations in the dark fringe channel. These flags, which generation is completely independent of STAMPAS, are gathered in different categorize, depending on the importance of the disturbance they point:

- **Category 1 flags (CAT1):** these flags correspond to periods of severe problems (data missing, calibration failure, control of the interferometer lost...). Data collected during these periods are not used.

- **Category 2 flags (CAT2):** these flags correspond to periods where large glitches are present in the data, with a clearly understood origin. These glitches affect differently the different search pipelines. It is possible to analyze CAT2 data when the effect of these glitches is limited. CAT2 data has been analyzed with STAMPAS: a great part of CAT2 data are

contaminated by very short glitches, which when they are not too strong, have a low impact on the pipeline.

- **Category 3 flags (CAT3):** these flags correspond to periods where the origin of the glitches present is partially understood or whose effect is limited (nearby trains, moderate seismic motion...). Triggers obtained during these periods are considered with caution.

- **Category 4 flags (CAT4):** these flags correspond to periods where *hardware injections* has been made. The mirror position is at that time, controlled to mimic their behavior in case of a gravitational wave pass through the detector. These injections are used, among other things, to check that the pipeline are ready for the detection, and that their data selection process is safe. Such periods where not analyzed

A first DQ selection

To remove the distribution tail we observed previously, we listed the 100 loudest background triggers we had (see appendix A), and we looked for coincidence with all the data quality flags list at our disposal. If we can prove that such coincidences are physically generated *i.e.* that the disturbance which turned a data quality flag on is the same that provoked a power excess in an interferometer, then we will discard all the triggers coinciding with this data quality flag.

To prove that the coincidences we observe are not accidental, we also compare the data quality flags lists to unphysical lists of triggers so the we estimate the number of accidental coincidences. Practically we apply several time shifts on the H1 and L1 GPS times of the background triggers we use, to obtain several "fake" lists of triggers, and we look for coincidences between these fake lists and the data quality flags. Given that this study is done on a limited sample of triggers, we consider that to be significant, a data quality flag must veto at least two more triggers from the real list of triggers (which are still issued from time shifted data) than any shifted list. Data quality flags which only veto one true trigger, but absolutely no "false" trigger, are also considered. If one of these

conditions is fulfilled, we select this data quality flag, and we use it as a veto. We also check that the amount of data flagged by it – the *deadtime* – is reasonable *i.e.* that applying these flags as vetoes would not make us lose too much data. Practically we made sure that none of these flags had a deadtime superior to a few percents of the zero lag lifetime.

Note here that the trigger list we use is issued from the background analysis, *i.e.* from timeshifted data. It means that to each trigger is associated to a different time in H1 and L1. Hence H1 DQ flags are compared to the H1 GPS of the triggers, and L1 DQ flags are compared to the L1 GPS of the triggers.

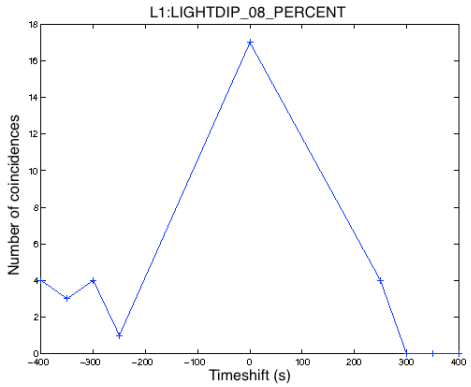

(a) Example of a data quality flag which flags significantly more the genuine triggers list than the others. Can be used as veto.

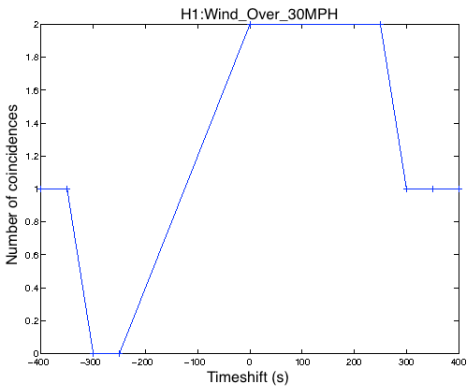

(b) Example of a data quality flag which doesn't flag more the genuine triggers list than the others. Not used as veto.

Figure 5.5: Example of plots made to check the safety of the data quality flag with respect to the STAMPAS pipeline.

In figure 5.5 you can see examples of the plots which have been made, for each data quality flag, in order to select the relevant triggers. They indicate the number of coincidences between the corresponding data quality flag and the triggers lists given their timeshifts (time shift 0 corresponds to the genuine trigger list).

The cumulative deadtime of the selected data quality flags is 194.95 hours in H1 and 217.98 hours in L1. This represents respectively 2.98 % and 3.34 % of the zero lag lifetime.

We must note here that to be perfectly unbiased, the selection of the DQ flags should have been performed on a set of triggers different from the set eventually used for the background estimation. For example we could have processed 200 more timeslides and apply the DQ selected to the new list of triggers. During the selection process, we first used the described method on the first 100 timeslides, and applied to results to a different set of 100 timeslides. Even though background reduction was not, as could be expected, as good as what we obtained by doing the selection on the 200 timeslides, results did not vary much. Furthermore, as we will see in sections 5.4.2 and 5.4.3, as well as in appendix A, the influence of the DQ selection on the triggers remaining after the entire selection process is small. Therefore the DQ flags selection bias will not affect significantly the results of the search.

A complementary DQ selection

The data quality flags (DQs) selection made above is based on coincidence between DQ flags and the 100 loudest background events. However many noise sources didn't generate triggers in STAMP thanks to the internal glitch cut. No trigger corresponding to these sources could have is in the DQ selection process, although they are interesting to select DQs. Such noise sources could, in the zero lag, generate a trigger passing the selection thresholds, while it would be possible to remove them using the proper DQ.

To identify these noise sources, coincidences between DQ times and glitch cut activation times are studied in order to see which additional DQs are selected using background triggers already eliminated by the glitch cut. For each glitch cut activation, STAMPAS returns the interferometer more likely to have caused the power excess. We have therefore two lists of glitch cuts activation times, one for H1 and one for L1. The H1 list will be compared to the H1 DQ flags times, and the L1 list to the L1 DQ flags times. About 500 and 50000 activation times have been found for H1 and L1 respectively.

As it is done during the first selection, we compare DQs times to a genuine list of "glitch cut triggers" and several fake lists. However the criteria used to select

DQs are a bit different from the criteria previously used. Indeed, the number glitch cuts activation times is much greater than the number of events we used with the first selection. Are selected DQs which are such as:

- the number of "glitch cut triggers" flagged with the genuine list of glitch cuts, N^{true}, verifies

$$N_{true} - \sqrt{N_{true}} > \max(N^i_{false}) \tag{5.2}$$

  with N^i_{false} is the number of coincidences between "glitch cut triggers" and DQs with the ith fake "glitch cut triggers" list,

- their average duration is inferior to 2000 s,
- their deadtime is inferior to 300 hours,
- they are not already part of the first DQ selection.

The cumulative deadtime of this second selection of flags is 710.83 hours in H1 and 487.29 hours in L1. They represent respectively 10.88 % and 7.46 % of the zero lag lifetime. This second selection of data quality flags has a long deadtime. If we were to apply these vetoes blindly, we would lose a significant amount of lifetime, which would decrease the search efficiency. Therefore we decide not to apply this second selection of trigger blindly. However, any event candidate flagged by one of the DQs selected here will be considered with caution.

5.4.2 SNR fraction cut

Most of the glitches we observed have a short duration. Due to the clustering algorithm, they can appear longer, but their power is essentially concentrated at a very specific time. This behavior is significantly different from the signals we expect. We can use it to discriminate noise triggers from signals. For each trigger, STAMPAS calculates the sum of the SNR of each individual pixel constituting the cluster (which is different from the SNR cluster), SNR_{sum}. STAMPAS also calculates for each time unit – each column of the *ft*-map – the sum of the pixels

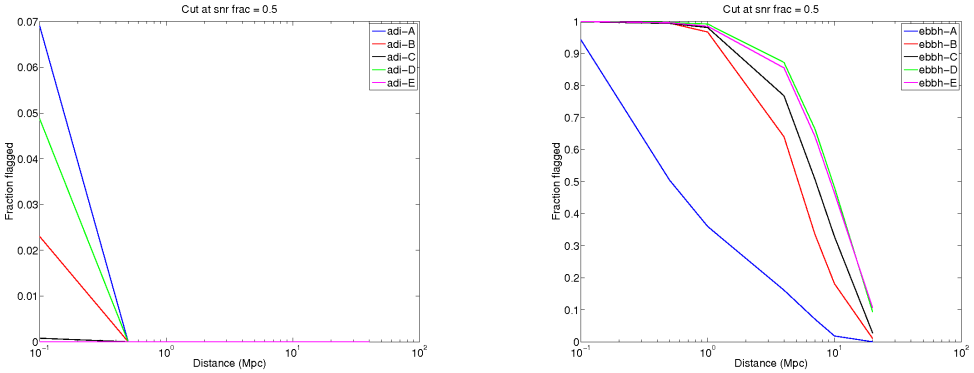

(a) Proportion of ADI injections which SNR_{frac} value is above 50% depending on the waveform amplitude.

(b) Proportion of EBBH injections which SNR_{frac} value is above 50% depending on the waveform amplitude.

Figure 5.6: Example of plots made to check the safety of the data quality flag with respect to the STAMPAS pipeline.

individual SNR: $\mathrm{SNR}_{sum}(\tau)$. If for a single column τ, the so-called *SNR frac* ratio $\mathrm{SNR}_{frac} = \frac{\mathrm{SNR}_{sum}(\tau)}{\mathrm{SNR}_{sum}} > X\%$, then the trigger is considered as a glitch, and vetoed. We have chosen $X = 50\%$ to remove as many loud triggers as possible, which weren't already flagged by data quality flags, without significantly affecting the injections.

This procedure makes a rather good distinction between noise and ADI signals. Indeed, we performed a preliminary study, making 1000 injections on MC noise, for each of the 5 ADI waveforms tested and for different amplitudes. Only a low percentage, for a single waveform at the highest – unrealistic – amplitude, of injections has been been flagged. In figure 5.6a are shown the results of the safety study.

The same studies performed on EBBH waveforms however have shown, see 5.6b, that these waveforms have a high maximal SNR_{frac} ratio. Indeed, the main part of the energy in these waveforms is concentrated in the last seconds. Using a selection based on the SNR fraction quantity would decrease greatly STAMPAS sensitivity to EBBH signals. The situation is not significantly improved with higher values of the SNR_{frac} threshold (see figure 5.7).

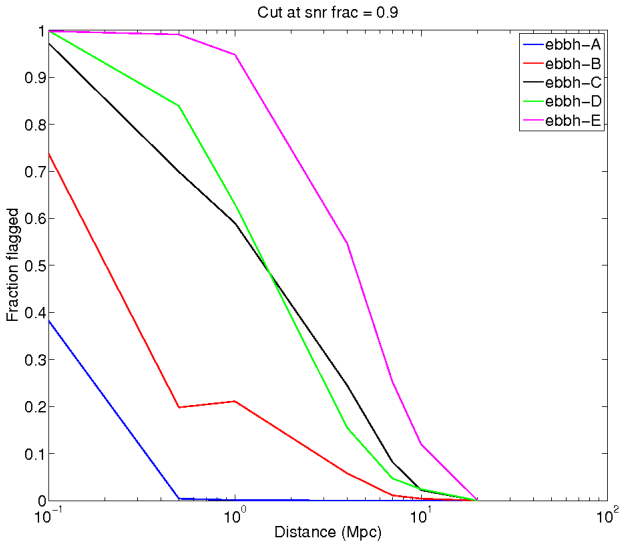

Figure 5.7: Proportion of EBBH injections which SNR_{frac} value is above 90% depending on the waveform amplitude. The proportion of affected injections is still very high. Only weak signals are not affected by the cut.

Using the SNRfrac quantity to select background events seems therefore a poor choice if we want to search for EBBH signals. Therefore we decided to split up our analysis in two: a first will be done using the SNR fraction as a cut with a 0.5 threshold, and will be referred to as the primary analysis. The second analysis using a threshold of 0.99, which increases the background but is sensitive to EBBH signals, will be referred to as the EBBH analysis.

The reason why we decided to apply a 0.99 threshold for the EBBH analysis is because the loudest background event not vetoed by a data quality flag (event number 2 in appendix A) has a SNR value of 1262.78. This is an extremely high value. The next background trigger not vetoed by a DQ is event number 7 in appendix 5.1, which has a SNR of 267.07. Removing the loudest background event hence would considerably reduce the background distribution tail for the dedicated EBBH analysis. The SNRfrac value of the loudest event is 0.99. The efficiency calculations (results are shown in section 5.4.5) will demonstrate that setting a SNRfrac threshold of 0.99 only affects the efficiency of very strong

signals (see figure 5.16b) – which observation is unlikely – and is therefore still safe to be applied.

5.4.3 Final distribution and loudest events

In figures 5.8a and 5.8b the FAR distribution is shown calculated with all the selection procedure applied. In the case of the primary analysis, it can be seen that the distribution, all selections applied, is close to what could be expected of a gaussian distribution. The background is very well understood.

The loudest remaining trigger in the primary analysis is presented in figure 5.9. Its SNR is 38.36, and looking at the dark fringe channel at the time of the trigger (figure 5.10), it seems to be due to the correlation of a short glitch in H1, with a noisy period in L1 at the same time (time shift taken into account).

5.4.4 Background properties

In this section we show how the background triggers are located in the parameter space.

The plots in figure 5.11 show the correlation between the various parameters (duration, average frequency[2], SNR,...) of the background triggers.

What can we deduce from such plots? 5.11a shows the trigger rate was stable during the run. Very loud triggers have well been removed, and where present homogeneously in the dataset. From plot 5.11b we see however that the longest signals are concentrated around 300 Hz, it is therefore possible that at some point during the run, some frequencies around 300 Hz went noisier for a short period of time. From 5.11c, we see that the triggers have essentially small durations and that they seldom last for more than 80s. From 5.11d, we see that the noise level is identical on average at every frequency, and that the loudest triggers were low frequency triggers ($f_{mean} < 200$ Hz). Finally, figure 5.11e shows the impact of the SNR frac cut on the background distribution.

[2]The frequency of a trigger is the mean between its minimal and maximal frequencies.

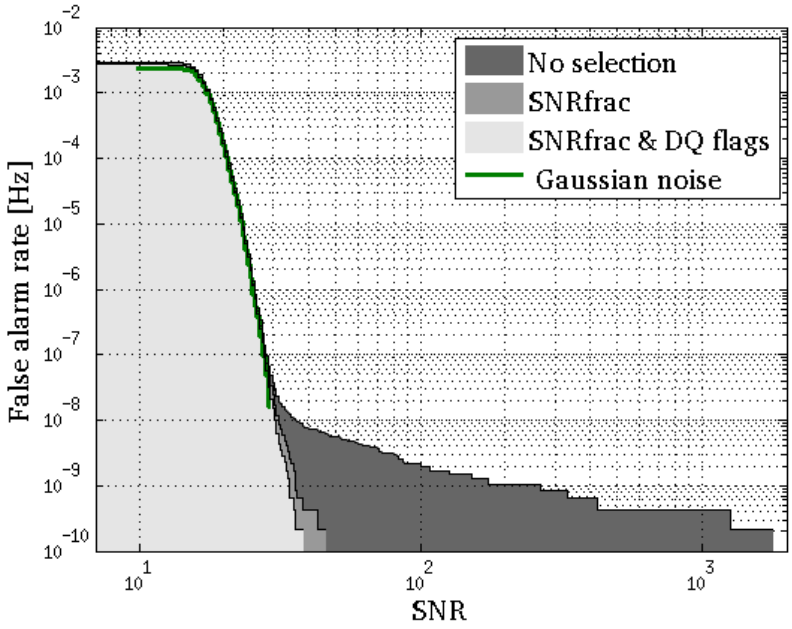

(a) FAR distribution obtained for the primary analysis with different trigger selection.

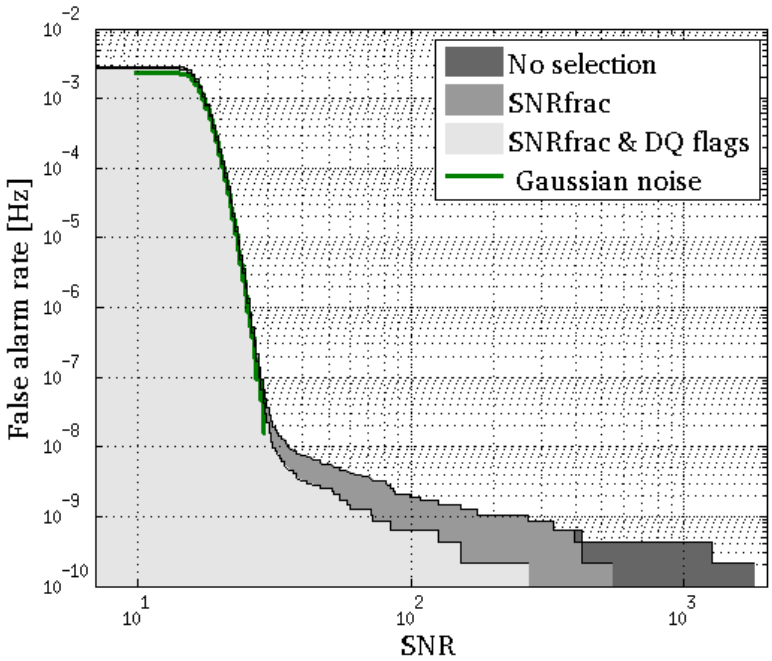

(b) FAR distribution obtained for the EBBH analysis with different trigger selection.

Figure 5.8: FAR distributions for the primary and the EBBH analyses. The light grey curve presents the FAR distribution without any selection, then the medium grey curve presents the distribution obtained when the data quality flags are applied as vetoes, and the darkest grey curve presents the distribution with both vetoes and triggers with an SNR fraction of less than 50 % for the primary analysis, and 99% for the EBBH analysis. The green curve is the distribution associated with MC data.

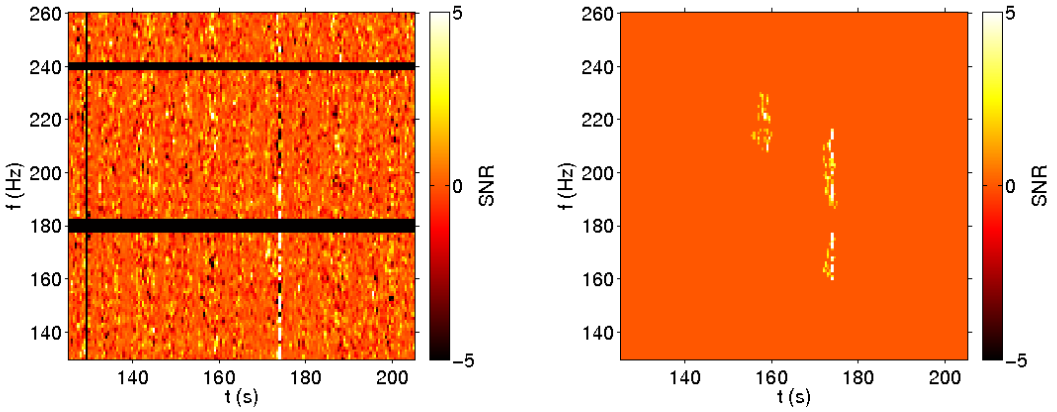

Figure 5.9: Left: STAMP *ft*-map of the loudest event, zoomed on the trigger. Right: the same map presenting only the pixels belonging to the trigger.

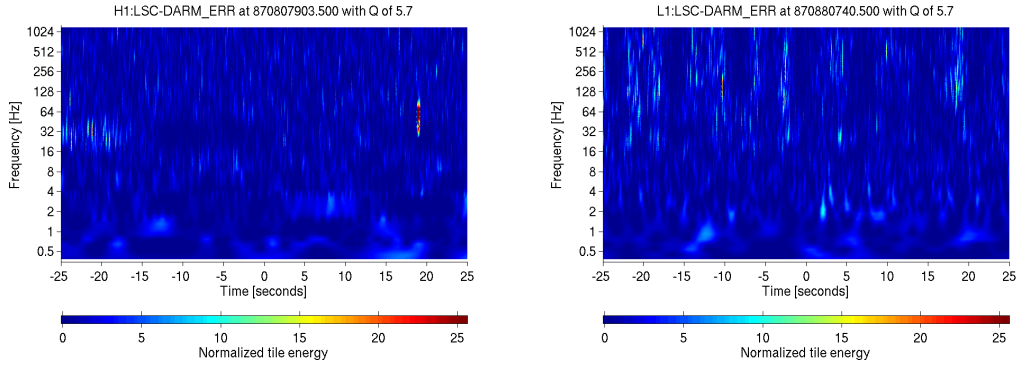

(a) H1 dark fringe channel *ft*-map

(b) L1 dark fringe channel *ft*-map

Figure 5.10: H1 and L1 dark fringe channels at the moment of the loudest background trigger of the primary study.

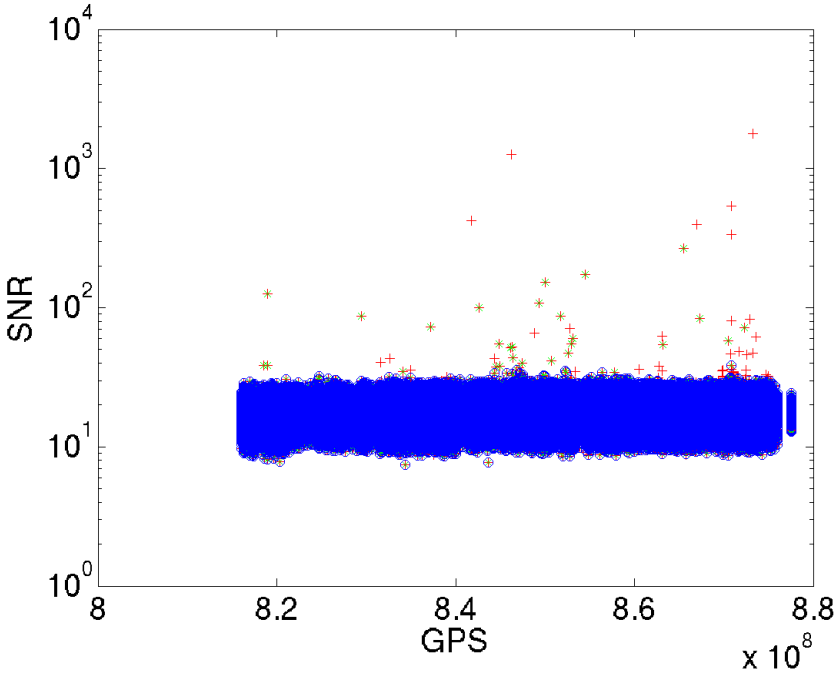

(a) SNR vs. GPS time of the triggers.

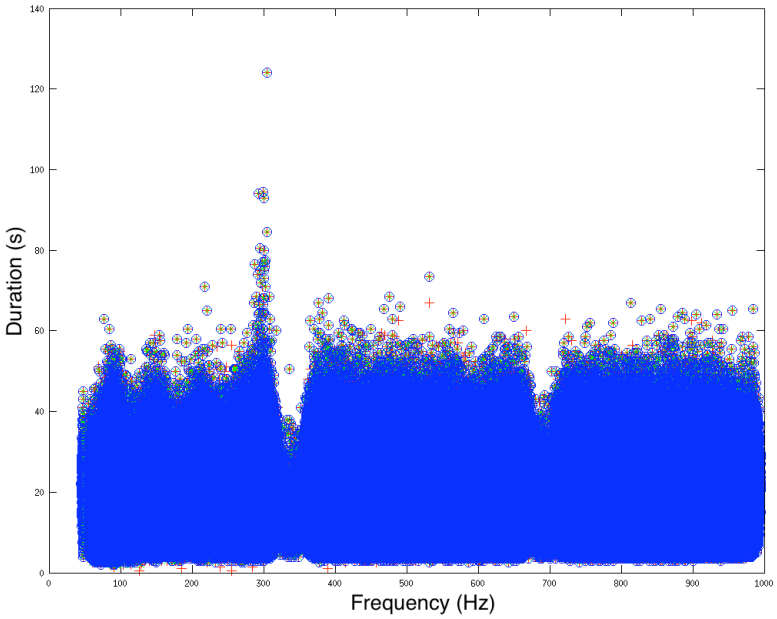

(b) Duration vs. Frequency of the triggers

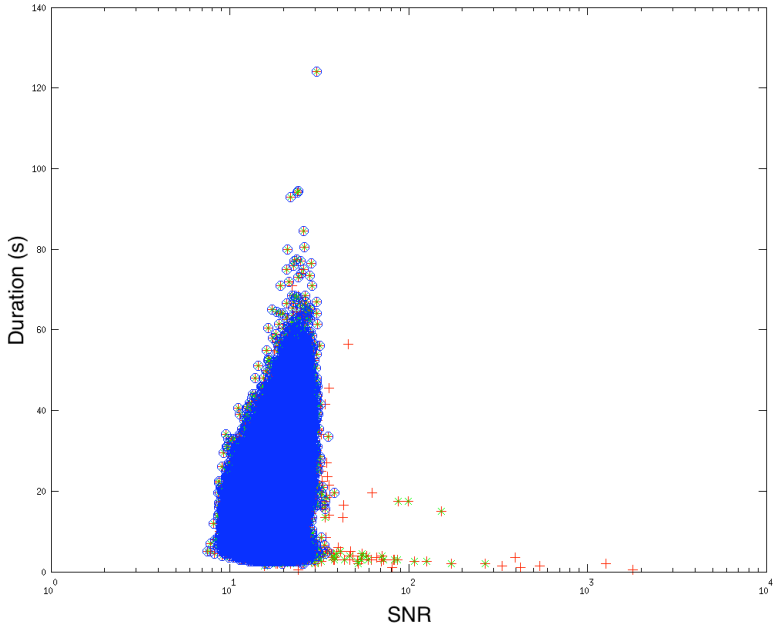

(c) Duration vs. SNR of the triggers

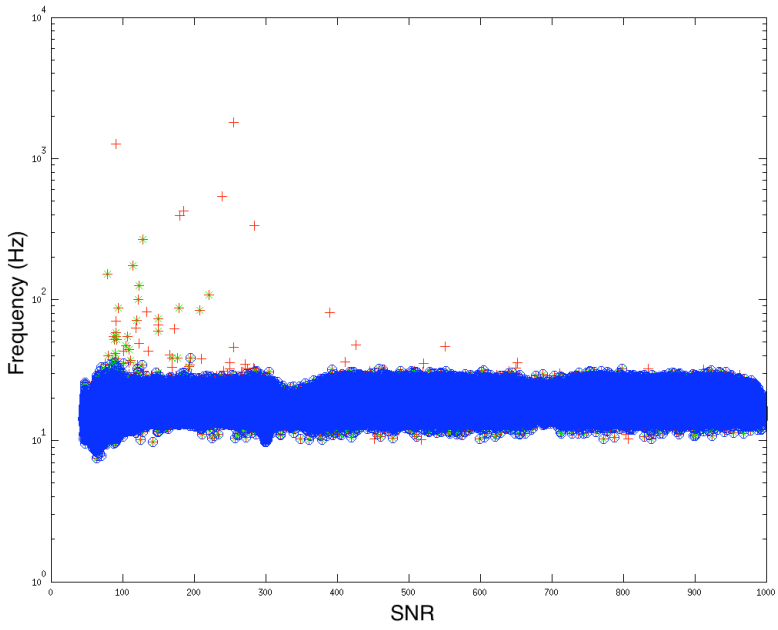

(d) Frequency vs. SNR of the triggers

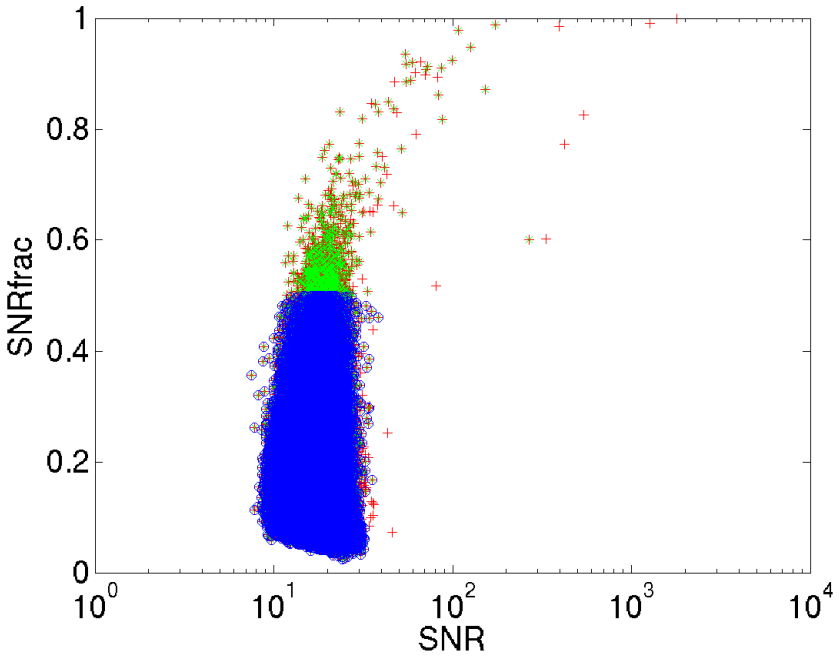

(e) SNR frac vs. SNR of the triggers

Figure 5.11: Various views of the parameter space covered by the background triggers. The red points represents the entire set of triggers, the green ones the trigger which passed the EBBH study's selection cuts, and the blue ones the triggers which pass the primary study's selection cuts.

Such plots can be used to better remove background triggers, by identifying their properties. As an example, we can see that if we only consider ADI-like signals, we may want to consider removing the triggers of duration smaller than 4-5s, knowing that ADI are recovered with higher duration. It turned out that this cut wouldn't affect loud background triggers, and wouldn't help us gain in sensitivity.

For the study, we considered that the data quality flags and the SNR fraction cuts were sufficient, and we didn't use any other selection procedure.

5.4.5 Efficiency studies

To estimate the ability of the pipeline to detect gravitational waves signals, one can plots efficiency curves. Using the results from the background study, we select an SNR threshold which must be applied on the triggers to obtain the lowest possible FAR. In practice we chose the SNR of the loudest event in the background distribution after all selection cuts are applied.

Among the recovered injections, we select only those which SNR is above this threshold. We also apply the same selection procedure (SNR fraction, data quality flags) as we applied to the background. Then we plot, for each waveform, the ratio of the number of recovered injections above the threshold, over the total number of injections, which is called *detection efficiency*. The plots represent the evolution of this ratio with the amplitude of the injected waveform (here indicated as a distance to the source of the injected signal).

Efficiency plots are made for both the primary and the EBBH studies. We present first on figure 5.12 the efficiency curves of the ADI waveforms.

On figure 5.12, we can notice three effects. First, a very strong injection should be detected no matter the conditions, which is why the curves should converge to 1 for low distances/strong amplitudes. It is not the case here because of the data quality flags vetoes, which can accidentally flag strong injections.

The observed rates, presented in table 5.4, are compatible with the DQs deadtime, 2.98 % for H1 and 3.34 % for L1. The differences of flagging rate can be explained because data quality flags are not exactly randomly distributed,

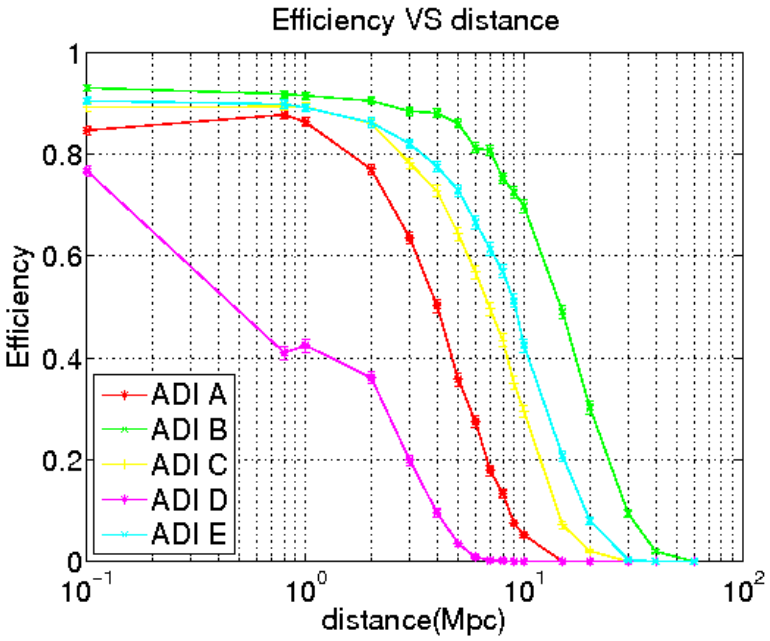

Figure 5.12: The detection efficiency curves obtained for the five ADI waveforms, with all data selection procedures applied. SNR threshold for detection is 38.36.

Waveform	Observed rate
ADI A	8.8%
ADI B	5.1%
ADI C	10.7%
ADI D	13.7%
ADI E	9.5%

Table 5.4: Observed percentage of lost injections due to data quality flags.

and because the waveforms do not have the same duration. In figure 5.13 the same curves are presented, without applying the data quality vetoes.

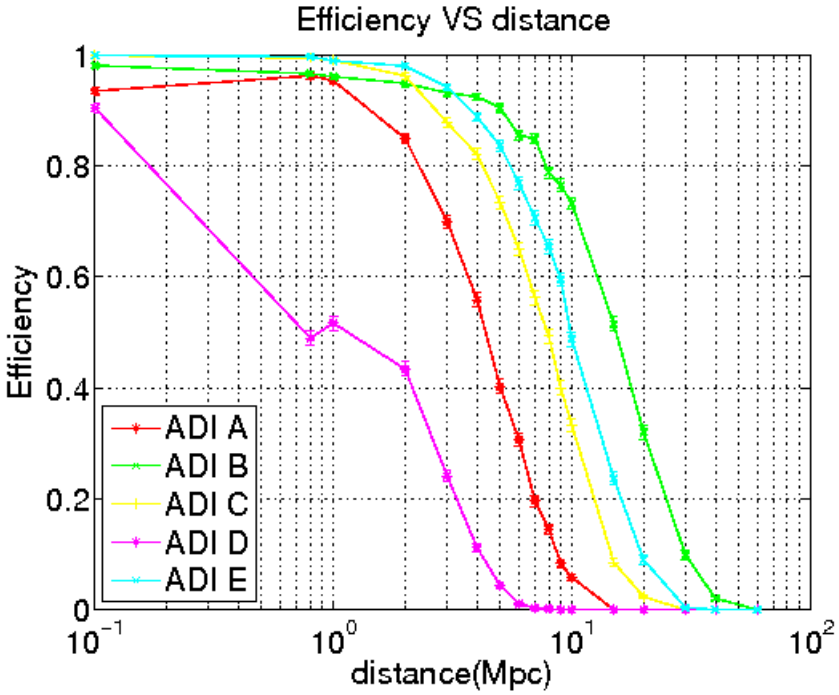

Figure 5.13: The efficiency curves obtained for the five ADI waveforms, without applying the data quality vetoes

The curves corresponding to the C and E models seem normal. The ADI A curve indicates missed injections at 0.1 Mpc not due to data quality flags. This is due to a known numerical artifact in STAMP, which increases the power at the beginning and the end of ADI injections. If enough power is present at the edges of the injection, the SNR frac value of the impacted signal will be increased, and therefore the injections may not pass the SNR frac cut. This effect impacts all the different waveforms, but not with the same amplitude. In table 5.5 are summarized the proportion of 0.1 Mpc injections removed by the SNR frac cut. Anyhow, the loss appears only for injections done at 0.1 Mpc[3], which

[3]In fact some ADI B injections are also affected at different distances, the effect is however marginal (less than 0.5% for every distances) and is likely due to the fact that ADI B triggers can be short (see next paragraph) which might increase the SNR frac value.

Waveforms	Fraction of injections vetoed by SNR frac cut
ADI A	6.3%
ADI B	1.9%
ADI C	0%
ADI D	3.3%
ADI E	0%

Table 5.5: Percentages of 0.1 Mpc injections removed by the SNR frac cut for each ADI waveform.

is not a plausible distance for detection. This effect will not seriously affect the study. Note that the results are consistent with the preliminary study presented in section 5.4.2.

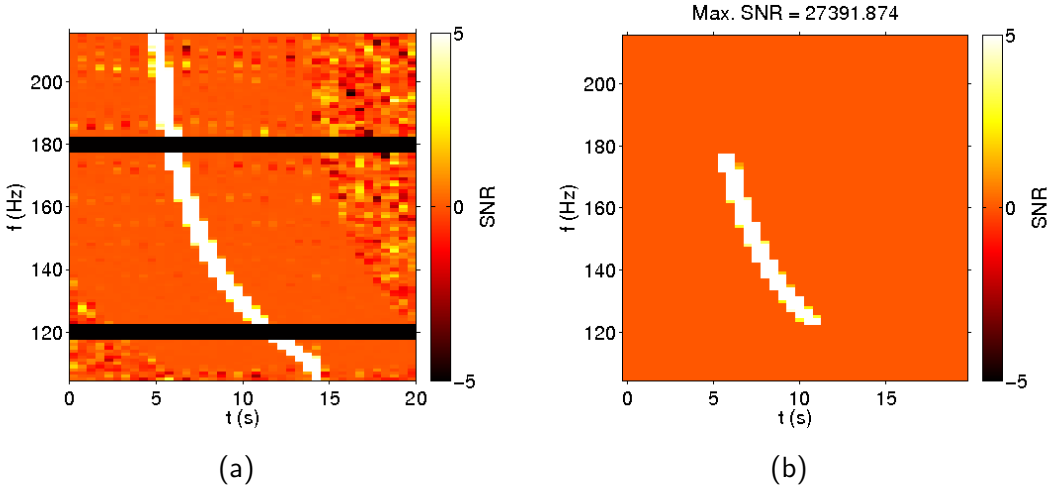

Figure 5.14: Left: STAMP *ft*-map of an ADI B injection at 1 Mpc in gaussian noise. Right: the same map presenting only the pixels belonging to the trigger. Only the central portion of the signal is recovered.

In the case of the ADI B, a loss appears at short distances. This is due to the fact that the ADI B is the shortest of the waveforms, and has the sharpest frequency variation of the models studied: its frequency varies at the rate of 10.53 $\mathrm{Hz\,s^{-1}}$. Furthermore, this waveform spectra passes by the two most important frequency bands notched before the analysis. Indeed, frequencies 118 to 122 Hz

and 178 to 182 Hz are not analyzed because they correspond to 60 Hz harmonics, and the noise around these harmonics in the LIGO experiment is very high. This cut in frequency can prevent the clustering algorithm to work properly: it may indeed cluster the three parts of the signal in the *ft*-map independently. Total recovered SNR may be underestimated, especially with high SNR values. In figure 5.14a is presented an *ft*-map of a strong ADI B signal, and in 5.14b what the clustering algorithm actually returns. We can see that the signal has been split in different parts, and that the clustering algorithm recovers only one of them. In figure 5.15 we present the duration of the recovered ADI B injections with respect to their SNR. The red points represent high amplitude injections. As it can clearly be seen, two distinct populations are visible on this plot, around two main duration values.

To check this explanation, 500 ADI B injections, for the same distances, have been made on MC data, without any frequency notching. No injections loss appeared at low distance, which confirmed the hypothesis.

The ADI D efficiency is affected by another STAMP feature. This waveform possess the smallest frequency evolution rate of the waveforms studied. Given the frequency resolution of the study, a significant amount of power can be present over $\sim 1-2$s at the same frequency. However, the STAMP Y statistic's variance is estimated for each pixel, over the neighboring frequency pixel. In such conditions, the variance is overestimated around these injections, which implies that the SNR is underestimated.

To check this explanation, 500 ADI D injections, for the same distances, have been made on MC data. The SNR calculation has been modified: in formula 4.6, the 5 first neighboring pixels were not used for the SNR variance calculation, to avoid any contamination of the signal. The efficiency curve obtained have a normal aspect, which confirmed the hypothesis. This effect strongly affects the detection capabilities of STAMPAS for this waveform. In chapter 7, we will detail methods currently investigated to solve this problem.

For the EBBH study, the efficiency curves are done using a different SNR threshold, corresponding to the SNR of the loudest background event which

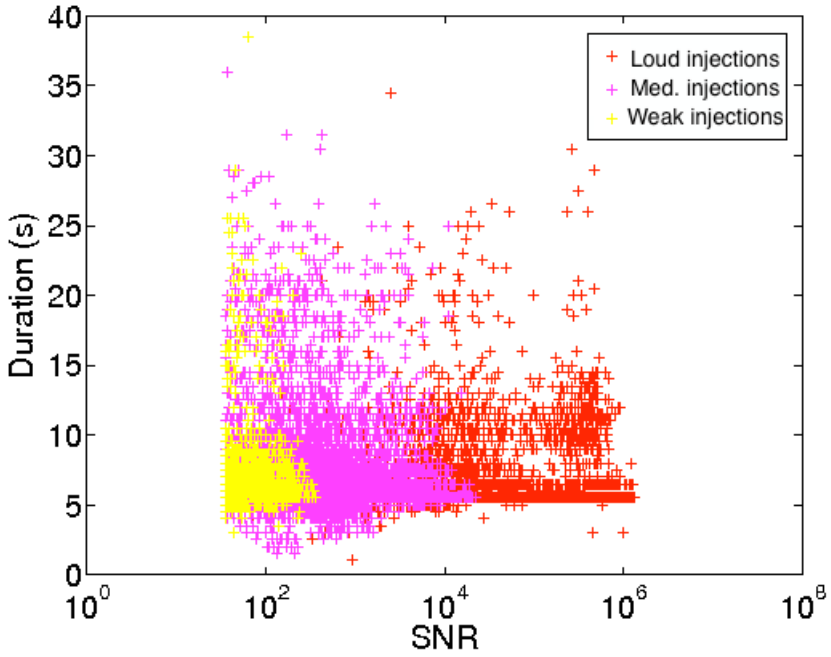

Figure 5.15: Duration of the triggers corresponding to recovered ADI B injections, with respect to their SNR. Red points correspond to injections from 0.1 to 1 Mpc, magenta points to injections from 2 to 10 Mpc, and yellow points to injections from 15 Mpc to 60 Mpc. A significant number of loud injections have a duration of about 6 seconds, despite the fact that the duration of the injection is 9.4s.

passed the selection cuts of this study. The loudest background event of the EBBH study is the event number 7 in the result table of the S5 analysis (see appendix A), and has an SNR of 267.07, Results are given in figure 5.16a.

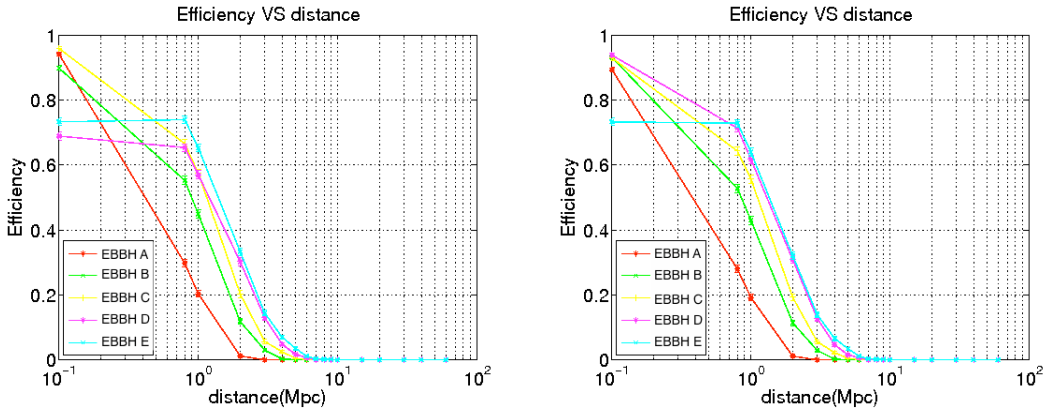

(a) The efficiency curves obtained for the five EBBH waveforms, with the SNRfrac cut and the DQs applied.

(b) The efficiency curves obtained for the five EBBH waveforms, with only the DQs applied.

Figure 5.16: Efficiency curves for the EBBH study, with a SNR threshold of 267.07. The application of a SNR frac cut with a 0.99 threshold doesn't significantly change the overall efficiency curves. The only significant loss happens at very low distances.

5.4.6 The False Alarm Density statistics

Before we analyze the non-timeshifted data, the so-called zero lag, it is important to know on which criteria we decide that a trigger is a gravitational wave candidate. A simple idea would be to choose a low false alarm rate, use the background study to find the associated SNR threshold, and declare as a candidate any trigger which SNR is superior to that threshold candidate. This method has been used in published short transient searches [90]. It has the inconvenience of making us choose an arbitrary FAR. If we pick a FAR too high, the candidate selection will be conservative but we take the risk of discarding genuine signals. A FAR too low would force us to investigate many background triggers.

To avoid these issues, we decided to use a ranking statistic of the events which takes into account the efficiency of the search with respect to the signal we are looking at and the background events, and which doesn't assume any arbitrary threshold. The False Alarm Density (FAD) statistics, as presented in [91], meets this requirement.

The visible volume

This statistic is based on an essential quantity: the *visible volume*,

$$V_{vis}(W, \mathrm{SNR}_t) = 4\pi \int_0^{+\infty} \varepsilon(W, r, \mathrm{SNR}_t) r^2 dr \tag{5.3}$$

where W symbolizes a waveform, ε its detection efficiency, function of the SNR threshold SNR_t and of r the distance to the simulated source. The visible volume is a figure of merit which indicates the effective volume investigated by the pipeline. The bigger this volume, the more likely we are to detect the waveform W in the data. This volume can be calculated for each possible value of SNR_t. Efficiencies are calculated as described in 4.2.5.

Of course the efficiency can't be estimated over all possible distances. With a limited sample of distances, it is possible to estimate the visible volume as

$$V_{vis}(W, \mathrm{SNR}_t) = \sum_{i=1}^{N_{tot}} 4\pi r_i^2 \left(\frac{dN_{inj}}{dr}(r_i) \right)^{-1} = \sum_{i=1}^{N_{tot}} \frac{1}{\rho_i} \tag{5.4}$$

with N_{tot} the total number of injections made, r_i the distance of the ith injection, and $\frac{dN_{inj}}{dr}(r_i)$ the radial density of simulated events. The uncertainty on this calculation is

$$\delta V_{vis} = \sqrt{\sum_{i=1}^{N_{tot}} \frac{1}{\rho_i^2}} \tag{5.5}$$

The FAD

To calculate the FAD associated to a given SNR_t value, one has to sum over all the triggers possessing a SNR superior to SNR_t, the inverse of the visible volume associated to their SNR. Then, this sum is normalized by the total lifetime T_{bkg} of the background,

$$\mathrm{FAD}_W(\mathrm{SNR}_t) = \frac{1}{T_{bkg}} \left(\sum_{\mathrm{SNR}_i > \mathrm{SNR}_t} \frac{1}{V_{vis}(W, \mathrm{SNR}_i)} \right) \tag{5.6}$$

The FAD, expressed in $[Distance]^{-3} \cdot [Time]^{-1}$, estimates the number of background events expected in a given observed volume, per unit of time. Whereas the FAR takes only into account background event rates, the FAD is weighted over the sensitivity to the sources studied. Equation (5.6) is based on only one waveform, but it is possible to take into account more waveforms by averaging the visible volume over all the studied waveforms,

$$\mathrm{FAD}(\mathrm{SNR}_t) = \frac{1}{T_{bkg}} \left(\sum_{\mathrm{SNR}_i > \mathrm{SNR}_t} \frac{1}{\bar{V}_{vis}(\mathrm{SNR}_i)} \right) \tag{5.7}$$

with $\bar{V}_{vis}$ the visible volume averaged over all W waveforms. Let us note here that it is possible to use this statistic to combine results from different pairs of detectors, even if, in the present case, we don't need to as we only use one pair.

Rank the candidates

The FAD can be used to rank the triggers from the background and from the zero-lag. Each SNR can be associated to a FAR. The more an event is significant, the smaller is its associated FAD. To determine the significance of the event, we can calculate its False Alarm Probability (FAP) *i.e.* the probability that an event is not caused by a gravitational wave. The FAP of a zero lag event is

$$\mathrm{FAP}(N) = 1 - \sum_{n=0}^{N-1} \frac{\mu^n}{n!} e^{-\mu} \tag{5.8}$$

where N is the total number of events present in the zero lag which FAD value is lower than the FAD of the considered event, and

$$\mu = \text{FAD} \cdot \nu(\text{FAD}) = \text{FAD} \cdot (T_{zero\ lag} V_{vis}(\text{FAD})) \tag{5.9}$$

ν is the *overall search productivity*, which is the product of the observable time by the visible volume associated to the event.

In absence of detection

If no foreground events end up to be genuine signals, it is possible, using the *loudest event statistic* [92] to use the overall search productivity of the loudest event to set an upper limit on the rate of the studied source. If we assume that the event SNR distribution we are interested in is Poissonian, of intrinsic rate R, it is possible to estimate the probability that, if we detect an event E, it has a SNR smaller than SNR_t. We can write this probability as

$$P(\text{SNR}|RT_{obs}) = e^{-RT_{obs}\varepsilon(\text{SNR})} \tag{5.10}$$

with T_{obs} the observation time and ε the search efficiency. If we consider the loudest event we have in the data, with $\text{SNR} = \text{SNR}_{max}$ – even if it's not a gravitational wave issued trigger – we can calculate the 90% upper limit rate $R_{90\%}$ *i.e.* the event rate such as the probability that we have a $100 - 90 = 10\%$ probability to detect a signal weaker than the loudest event,

$$0.1 = e^{-R_{90\%}T_{obs}\varepsilon(\text{SNR}_{max})} \tag{5.11}$$

which yields

$$R_{90\%} = -\frac{\ln(1-0.9)}{T_{obs}\varepsilon(\text{SNR}_{max})} \tag{5.12}$$

In other words, we are 90% confident that if the event rate was higher than $R_{90\%}$, we would have detected a candidate of $\text{SNR} < \text{SNR}_{max}$. Another way to interpret

this result is to say that we have 10% probability to have underestimated the true event rate with the measures.

Using the FAD notation, one can calculate an upper limit on the event rate per unit volume with

$$R_{90\%} = \frac{2.303}{\nu(\mathrm{FAD}^{\star})} \tag{5.13}$$

where $\mathrm{FAD}^{\star}$ is the FAD associated with the highest ranked trigger in the zero lag. This rate will be estimated using FAD calculated only with the appropriate waveform/set of waveforms.

Chapter 6

Zero lag results

"My momma always said, "Life was like a box of chocolates. You never know what you're gonna get.""

Forrest Gump

After the S5 background study, the zero lag triggers – triggers issued from the data correlation of H1 and L1 without any time shift introduced – have been produced. Before studying them, we apply on them the cuts determined during the background study. Once this is done, results are revealed – "we open the box". In this chapter we detail and comment the results obtained respectively for ADI and EBBH signals.

6.1 ADI analysis

6.1.1 Event distribution

Displayed in figure 6.1a is the false alarm rate distribution of background events and foreground events (events from the zero lag). Figure 6.1b presents a zoomed-in version of figure 6.1a. It can be seen that no event has a SNR superior to the loudest background event. The FAR distribution of the foreground is compatible with the background distribution, as well as with the MC background distribution.

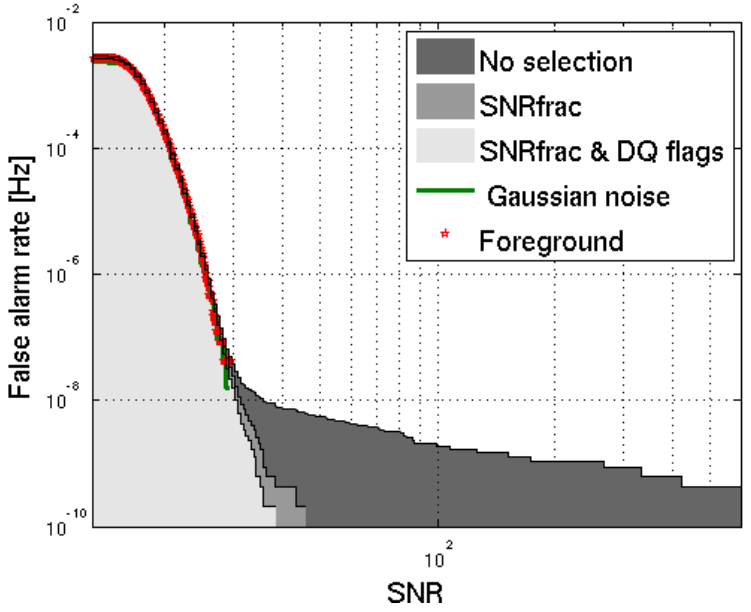

(a)

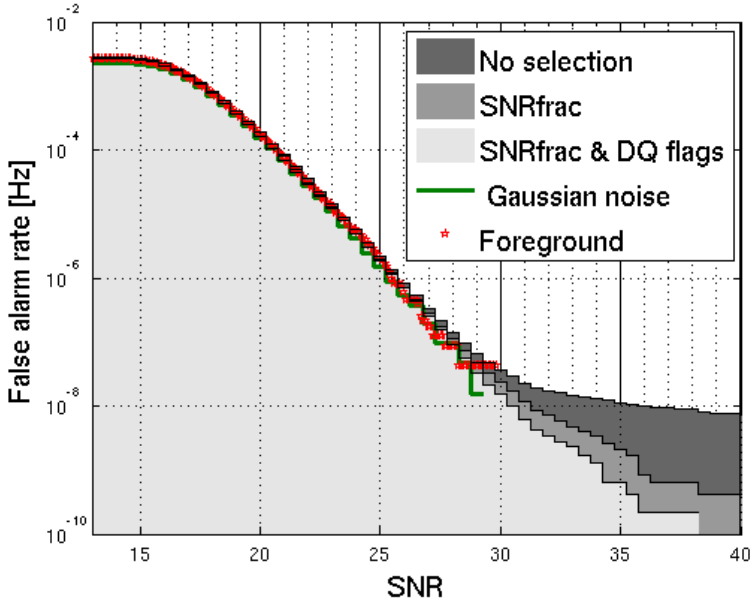

(b)

Figure 6.1: The FAR distribution for the background triggers (issued from time shifted data), the foreground triggers (issued from non shifted data), and Monte-Carlo simulated data, using cuts adapted to ADI waveforms, regular (a) and zoomed-in (b) version. The "no selection" curves correspond to all the background triggers without any selection. The "SNRfrac" curves correspond to the background triggers which passed the SNRfrac cut. The "SNRfrac & DQ Flags" curves correspond to the background triggers which passed both SNRfrac cut and DQs vetoes. The "Gaussian Noise" curves correspond to the simulated data, and the "Foreground" curves to the foreground events which passed all the cuts.

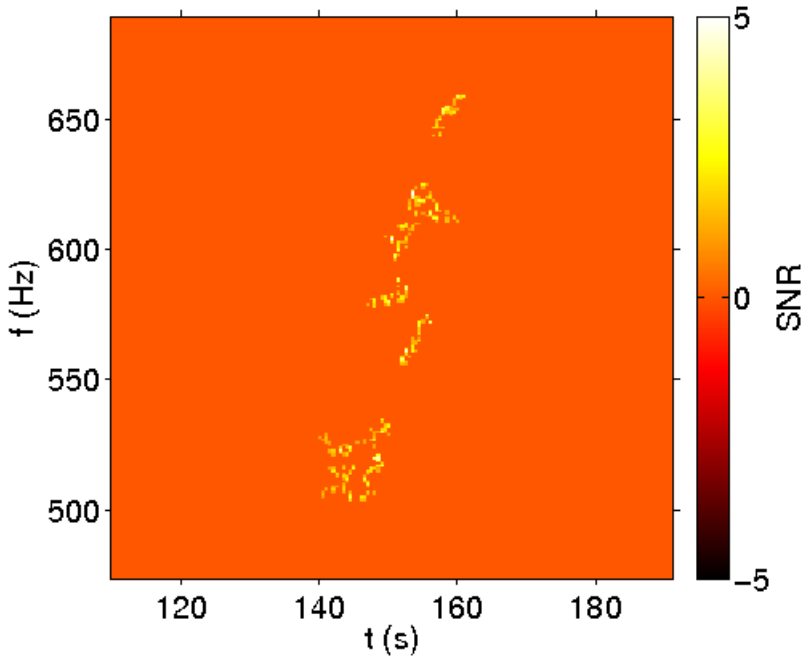

Figure 6.2: The *ft*-map of the loudest foreground event. Only the pixels belonging to the event are displayed.

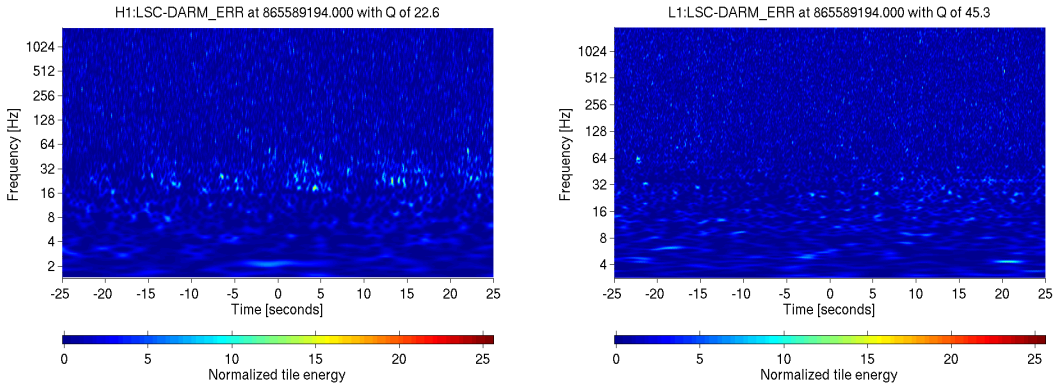

(a) (b)

Figure 6.3: The OMEGA scans in H1 (a) and L1 (a) centered on the start time of the loudest foreground event. At the frequency of the event, no excess power can be seen.

Displayed in figure 6.4 are the main characteristics of the foreground events. There are no outlier event, and all the plots are fairly similar to the background figures 5.11.

In figure 6.2 we present the STAMP *ft*-map associated with the loudest event, along in figures 6.3a and 6.3b as the OMEGA scans of H1 and L1 at the time of the trigger. No significant power excess can be observed in any interferometer, and the structure of the STAMPAS trigger is comparable with triggers obtained by random fluctuations. The square-root SNR of the loudest foreground events, compared to amplitude SNRs of different burst studies [93], are consistent with noise events. We therefore cannot claim any signal detection.

In table 6.1 we present the characteristics of the 10 loudest foreground events. Most of them have a frequency range well over 200Hz, with no obvious cause. They except for one event they all last between 20s and 35s, which is compatible with the predicted background behavior (see figure 5.11c).

Id	SNR	$SNR^{1/2}$	GPS time	Dur. (s)	f_{min} (Hz)	f_{max} (Hz)	SNR_{frac}
1	29.78	5.46	865589194.0	21.0	504	659	0.06
2	28.19	5.31	851136555.0	22.0	130	201	0.10
3	27.60	5.25	837932716.5	27.0	919	985	0.10
4	27.09	5.20	861745784.0	21.0	379	454	0.11
5	26.91	5.19	869880309.5	32.5	716	807	0.08
6	26.69	5.17	855253512.5	22.5	720	826	0.09
7	26.62	5.16	867409131.0	29.0	443	552	0.11
8	26.62	5.16	839114728.0	46.5	517	570	0.11
9	26.57	5.15	822357086.0	20.5	901	954	0.08
10	26.48	5.15	839761476.0	37.5	736	809	0.06

Table 6.1: Table of the 10 loudest foreground events characteristics.

6.1.2 Vetoed events

Of the 67941 triggers of the zero lag, 63330 passed the cuts (93.21 % of the total). 2 of them have been vetoed by SNRfrac, the rest were removed due to the data quality flags. 6.79 % of the triggers have been flagged by the data quality flags,

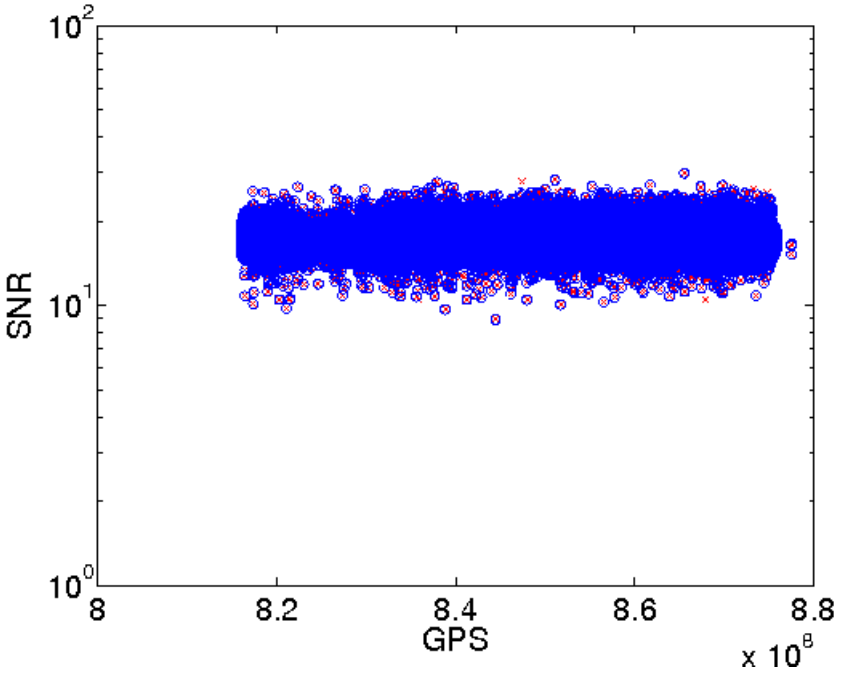

(a) SNR vs. GPS time plot of the triggers.

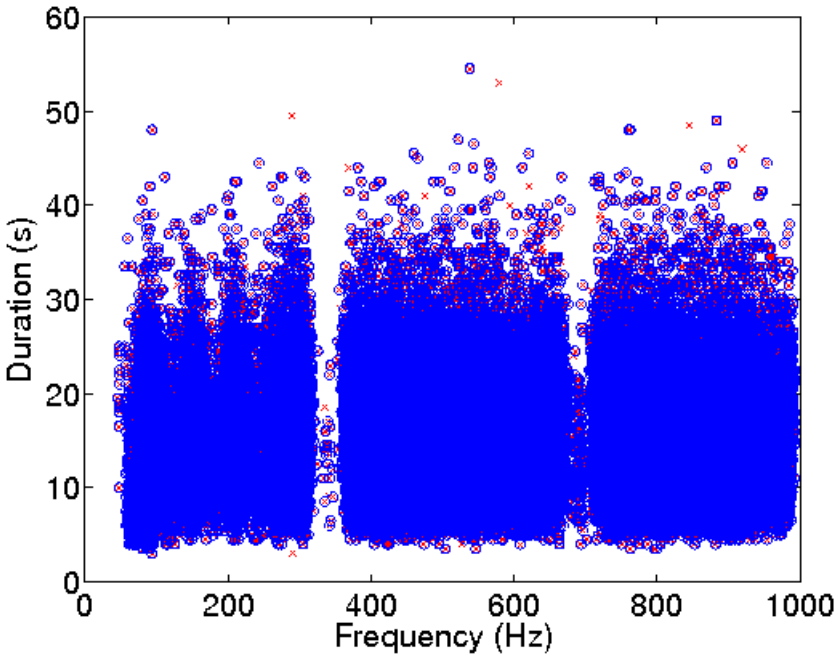

(b) Duration vs. Frequency plot of the triggers

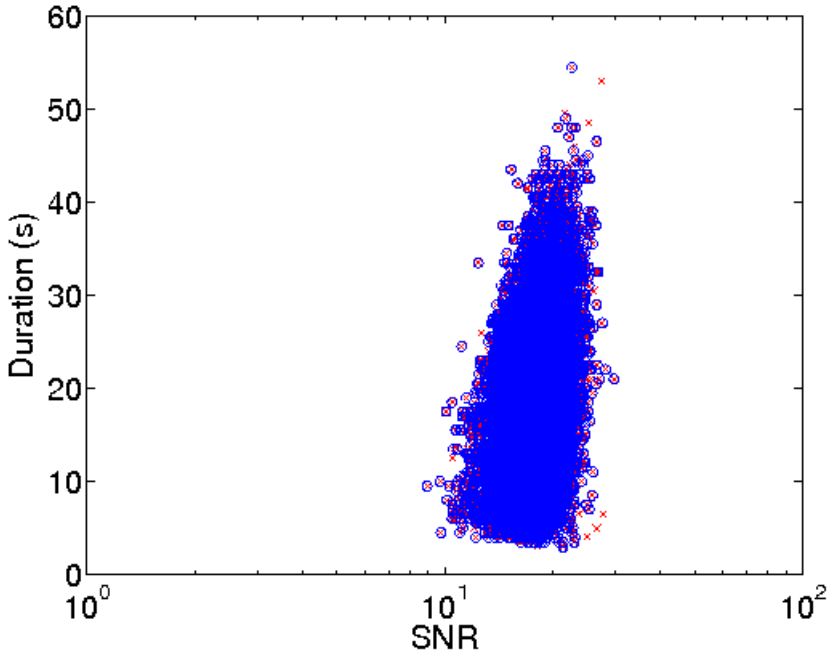

(c) Duration vs. SNR plot of the triggers

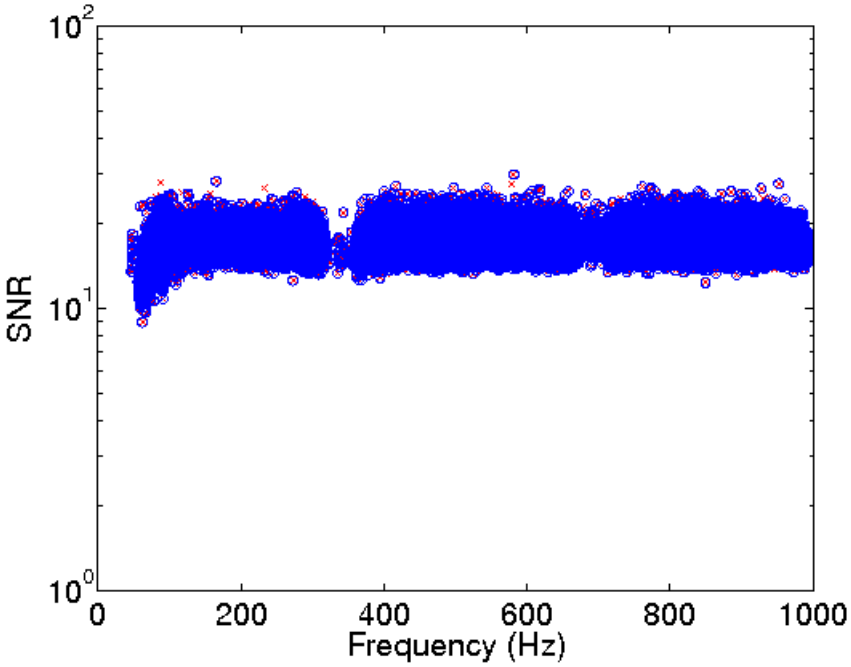

(d) Frequency vs. SNR plot of the triggers

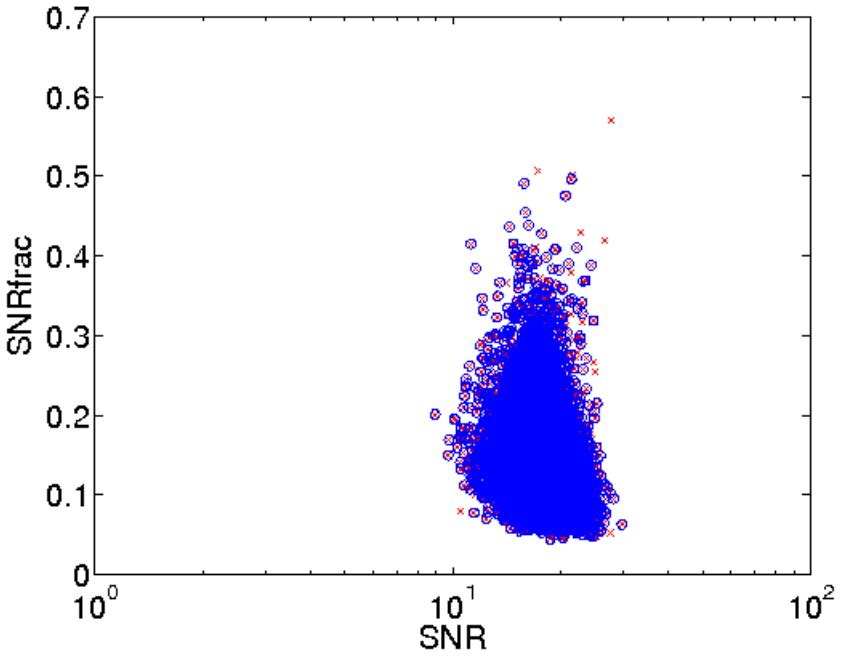

(e) SNR frac vs. SNR plot of the triggers

Figure 6.4: Various views of the parameter space covered by the foreground triggers. The red points represents the entire set of triggers and the blue ones the triggers not vetoed by any DQ and with an SNRfrac value less than 0.5.

which is compatible with the dead time of the vetoes. Indeed the total dead-time of H1 vetoes was 2.98 % and the total dead-time of L1 vetoes 3.34 %. This confirms the good quality of the foreground data.

In figure 6.5 are displayed frequency and duration histograms of the foreground triggers. As it can be seen, no specific trigger population was removed by the cuts.

6.1.3 Astrophysical statements

Using the statistics described in section 5.4.6 it is possible to calculate the False Alarm Density (FAD) and the False Alarm Probability (FAP) of the loudest events, based on each of the five ADI waveforms used for the analysis. They are summarized in table 6.2. The statistical uncertainty on the FAD has been estimated using formula (5.5), and propagating the error on the visible volume. Systematic uncertainty comes mainly from the detectors calibration uncertainties, estimated in [94]. An error of calibration can be considered as an error on the injections' amplitude *i.e.* as an error on the distance to the sources. An $X\%$ error on the distance implies a $3X\%$ error on the visible volume. In the 40-2000 Hz frequency band, amplitude calibration error for H1 is 10.4 %, and 14.4 % in L1. The uncertainty quadratic sum is therefore 17.8 %. Hence, the error on the visible volume is approximately 54 %.

A similar table can be made for false alarm probability values, see table 6.3. Errors on the FAD and visible volume calculation have been propagated to the calculation of the FAP, and the obtained values have been maximized consequently. Estimates in table 6.3 are therefore conservative estimates.

As we can see in table 6.3, the FAP is similar for each of the studied waveforms, and strongly supports the non-gravitational wave origin of the foreground.

With the false alarm density profiles calculated using the S5 background, for each of the five ADI waveforms, and the false alarm density of the loudest event, we can set an upper limit on the rate of ADI events for each of the five models, using equation (5.13). Results are given in table 6.4, and have been readjusted upwards taking into account the calculation uncertainties.

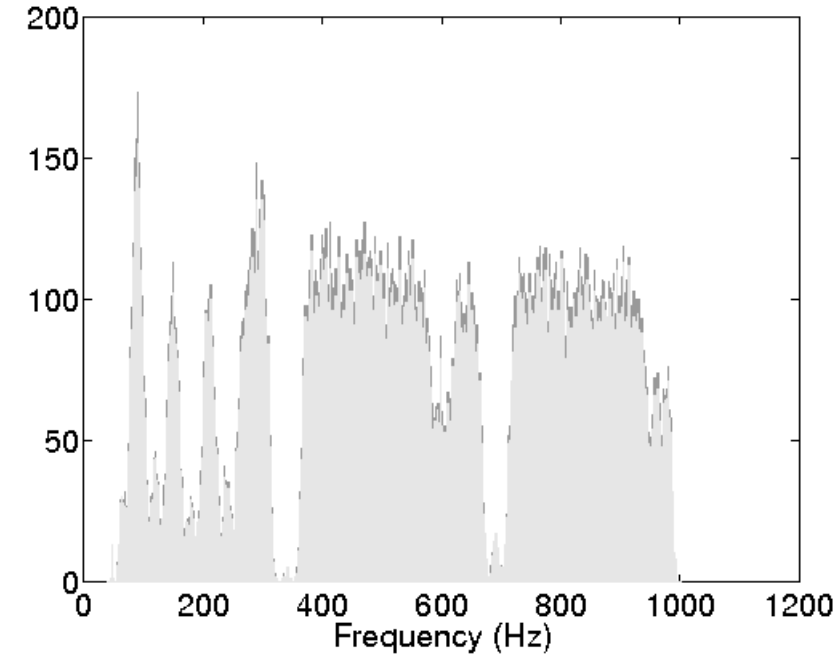

(a)

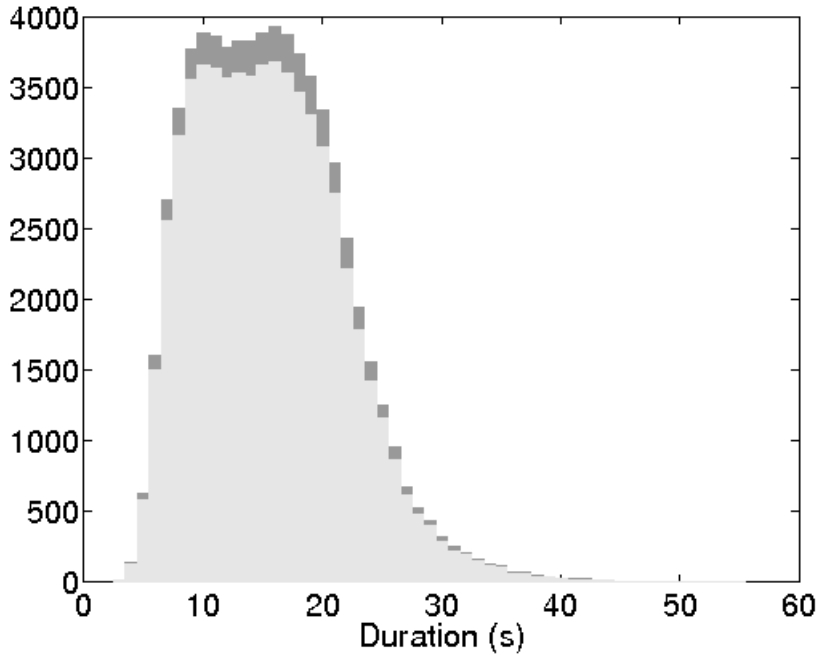

(b)

Figure 6.5: Frequency (a) and duration (b) histograms of the foreground triggers. In dark grey are displayed all the triggers obtained, and in light grey the triggers which passed the cuts.

ID	SNR	ADI A ($\mathrm{Mpc^{-3}yr^{-1}}$)	ADI B ($\mathrm{Mpc^{-3}yr^{-1}}$)	ADI C ($\mathrm{Mpc^{-3}yr^{-1}}$)	ADI D ($\mathrm{Mpc^{-3}yr^{-1}}$)	ADI E ($\mathrm{Mpc^{-3}yr^{-1}}$)
1	29.78	$4.09 \cdot 10^{-4}$ $\pm 2.21 \cdot 10^{-4}$	$1.30 \cdot 10^{-5}$ $\pm 7.01 \cdot 10^{-6}$	$1.04 \cdot 10^{-4}$ $\pm 5.61 \cdot 10^{-5}$	$3.60 \cdot 10^{-3}$ $\pm 1.96 \cdot 10^{-3}$	$4.97 \cdot 10^{-5}$ $\pm 2.68 \cdot 10^{-5}$
2	28.19	$1.52 \cdot 10^{-3}$ $\pm 8.20 \cdot 10^{-4}$	$5.09 \cdot 10^{-5}$ $\pm 2.75 \cdot 10^{-5}$	$4.01 \cdot 10^{-4}$ $\pm 2.16 \cdot 10^{-4}$	$1.31 \cdot 10^{-2}$ $\pm 7.13 \cdot 10^{-3}$	$1.92 \cdot 10^{-4}$ $\pm 1.03 \cdot 10^{-4}$
3	27.60	$2.64 \cdot 10^{-3}$ $\pm 1.43 \cdot 10^{-3}$	$9.04 \cdot 10^{-5}$ $\pm 4.88 \cdot 10^{-5}$	$7.07 \cdot 10^{-4}$ $\pm 3.82 \cdot 10^{-4}$	$2.28 \cdot 10^{-2}$ $\pm 1.24 \cdot 10^{-2}$	$3.38 \cdot 10^{-4}$ $\pm 1.82 \cdot 10^{-4}$
4	27.09	$4.23 \cdot 10^{-3}$ $\pm 2.29 \cdot 10^{-3}$	$1.46 \cdot 10^{-4}$ $\pm 7.90 \cdot 10^{-5}$	$1.13 \cdot 10^{-3}$ $\pm 6.13 \cdot 10^{-4}$	$3.63 \cdot 10^{-2}$ $\pm 1.98 \cdot 10^{-2}$	$5.36 \cdot 10^{-4}$ $\pm 2.90 \cdot 10^{-4}$
5	26.91	$5.10 \cdot 10^{-3}$ $\pm 2.76 \cdot 10^{-3}$	$1.77 \cdot 10^{-4}$ $\pm 9.54 \cdot 10^{-5}$	$1.37 \cdot 10^{-3}$ $\pm 7.39 \cdot 10^{-4}$	$4.37 \cdot 10^{-2}$ $\pm 2.38 \cdot 10^{-2}$	$6.44 \cdot 10^{-4}$ $\pm 3.48 \cdot 10^{-4}$
6	26.69	$6.15 \cdot 10^{-3}$ $\pm 3.32 \cdot 10^{-3}$	$2.13 \cdot 10^{-4}$ $\pm 1.15 \cdot 10^{-4}$	$1.65 \cdot 10^{-3}$ $\pm 8.89 \cdot 10^{-4}$	$5.25 \cdot 10^{-2}$ $\pm 2.86 \cdot 10^{-2}$	$7.74 \cdot 10^{-4}$ $\pm 4.18 \cdot 10^{-4}$
7	26.62	$6.56 \cdot 10^{-3}$ $\pm 3.54 \cdot 10^{-3}$	$2.28 \cdot 10^{-4}$ $\pm 1.23 \cdot 10^{-4}$	$1.75 \cdot 10^{-3}$ $\pm 9.48 \cdot 10^{-4}$	$5.59 \cdot 10^{-2}$ $\pm 3.05 \cdot 10^{-2}$	$8.24 \cdot 10^{-4}$ $\pm 4.45 \cdot 10^{-4}$
8	26.62	$6.57 \cdot 10^{-3}$ $\pm 3.55 \cdot 10^{-3}$	$2.28 \cdot 10^{-4}$ $\pm 1.23 \cdot 10^{-4}$	$1.76 \cdot 10^{-3}$ $\pm 9.49 \cdot 10^{-4}$	$5.60 \cdot 10^{-2}$ $\pm 3.05 \cdot 10^{-2}$	$8.25 \cdot 10^{-4}$ $\pm 4.46 \cdot 10^{-4}$
9	26.57	$6.88 \cdot 10^{-3}$ $\pm 3.72 \cdot 10^{-3}$	$2.39 \cdot 10^{-4}$ $\pm 1.29 \cdot 10^{-4}$	$1.84 \cdot 10^{-3}$ $\pm 9.94 \cdot 10^{-4}$	$5.87 \cdot 10^{-2}$ $\pm 3.20 \cdot 10^{-2}$	$8.64 \cdot 10^{-4}$ $\pm 4.67 \cdot 10^{-4}$
10	26.48	$7.56 \cdot 10^{-3}$ $\pm 4.09 \cdot 10^{-3}$	$2.63 \cdot 10^{-4}$ $\pm 1.42 \cdot 10^{-4}$	$2.02 \cdot 10^{-3}$ $\pm 1.09 \cdot 10^{-3}$	$6.44 \cdot 10^{-2}$ $\pm 3.51 \cdot 10^{-2}$	$9.49 \cdot 10^{-4}$ $\pm 5.12 \cdot 10^{-4}$

Table 6.2: Table of the FAD values of the loudest foreground events, based on each of the 5 ADI waveforms studied.

ID	SNR	ADI A (%)	ADI B (%)	ADI C (%)	ADI D (%)	ADI E (%)
1	29.78	60	59	59	61	58
2	28.19	~ 100	97	98	~ 100	98

Table 6.3: Table of the FAP values of the loudest foreground events, based on each of the 5 ADI waveforms studied. The next events have a FAP compatible with 100 %.

These upper limits are the first ones set on ADI signals with an all-sky search[1], and are a milestone of long transient gravitational waves search. The best results are achieved for the ADI B waveform, which is the loudest signal we have been testing. Upper limits are decreasing as the amplitude of the waveforms tested increases (see table 5.2). We noticed however that the frequency behavior of the waveforms can have a significant impact on the search efficiency (see section 5.4.5). It is however difficult to disentangle the relative contribution of the waveforms' amplitude and of their frequency evolution, to the value of the upper limits with the ADI waveforms we used for the analysis.

ADI A ($\mathrm{Mpc^{-3}yr^{-1}}$)	ADI B ($\mathrm{Mpc^{-3}yr^{-1}}$)	ADI C ($\mathrm{Mpc^{-3}yr^{-1}}$)	ADI D ($\mathrm{Mpc^{-3}yr^{-1}}$)	ADI E ($\mathrm{Mpc^{-3}yr^{-1}}$)
$4.31 \cdot 10^{-3}$	$1.43 \cdot 10^{-4}$	$1.13 \cdot 10^{-3}$	$3.77 \cdot 10^{-2}$	$5.48 \cdot 10^{-4}$

Table 6.4: Table of the rate upper limits for the 5 ADI waveforms studied.

In [60], the ADI rate is estimated to be $\sim 10^{-6}$ $\mathrm{Mpc^{-3}yr^{-1}}$. This rate is estimated assuming that it is comparable to the rate of long gamma-ray bursts emitted by supernovæ. Indeed, ADIs are also a source of long gamma-ray bursts [60, 61]. However not all long gamma-ray bursts issued from supernovæare associated with ADIs, this rate is therefore optimistic. The best upper limit we set is one order of magnitude above this value. With the next generation of ground-based interferometers, Advanced LIGO and Advanced Virgo, the sensitivity of the detectors should be higher by a factor 10 [98]. This would increase the visible volumes by a factor 10^3, and lower the upper limits by the same factor. We should therefore be able to set upper limits equivalent to or lower than the predicted rates. This means that the detection of ADI signals during advanced detector era is a possibility. In case of no detection, the new upper limits should set strong constraints on the astrophysical models.

[1]For the results of the previous (short) transient all-sky searches, see [95, 96, 97].

6.2 EBBH analysis

In section 5.4.2 we decided to split the analysis in two: one analysis using cuts adapted to ADI signals, and one analysis using cuts adopted to EBBH signals. In this section we present results from this second analysis.

6.2.1 Event distribution

Displayed in figure 6.6a is the FAR distribution of the background and of the foreground events using the adapted SNRfrac cut of 0.99. The loudest foreground event is unchanged (see figures 6.2, 6.3a and 6.3b), and only one event changes in the 10 loudest with respect to the ADI study. We cannot claim any signal detection.

In table 6.5 we present the characteristics of the 10 loudest foreground events obtained using EBBH cuts. Except for event 3 they are identical to the events presented in 6.1.

Id	SNR	$SNR^{1/2}$	GPS time	Dur. (s)	f_{min} (Hz)	f_{max} (Hz)	SNR_{frac}
1	29.78	5.46	865589194.0	21.0	504	659	0.06
2	28.19	5.31	851136555.0	22.0	130	201	0.10
3	27.79	5.27	847415551.0	6.5	67	109	0.57
4	27.60	5.25	837932716.5	27.0	919	985	0.10
5	27.09	5.20	861745784.0	21.0	379	454	0.11
6	26.91	5.19	869880309.5	32.5	716	807	0.08
7	26.69	5.17	855253512.5	22.5	720	826	0.09
8	26.62	5.16	867409131.0	29.0	443	552	0.11
9	26.62	5.16	839114728.0	46.5	517	570	0.11
10	26.57	5.15	822357086.0	20.5	901	954	0.08

Table 6.5: Table of the 10 loudest foreground events characteristics, with cuts adapted to EBBH signals.

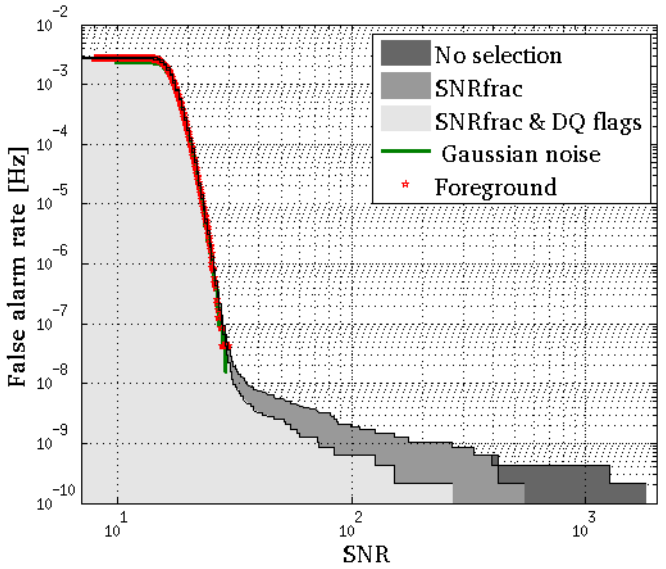

(a)

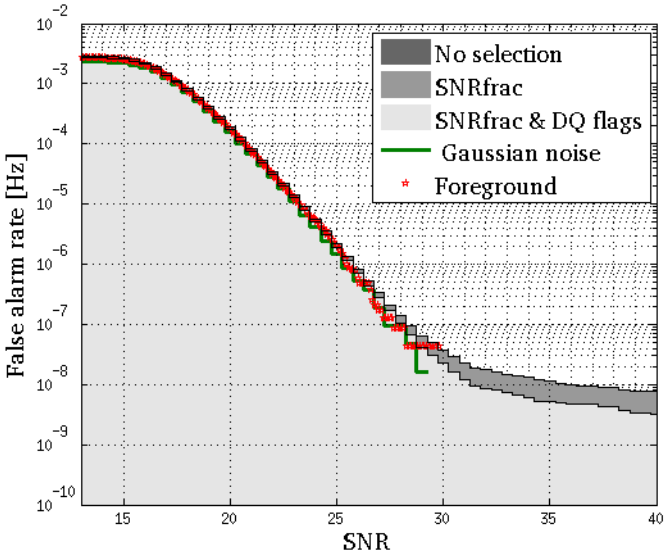

(b)

Figure 6.6: The FAR distribution for the background triggers (issued from time shifted data), the foreground triggers (issued from non shifted data), and Monte-Carlo simulated data, using cuts adapted to EBBH waveforms, regular (a) and zoomed-in (b) version. The "no selection" curves correspond to all the background triggers without any selection. The "SNRfrac" curves correspond to the background triggers which passed the SNRfrac cut. The "SNRfrac & DQ Flags" curves correspond to the background triggers which passed both SNRfrac cut and DQs vetoes. The "Gaussian Noise" curves correspond to the simulated data, and the "Foreground" curves to the foreground events which passed all the cuts.

6.2.2 Vetoed events

The discussion on vetoed events is the same than in section 6.1.2. Indeed only two events were vetoed by the SNRfrac cut in the ADI study, which does not change in any significant way the results presented there.

6.2.3 Astrophysical statements

The false alarm density and the false alarm probability of the loudest events based on each of the five EBBH waveforms used for the analysis, are summarized in table 6.6. The statistical uncertainty on the FAD has been estimated using formula (5.5), and propagating the error on the visible volume. Systematical uncertainty come mainly from the detectors calibration uncertainties, estimated in [94]. The consequent error on the visible volume is approximately 54 %.

The FAD values obtained with EBBH signals are 1 or 2 orders of magnitude higher than the values obtained with ADI signals. This can be due to the background selection, which is less efficiency in the case of EBBH signals than in the case of EBBH signals.

As we can see in table 6.7, FAP are also very elevated, leaving few doubts on the non-gravitational wave nature of the loudest events. As we done previously, errors on the FAD and visible volume calculation have been propagated to the calculation of the FAP, and the obtained values have been maximized consequently.

With the false alarm density profiles calculated using the S5 background, for each of the five EBBH waveforms, and the false alarm density of the loudest event, we can set upper limits on the rate of EBBH events, using equation (5.13). Results are given in table 6.8, and have been readjusted upward taking into account the calculation uncertainties.

Recent studies estimate the rate of binary black holes close encounters to $\sim 10^{-11} - 10^{-6}$ $\mathrm{Mpc}^{-3}\mathrm{yr}^{-1}$ [66, 68]. In the advanced detector era, the upper limits should be close to the upper value presented here. In the current state of

ID	SNR	EBBH A ($\mathrm{Mpc^{-3}yr^{-1}}$)	EBBH B ($\mathrm{Mpc^{-3}yr^{-1}}$)	EBBH C ($\mathrm{Mpc^{-3}yr^{-1}}$)	EBBH D ($\mathrm{Mpc^{-3}yr^{-1}}$)	EBBH E ($\mathrm{Mpc^{-3}yr^{-1}}$)
1	29.78	$1.25 \cdot 10^{-2}$ $\pm 7.78 \cdot 10^{-3}$	$3.19 \cdot 10^{-3}$ $\pm 1.77 \cdot 10^{-3}$	$1.90 \cdot 10^{-3}$ $\pm 1.04 \cdot 10^{-3}$	$1.11 \cdot 10^{-3}$ $\pm 6.02 \cdot 10^{-4}$	$1.19 \cdot 10^{-3}$ $\pm 6.48 \cdot 10^{-4}$
2	28.19	$2.22 \cdot 10^{-2}$ $\pm 1.30 \cdot 10^{-2}$	$6.43 \cdot 10^{-3}$ $\pm 3.53 \cdot 10^{-3}$	$4.06 \cdot 10^{-3}$ $\pm 2.21 \cdot 10^{-3}$	$2.44 \cdot 10^{-3}$ $\pm 1.32 \cdot 10^{-3}$	$3.13 \cdot 10^{-3}$ $\pm 1.70 \cdot 10^{-3}$
3	27.79	$2.80 \cdot 10^{-2}$ $\pm 1.62 \cdot 10^{-2}$	$8.39 \cdot 10^{-3}$ $\pm 4.59 \cdot 10^{-3}$	$5.37 \cdot 10^{-3}$ $\pm 2.92 \cdot 10^{-3}$	$3.24 \cdot 10^{-3}$ $\pm 1.76 \cdot 10^{-3}$	$4.33 \cdot 10^{-3}$ $\pm 2.34 \cdot 10^{-3}$
4	27.60	$3.19 \cdot 10^{-2}$ $\pm 1.83 \cdot 10^{-2}$	$9.73 \cdot 10^{-3}$ $\pm 5.32 \cdot 10^{-3}$	$6.27 \cdot 10^{-3}$ $\pm 3.40 \cdot 10^{-3}$	$3.79 \cdot 10^{-3}$ $\pm 2.05 \cdot 10^{-3}$	$5.13 \cdot 10^{-3}$ $\pm 2.78 \cdot 10^{-3}$
5	27.09	$4.54 \cdot 10^{-2}$ $\pm 2.57 \cdot 10^{-2}$	$1.44 \cdot 10^{-2}$ $\pm 7.83 \cdot 10^{-3}$	$9.43 \cdot 10^{-3}$ $\pm 5.12 \cdot 10^{-3}$	$5.70 \cdot 10^{-3}$ $\pm 3.09 \cdot 10^{-3}$	$7.94 \cdot 10^{-3}$ $\pm 4.30 \cdot 10^{-3}$
6	26.91	$5.26 \cdot 10^{-2}$ $\pm 2.96 \cdot 10^{-2}$	$1.69 \cdot 10^{-2}$ $\pm 9.19 \cdot 10^{-3}$	$1.11 \cdot 10^{-2}$ $\pm 6.04 \cdot 10^{-3}$	$6.73 \cdot 10^{-3}$ $\pm 3.64 \cdot 10^{-3}$	$9.46 \cdot 10^{-3}$ $\pm 5.12 \cdot 10^{-3}$
7	26.69	$6.15 \cdot 10^{-2}$ $\pm 3.44 \cdot 10^{-2}$	$1.99 \cdot 10^{-2}$ $\pm 1.08 \cdot 10^{-2}$	$1.32 \cdot 10^{-2}$ $\pm 7.16 \cdot 10^{-3}$	$7.97 \cdot 10^{-3}$ $\pm 4.31 \cdot 10^{-3}$	$1.13 \cdot 10^{-2}$ $\pm 6.11 \cdot 10^{-3}$
8	26.62	$6.48 \cdot 10^{-2}$ $\pm 3.63 \cdot 10^{-2}$	$2.11 \cdot 10^{-2}$ $\pm 1.15 \cdot 10^{-2}$	$1.40 \cdot 10^{-2}$ $\pm 7.59 \cdot 10^{-3}$	$8.44 \cdot 10^{-3}$ $\pm 4.57 \cdot 10^{-3}$	$1.20 \cdot 10^{-2}$ $\pm 6.50 \cdot 10^{-3}$
9	26.62	$6.49 \cdot 10^{-2}$ $\pm 3.63 \cdot 10^{-2}$	$2.11 \cdot 10^{-2}$ $\pm 1.15 \cdot 10^{-2}$	$1.40 \cdot 10^{-2}$ $\pm 7.60 \cdot 10^{-3}$	$8.46 \cdot 10^{-3}$ $\pm 4.58 \cdot 10^{-3}$	$1.20 \cdot 10^{-2}$ $\pm 6.51 \cdot 10^{-3}$
10	26.57	$6.76 \cdot 10^{-2}$ $\pm 3.78 \cdot 10^{-2}$	$2.20 \cdot 10^{-2}$ $\pm 1.20 \cdot 10^{-2}$	$1.46 \cdot 10^{-2}$ $\pm 7.93 \cdot 10^{-3}$	$8.83 \cdot 10^{-3}$ $\pm 4.78 \cdot 10^{-3}$	$1.26 \cdot 10^{-2}$ $\pm 6.80 \cdot 10^{-3}$

Table 6.6: Table of the FAD values of the loudest foreground events, based on each of the 5 EBBH waveforms studied.

ID	SNR	EBBH A (%)	EBBH B (%)	EBBH C (%)	EBBH D (%)	EBBH E (%)
1	29.78	~ 100	~ 100	95	94	84

Table 6.7: Table of the FAP values of the loudest foreground event, based on each of the 5 EBBH waveforms studied. The next events have a FAP compatible with 100 %.

EBBH A ($\mathrm{Mpc^{-3}yr^{-1}}$)	EBBH B ($\mathrm{Mpc^{-3}yr^{-1}}$)	EBBH C ($\mathrm{Mpc^{-3}yr^{-1}}$)	EBBH D ($\mathrm{Mpc^{-3}yr^{-1}}$)	EBBH E ($\mathrm{Mpc^{-3}yr^{-1}}$)
$3.73 \cdot 10^{-2}$	$1.23 \cdot 10^{-2}$	$8.56 \cdot 10^{-3}$	$5.15 \cdot 10^{-3}$	$7.15 \cdot 10^{-3}$

Table 6.8: Table of the rate upper limits for the 5 EBBH waveforms studied.

the pipeline, a detection remains unlikely. However in the future, improvement of the EBBH detection capabilities of STAMPAS will be a primary goal.

6.3 Concluding remarks

The STAMPAS analysis on S5 data revealed a very clean trigger distribution for the zero lag, extremely close to the simulated MC data. For ADI signals, the background was well understood and the upper limits indicate that the next generation of ground-based detectors should be able to either make a detection or set constraining upper limits. Sensitivity to EBBH signals will be improved in the future, although the results we obtained are very promising already.

This analysis was only a first step, and others will follow soon. In particular, the LIGO S6 run should be straightforward to analyze, at least for the H1L1 pair. Virgo data will in particular be taken into account for this analysis, allowing us to exploit results coming from three pairs of interferometers instead of one. In the next section we will among other things discuss the studies done so far to include a third interferometer into the pipeline.

Chapter 7

Improving STAMPAS

"One more thing..."

Steve Jobs

Although STAMPAS was able to set significant upper limits, it is possible to improve it even further. In this chapter we will expose the different unresolved issues encountered during the development of STAMPAS, and the possible solutions which have been studied or planned. We will also introduce future developments planned for the pipeline.

7.1 Known pipeline issues

7.1.1 The variance estimation

As described in section 4.1.1, the Y quantity variance, σ_Y, is estimated using, for a given (t, f) pixel, the neighboring pixels with the same frequency (see equation (4.6)). This estimation is biased when a significant signal power is present in the pixels used for the variance calculation. As a consequence, signals with power at a given frequency that last for more than δt seconds (the time resolution), will have their SNR artificially damped to ~ 1 or less. Hence, the STAMPAS pipeline has a poor sensitivity to signals for which the frequency is varying at a

rate inferior to $\delta f/\delta t$ Hz s^{-1} with $(\delta f, \delta t)$ the binning resolution of the *ft*-maps; its SNR will then be underestimated. In the case where the signal is locally monochromatic for more than $N\delta t$ seconds, where N is the number of time segments chosen to estimate the variance, the signal can be totally suppressed due to the noise estimation method. In the extreme case of monochromatic signals, this suppression is very significant. In figure 7.1, a *ft*-map where a strong quasi-monochromatic injection has been done in MC noise is presented. The SNR calculated by STAMPAS is weak, even if on the map presenting the raw Y statistic, the signal is clearly present.

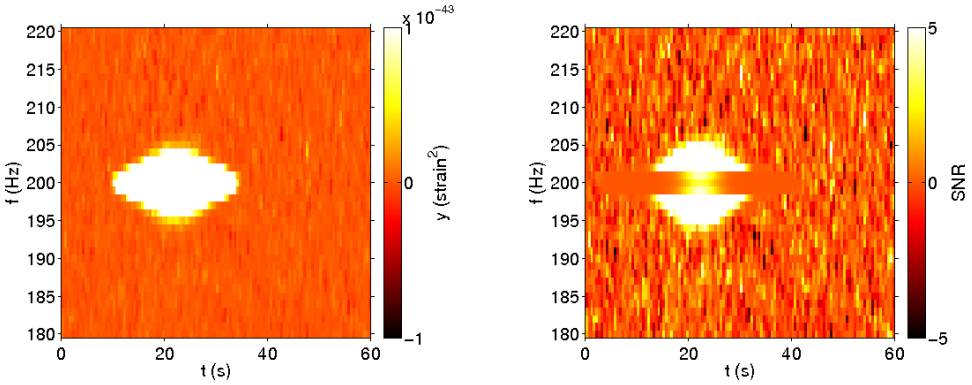

(a) Y *ft*-map of a strong monochromatic signal injected in MC noise

(b) SNR *ft*-map of a strong monochromatic signal injected in MC noise

Figure 7.1: *ft*-maps show that the SNR of the injection is damped, even though the injection is integrally visible in the Y map. The effect is clearly visible at the frequencies where the signal lasts longer.

This flaw in the SNR estimation makes the pipeline nearly blind to monochromatic signals and slowly varying signals such as neutron stars' r-modes for example. One of the goal of the STAMPAS pipeline is to make as little hypothesis on the signals as possible, a goal which is not currently reached due to the noise estimation.

Alternative sigma

The efforts to correct the noise estimation were first directed toward a slight modification of the Y variance estimation, which would not affect too much the core of the pipeline. The idea was to estimate the variance, for a given pixel, not by using its neighboring pixels, but pixels located elsewhere on the map. To achieve this without modifying to deeply the core of the pipeline, we tested the following alternative variance estimator, called *alternative sigma*. The Y map is calculated as before, and the variance estimator, σ_Y^2, is calculated normally. Then, before calculating the SNR of each pixel, the *ft*-map of the σ_Y values is split in two halves, which are exchanged. Numerically, for a Ts long map, we have the following:

$$\begin{cases} \text{If } \tau \leq T/2, \text{ then: } \sigma_Y(\tau, f) \leftarrow \sigma_Y(\tau + T/2, f) \\ \text{If } \tau > T/2, \text{ then: } \sigma_Y(\tau, f) \leftarrow \sigma_Y(\tau - T/2, f) \end{cases} \tag{7.1}$$

If T is an odd number, the first column is not affected by this change. Note here that the number of bins necessary to calculate σ_Y is optimized as presented in 4.1.1.

With this modification, monochromatic or slowly varying signals' SNR increased significantly. In figure 7.2 are two example of injections realized on MC noise. The left map uses the regular STAMP calculations, the right map uses alternative sigma. Note here that we can see how badly the ADI D waveform could be affected by the regular STAMP noise estimation (as stated in 5.4.5). Other ADI waveforms, such as ADI A, are also affected by this issue, but much less. The new value of the SNR, although significantly higher in both cases, should not be directly compared to the previous value, since the noise estimation is different.

To check that this modification of the way the SNR is estimated doesn't affect signals which otherwise are recovered correctly, ADI B waveform has been injected in MC data with or without the alternative sigma calculation, see figure 7.3.

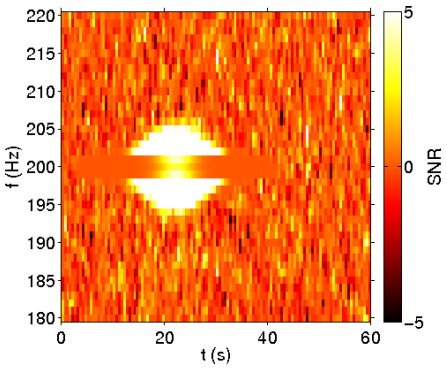

(a) SNR *ft*-map of a strong monochromatic signal injected in MC noise with the regular STAMP calculations. Recovered SNR ~ 300

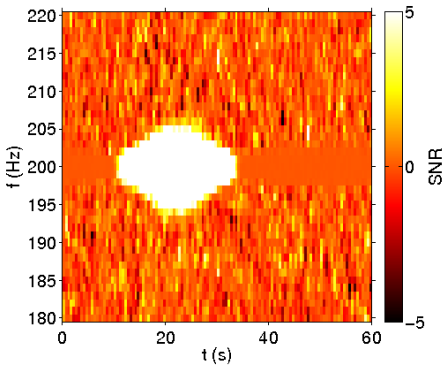

(b) SNR *ft*-map of a strong monochromatic signal injected in MC noise with the alternative sigma option active. Recovered SNR $\sim 2 \cdot 10^6$

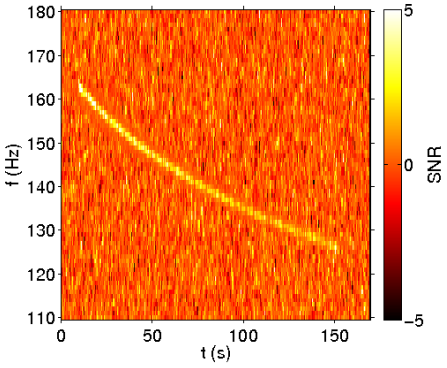

(c) SNR *ft*-map of an ADI D signal injected in MC noise with the regular STAMP calculations. Recovered SNR ~ 40

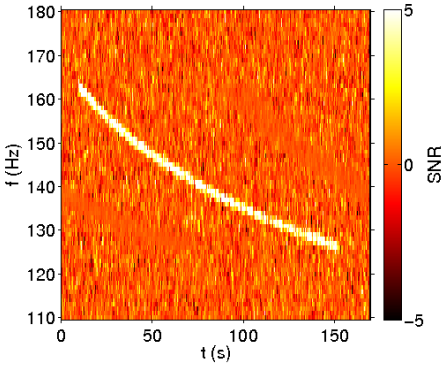

(d) SNR *ft*-map of an ADI D signal injected in MC noise with the alternative sigma option active. Recovered SNR ~ 150

Figure 7.2: *ft*-maps show that the injections are more visible using alternative sigma.

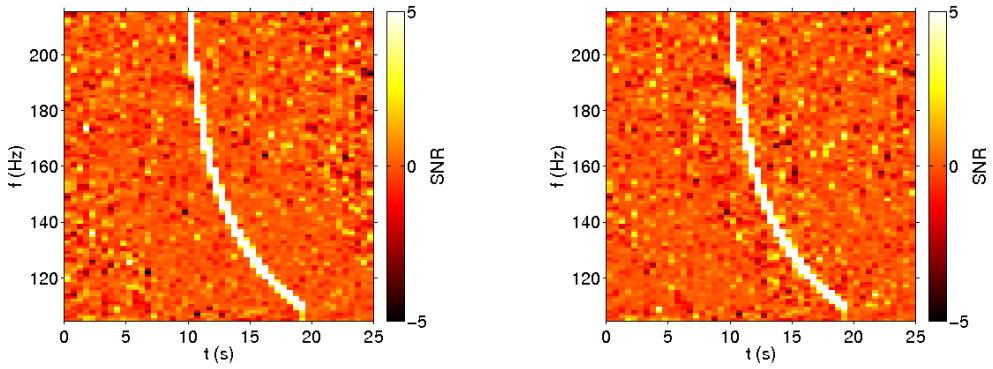

(a) SNR *ft*-map of an ADI B signal injected in MC noise with the regular STAMP calculations. Recovered SNR ~ 360

(b) SNR *ft*-map of an ADI B signal injected in MC noise with the alternative sigma option active. Recovered SNR ~ 310

Figure 7.3: *ft*-maps show that the injection SNR is similar in both cases.

In this example the new value of the SNR is slightly lower than the standard value, which can be explained by the fact that the pixels surrounding the signal have a SNR close to 0 in the standard noise estimation, which is not true anymore using alternative sigma. This effect depends on the shape of the signal. This has been shown by making a 1000 injections in MC noise of the same ADI waveform, and calculating the SNR with and without the alternative sigma option, but without using, for a given pixel, the 2 pixels before and the 2 pixels following in frequency for the noise estimate. At this condition, the averaged recovered SNR was the same in both cases.

The effect on signals rapidly varying in frequency is therefore negligible. However, before using this modification for the analysis, test were done to study the effect of this modification on the background study.

A week of data was from the S6 scientific run of LIGO, has been analyzed with STAMPAS, using a single time slide. In figure 7.4 is shown the FAR curve for the background distribution of data with and without using the alternative sigma option. It can be seen that number of generated triggers is greater with alternative sigma. Also the tail of the distribution seems to be larger.

To confirm this observation, 20 time slides, using the same S6 week, has been performed. Results of this study are shown in figure 7.5. The FAR distribution is compared with the distribution obtained with the same amount of MC data. The increasing of the tail is therefore extremely important when the amount of data processed is significant.

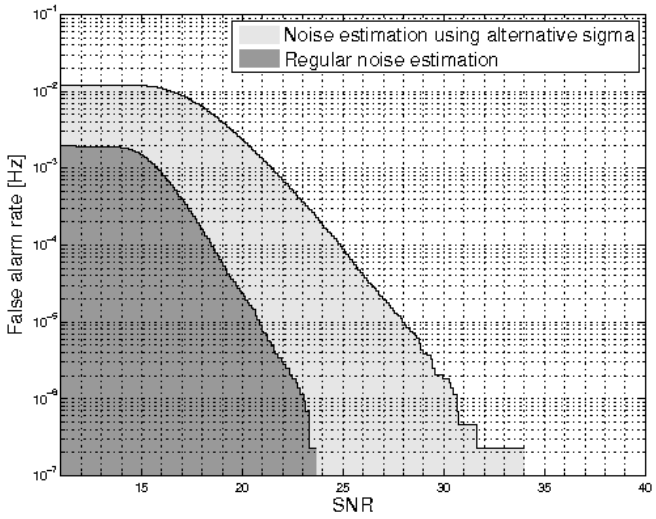

Figure 7.4: FAR distribution of one week of S6 data using one time slide, with and without using alternative sigma. Using alternative sigma increases the number of noise triggers generated as well as the number of events in the distribution tail.

A large distribution tail indicates that we detect more glitches in the data using alternative sigma. In figure 7.6 can be seen an *ft*-map analyzed with and without alternative sigma. Glitches invisible or weak with the regular variance calculation appear very strong with alternative sigma.

To maintain the efficiency of the search to a reasonable level, data selection should allow us to reject as many of these glitches as possible. The use of an extended glitch cut (see next section) reduced significantly the number of loud events, as it can be seen in figure 7.5, but it has been found difficult to reduce the background any more. At this point it has been decided to run the first analysis without using alternative sigma, however investigations on this study

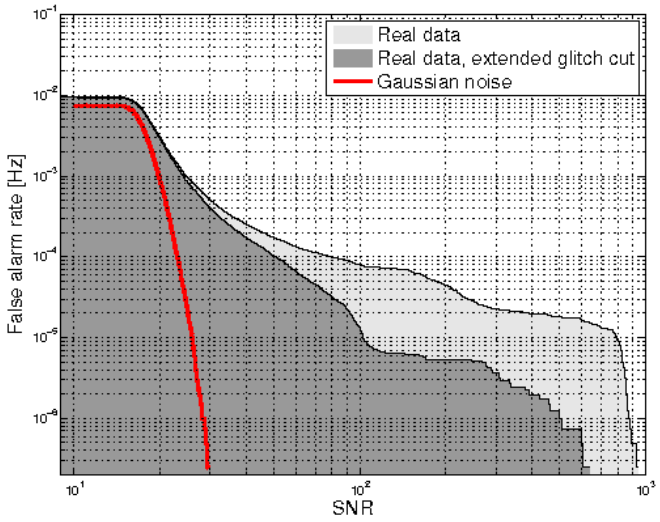

Figure 7.5: FAR distribution of one week of S6 data using 20 time slides, with and without using the extended glitch cut, compared with a FAR distribution built with an identical amount of simulated data.

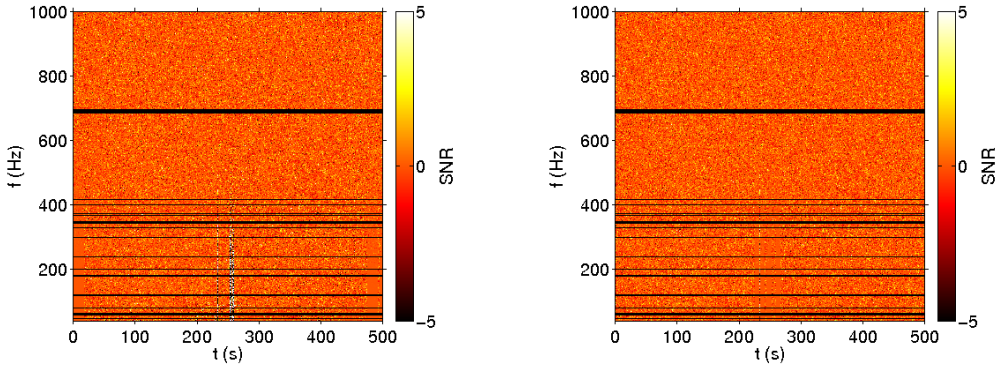

(a) SNR *ft*-map of a glitch in H1L1 data, calculated using alternative sigma. Recovered SNR ~ 7600

(b) SNR *ft*-map of a glitch in H1L1 data, calculated not using alternative sigma. Recovered SNR ~ 16

Figure 7.6: *ft*-maps show that the same glitch in the data yields very different SNR values depending if alternative sigma is used or not.

will be resumed after the results of the S5 analysis are final. In particular we plan to use the newly developed SNR fraction quantity to reduce even more the background.

Other solutions

Other solutions to the variance estimation issue have been considered. The first one would be to use the standard variance calculation, but without considering the closest pixels in the calculation. This would strengthen the SNR of several models of waveform (including the ADI D model), with very small changes brought to the code. However it would have little impact on monochromatic signals and do not solve satisfyingly the problem.

Another considered solution, which would require deeper modification to the core of the STAMP algorithm, was to change the definition of the variance estimator σ_Y, by using not a mean over neighboring pixels, but the median of their values, with the exception of the strongest pixel(s). Strong but short variations of power wouldn't affect much this value, however the monochromatic signals would still be missed using this method as it is.

In both cases, studies of the background should be performed to understand their impact on the sensitivity of STAMPAS to the short glitches.

7.1.2 Waveforms trustworthiness

Another issue we encountered during STAMPAS development was that when performing loud injections with ADI waveforms, unphysical excesses of power appeared at the start and/or at the end of the injected signal on the *ft*-maps (see figure 7.7). These artefacts only appear with strong waveforms – corresponding to signal coming from sources unlikely close to the Earth – and cause the pipeline glitch cut to flag the injections. The first hypothesis on the cause of this effect was that the waveforms weren't well conditioned. Indeed, for computational and physical reasons, the waveforms we inject in the data must have a null amplitude at their beginning, amplitude slowly increasing, and they must end with a slowly decreasing amplitude to a final null amplitude. An exponential damping has

been introduced at the beginning and at the end of the ADI waveforms, but the artefact remained.

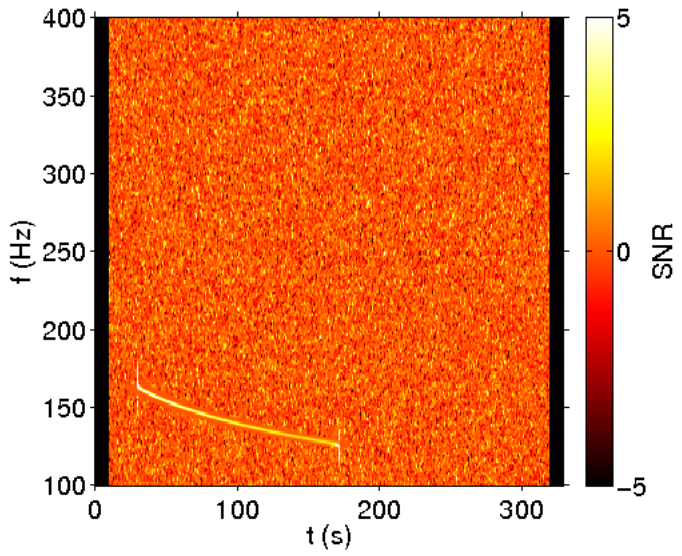

Figure 7.7: *ft*-map with an ADI injection made on MC noise. Unphysical burst of energies are present at the beginning and at then end of the waveform.

The cause of this effect does not come from the waveforms themselves, and we suspect a numerical effect appearing somewhere in the code. Investigations are in progress to understand and suppress this effect which does not affect the results for plausible injections, but points to a weakness of the pipeline. As a matter of principle, STAMPAS should recover strong injections and never reject them as glitches.

7.1.3 Data selection

As stated in 5.2.1, common science data between the two detectors used by STAMPAS are divided in time windows of $\mathcal{O}(100\text{s})$. Time fragments which are not contained in such divisions were ignored during the S5 analysis. 8.76% of the data weren't analyzed due to this choice. To include these data into the next analysis run with STAMPAS, it is planned to divide the data differently, in

order to span all the data contained in the selected data segments. First, on the common science data for a given pair of detector, the data segments shorter than the minimal duration of the *ft*-maps, noted T, would be rejected, as it has already been done. On the remaining segments, longer than this minimal duration, the data would be divided as before in windows of T seconds, with a minimal constant overlap of $T_{overlap}$ seconds. Let us assume that after the division, a segment t_{rest} seconds, with $t_{rest} < T - t_{overlap}$ not included in the last map, isn't long enough to form itself a new window. Then, we would introduce a supplementary time window, overlapping with the previous map by $T - t_{rest}$ seconds. Some data would be analyzed more than necessary, but the entire science segment would be spanned.

This spanning hasn't been included in the S5 analysis because its implementation wouldn't be trivially compatible with STAMPAS timeshifts method, and that it wasn't time enough to solve these problems. However this method will be implemented in the future versions of the pipeline.

7.1.4 Computing speed

Currently, the computing requirements of STAMPAS allow one to process about 1 year of data, with 100 lags, in about 10 days. These results were obtained on the California Institute of Technology cluster, using about 300 CPUs in parallel. According to the burst group white paper [99], this is about 20 times slower than the reference pipeline for short transients, the cWB pipeline [75]. This is essentially due to input/output processes. Reducing computing speed of the pipeline will be an important part of future STAMPAS studies. It will allow the processing of a greater background, which would increase the reliability of the upper limits obtained using STAMPAS, along as the significance of the candidates we could find.

7.2 Future developments

7.2.1 Extended glitch cut

To further reduce the tail of the FAR distribution, it has also been considered to use the STAMP internal glitch cut as a flag. The list of GPS times vetoed by the glitch cut would be saved, and using this list we could veto any trigger happening in a $\pm t_{gc}$ second window near a glitch cut. More specifically, if the glitch cut is triggered at a time t_0, every trigger in coincidence with it, within a $2 \cdot t_{gc}$ window, would be notched independently of the sky direction investigated. The idea being that depending on the antenna factors for instance, a glitch may or may not be caught by the glitch cut. If a glitch is flagged by the cut in one direction, it is removed in every other direction.

This procedure wasn't applied during the S5 analysis, because the background was nearly gaussian, and tests have shown that using this extended glitch cut didn't improve the background distribution. Also, in the current state of the pipeline, the detection efficiency of the ADI waveforms would have been impacted do to the artefact described in 7.1.2. The artefacts present at the beginning and the end of some injections tend to trigger the glitch cut. Therefore, injections would have been vetoed by the extended glitch cut if it had been used.

However, when this problem will be solved, the extended glitch may prove itself useful if a different noise estimation technique, such as alternative sigma described in 7.1.1, is used. Indeed, this procedure has been experimented during the S6 week test described earlier, which used alternative sigma. Results, which can be seen in figure 7.5, show a significant improvement of the FAR distribution.

7.2.2 Coherence check with better time resolution

It has been noticed that several high SNR triggers were caused by two glitches happening in both interferometers at the same time (taken into account the time shift) in a time window shorter than STAMPAS resolution. However, two power excesses in two different interferometers can only be caused by the same

gravitational wave signal if they happen at less than $\delta_{IJ}t$ seconds, where $\delta_{IJ}t$ is the light travel time between the two interferometers I and J, remembered in table (2.2). This reasoning is true if and only if the time accuracy of the two experiments is good enough. In table 7.1 we summarize the timing calibration error of H1, L1 and V1. They are much smaller than the maximal time of flight, which allows us to use the time difference between two events in different experiments to determine if they are or not physically related.

Interferometers	Timing calibration error at 100 Hz (ms)
H1	0.125
L1	0.117

Table 7.1: Timing calibration error for LIGO interferometers measured during the S5 run [94]. These value are given for signals of frequency 100 Hz. They are inversely proportional to signal frequency: they are ten times greater for 10 Hz signals, and 10 times lower for 1000 Hz signals.

STAMPAS resolution is of the order of 1s. Therefore, two glitches separated by more than $\delta_{IJ}t$ seconds may well be correlated by STAMPAS and generate a trigger even though they are not physically correlated.

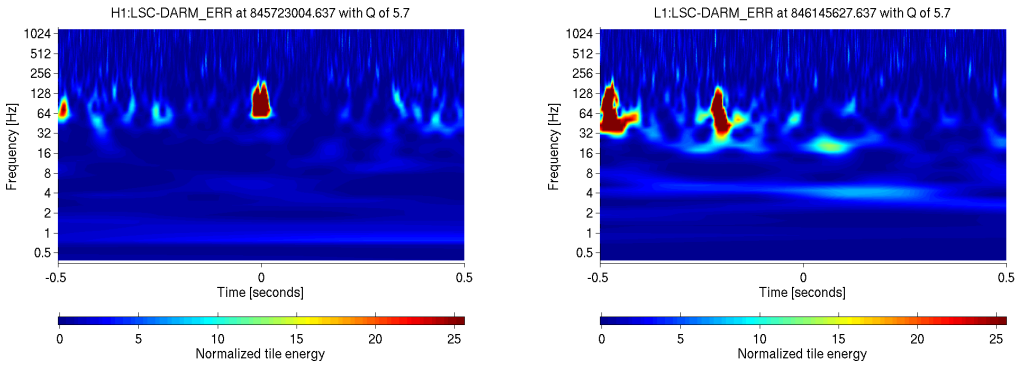

(a) OMEGA scan seen in H1.

(b) OMEGA scan seen in L1.

Figure 7.8: Background event 56 of the list of ranked events of the S5 analysis. The glitches present in H1 and L1 are separated by more than 10ms, however due to STAMPAS resolution, they are seen as correlated to one another.

In figure 7.8 are shown two *ft*-maps done with the OMEGA tool [100], corresponding to a part of the background trigger number 56 (see Appendix A) from the S5 analysis described in the previous chapter. This trigger is composed of several short glitches of the same kind than the one shown in 7.8. The windows are centered on the same time taking into account the time shift applied, *i.e.* the time corresponding to the center of the windows are correlated with each other in STAMPAS. It can be seen with this example that glitches are clearly visible in both interferometers, but are separated by more then 10ms, which is the light travel distance between H1 and L1. They are then not caused by a true gravitational wave. This is true for all the glitches composing the background trigger number 56; it can therefore be identified as a noise trigger.

To remove systematically the concerned triggers, the time between power excesses in both interferometers have to be quantified, so we can implement a cut. Future work on the pipeline will include the implementation of a variable characterizing the precise temporal separation between power excesses in different experiments. This might be done within STAMPAS itself, during the processing of the interferometers data stream, while STAMPAS resolution doesn't prevents us to do so. Until this is done, triggers such like the trigger 56 can't be rejected.

7.2.3 Including a third interferometer

The STAMPAS pipeline works with a pair of interferometers. Therefore, it can not provide an exact location of the signals it can detect, but only a ring of possible sources in the sky. To suppress any ambiguity in the detection, it is necessary to add a third interferometer to the network, as it has been done in other coherent pipelines (see [69, 70, 71, 74, 75, 76, 80]). They are two different possibilities on how exactly to do this.

The first possibility is to run three STAMPAS analysis, as described in this thesis, using each time a different pair of interferometer. Whenever a significant trigger is detected in any of the pair, we could run a complete all-sky analysis, on every possible ring in the sky, on the appropriate time segment in each pairs of detectors. We would obtain three sky maps, indicating for each sky position

the maximal SNR recovered with STAMPAS. We could combine these maps to extract the position of the signal's source. In figures 7.9a, 7.9b and 7.9c, are presented the three all-sky maps obtained with respectively the pairs H1L1, L1V1 and V1H1. The same injection (an ADI waveform) has been performed, at the same time, in MC data, at position (5h,80 °). In figure 7.9d, the maps have simply been multiplied to each other. The cyan cross indicates the local maxima of the map, which are the possible sources of the signal.

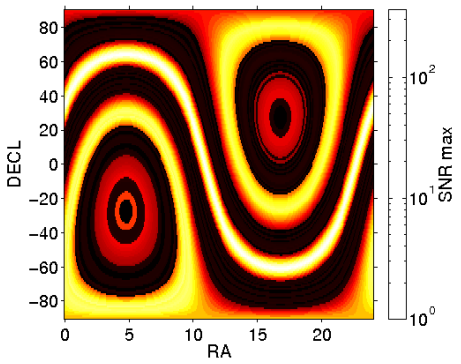

(a) Skymap for the H1L1 pair.

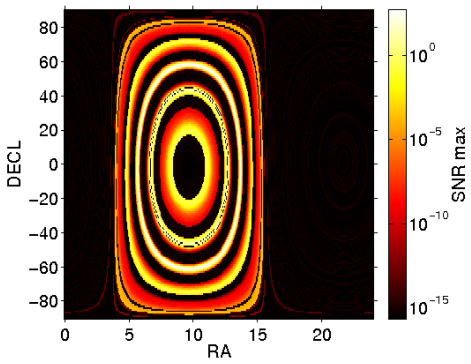

(b) Skymap for the H1V1 pair.

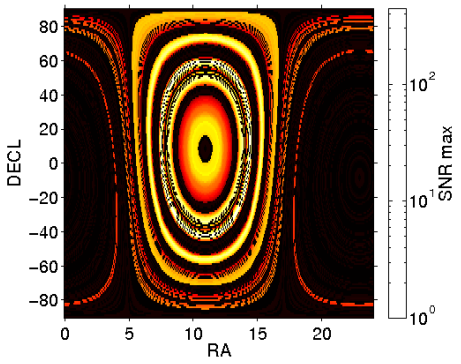

(c) Skymap for the V1L1 pair.

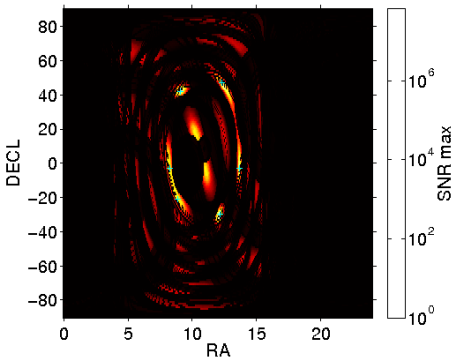

(d) Product of the above sky maps.

Figure 7.9: Skymaps obtained for the different pairs of interferometers for a given injection. On the (d) map, the cyan crosses indicates local maxima at most 20% inferior to the absolute maximum of the $\Pi_{pairs}\mathrm{SNR}_{IJ}$. The injection has been made at (5h,80 °).

To study the efficiency of this reconstruction, we plotted for 10000 trials, the angular separation between the true injection and the reconstructed position with the loudest recovered SNR, for both right ascension and declination, when the injection was recovered with an SNR greater than 40. We used an ADI waveform as the injected signal. As can be seen in figure 7.10, the curves are centered on 0, when 3 all three pairs generated a trigger.

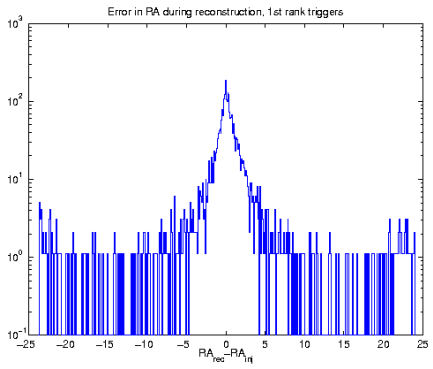

(a) Angular separation in right ascension. Distribution half-width is $\sigma_{RA} \sim 11\,^{\circ}$.

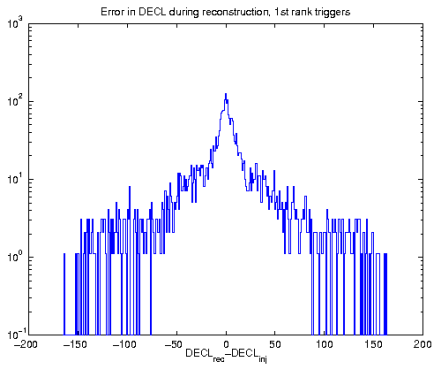

(b) Angular separation in declination. Distribution half-width $\sigma_{DECL} \sim 11\,^{\circ}$ as well.

Figure 7.10: Angular separations in right ascension and declination between the reconstructed positions and the true position of the injection, in the case where all pairs of detectors recovered the injection.

The injected signal was polarized, we can deduce that the uncertainty due to the fact that STAMPAS does not take into account the polarization of the signal is on average compensated. However the spatial resolution of theis test was low. Indeed, 50% of the injections are recovered with a maximal angular separation to the true injection of $\sim 11\,^{\circ}$ in both right ascension and declination when the three pairs of interferometers produced a trigger. This angular separation doubles when only two pairs generated a trigger of SNR above 40. Different combinations of the results from the three pairs than the simple multiplication of the recovered SNR in every direction should be tested in the future.

The second possibility to combine the results from the three pairs would be to modify the statistic we use. The STAMP statistics described in 4.1.1 can be adapted to take into account the results from several pairs of detectors, instead of using just one pair. The sums in equation (4.9) and (4.10) can be done on all the pixels corresponding to the trigger you are interested in, taken in the three different maps corresponding to the three pairs you analyzed, *i.e.*

$$\mathcal{Y}_\Gamma(\vec{\Omega}) = \frac{\sum_{(I,J)} \sum_{(\tau,f)\in\Gamma} Y^{IJ}(\tau,f,\vec{\Omega})\sigma_Y^{IJ}(\tau,f,\vec{\Omega})^{-2}}{\sum_{(I,J)} \sum_{(\tau,f,\vec{\Omega})\in\Gamma} \sigma_Y^{IJ}(\tau,f,\vec{\Omega})^{-2}} \tag{7.2}$$

and

$$\sigma_\Gamma^2(\vec{\Omega}) = \left(\sum_{(I,J)} \sum_{(\tau,f)\in\Gamma} \sigma_Y^{IJ}(\tau,f,\vec{\Omega})^{-2} \right)^{-1} \tag{7.3}$$

where (I, J) are the possible pairs of detectors. In other words using this averaged statistics, a global *ft*-map can be generated from the three separated maps corresponding to each pair. If we use this solution, the pipeline should be modified to analyze simultaneously the *ft*-maps of each three pairs of detectors, in such a way it could generate the combined *ft*-maps. No studies have been performed yet on such combined statistics.

7.2.4 EBBH waveforms

EBBH signals are difficult to recover with STAMPAS due to some of their characteristics that they share with the background, especially an outburst of power during the last second. During the in spiral phase of the signal, the waveform appears in the *ft*-maps like a succession of short broadband signals. This characteristic might be used to conceive an alternate clustering algorithm dedicated to the detection of such signals. In any case it seems difficult to reach equal sensitivity to categories of signal like ADI and EBBH, with the current state of the pipeline. However, improvements discussed above might help filling the gap between these two categories.

Conclusion

The STAMPAS pipeline is the first all-sky pipeline dedicated to the search of long transient signals, lasting from $\mathcal{O}$(1s) to $\mathcal{O}$(500s). Designed without priors on the behavior of the signals investigated, its efficiency has been evaluated using two different families of waveforms: Accretion Disk Instabilities (ADI) and Eccentric Binary Black-Holes (EBBH). The first STAMPAS analysis was performed on data coming from fifth scientific run of the LIGO experiments. Only the pair composed of the Hanford and Livingston interferometers was investigated.

The analysis of the background showed that, after rigorous data selection, the noise profile was close to gaussian noise. The pipeline results can not be significantly improved by a better understanding of the noise. No foreground event passed the selection criteria. The loudest of them, with an energy SNR of 29.78, has a false alarm probability of about 60 % depending on the ADI model considered. Using the false alarm density statistic, and based on the efficiency studies of ADI signals, we can attribute a false alarm density comprised between $3.60 \cdot 10^{-3}$ and $1.30 \cdot 10^{-5}$ $\mathrm{yr}^{-1}\mathrm{Mpc}^{-3}$ to this event. Using the loudest event statistic, we deduced upper limits on the rate of ADI signals going from $3.77 \cdot 10^{-2}$ to $1.43 \cdot 10^{-4}$ $\mathrm{Mpc}^{-3}\mathrm{yr}^{-1}$.

The EBBH waveforms have proven more difficult to detect with the current version of pipeline, their characteristics tend to trigger the different cuts used to separate background from foreground events. Specifically, the high peak in energy during the final moments of the signal often leads the pipeline to misidentify these signals as background artefacts. As a consequence, their study has been done with less restrictive background selection, leading to upper limits comprised between

$3.73 \cdot 10^{-2}$ and $5.15 \cdot 10^{-3}$ $\mathrm{Mpc}^{-3}\mathrm{yr}^{-1}$. Considering the difficulties encountered by STAMPAS to efficiently detect EBBH, it is likely that a specific version of the pipeline would have to be considered to detect such signals with an efficiency comparable to the ones achieved with ADI waveforms.

The STAMPAS pipeline has several issues which will be fixed in the near future. The main drawback of the pipeline is the noise estimation performed on the *ft*-maps. In its current state, STAMPAS is poorly sensitive to signals with a frequency evolution stationary on a timescale larger than the time resolution of the pipeline. It is insensitive to monochromatic signals. Several ideas are currently explored to correct this weakness.

Despite these imperfections, the potential of the STAMPAS pipeline has largely been demonstrated, through results we obtained. Considering the ADI signals, we managed to obtain a nearly gaussian background, and to set good upper limits on various signal models. As it is the first of its kind to investigate specifically the long transient signals, I wish that people will continue to improve it, so when LIGO and Virgo enter the Advanced Detector Era, STAMPAS would have become one of the main pipelines used by the LIGO-Virgo collaboration.

Appendix A

Loudest background triggers in S5 analysis

Id	SNR	GPS time in H1	GPS time in L1	Dur. (s)	f_{min} (Hz)	f_{max} (Hz)	SNR_{frac}	Cut by
1	1790.29	873240388.5	873348988.5	0.5	183	327	1.00	*†
2	1262.78	846218948.0	846400285.0	2.0	64	117	0.99	†
3	539.78	870799093.0	870842972.0	1.5	194	285	0.83	*†
4	423.91	841767619.5	842078846.5	1.0	151	221	0.77	*†
5	394.44	866999331.5	867143080.5	3.5	90	271	0.98	*†
6	333.60	870799093.0	870924742.0	1.5	252	316	0.60	*†
7	*267.07*	*865521222.0*	*865538447.0*	*2.0*	*80*	*177*	*0.60*	†
8	173.87	854528863.0	854638651.0	2.0	64	165	0.99	†
9	152.09	850062526.0	850171098.0	15.0	40	117	0.87	†
10	125.99	819004509.5	819338425.5	2.5	79	168	0.95	†
11	107.60	849353435.5	849425938.5	2.5	183	260	0.98	†
12	99.95	842665387.5	842761825.5	17.5	69	175	0.92	†
13	87.26	829494563.5	829582772.5	17.5	72	117	0.82	†
14	86.81	851760540.0	851948893.0	3.0	135	223	0.91	†
15	83.56	867285623.5	867395799.5	3.0	123	293	0.86	†
16	82.15	872931405.0	873145189.0	3.0	90	177	0.89	*†

17	80.86	870799093.0	870842972.0	1.0	350	429	0.52	*†
18	72.69	837246215.0	837248312.0	3.0	123	177	0.91	†
19	71.39	872274217.0	872379038.0	4.0	67	172	0.91	†
20	70.67	852772663.5	852849264.5	2.5	64	117	0.90	*†
21	66.02	848834238.0	849133945.0	3.5	123	177	0.92	*†
22	62.45	863116928.5	863244108.5	19.5	73	164	0.79	*†
23	61.92	873577724.5	873629006.5	3.0	140	205	0.90	*†
24	59.70	853160981.0	853255166.0	3.0	123	177	0.92	†
25	58.04	870464486.0	870477349.0	4.0	64	117	0.89	†
26	54.89	844818046.5	844824481.5	4.0	64	112	0.92	†
27	54.74	852910306.0	852984078.0	4.5	64	117	0.89	†
28	54.43	863148385.5	863235283.5	3.0	64	150	0.94	†
29	52.34	846334248.5	846397545.5	2.0	64	113	0.65	†
30	51.73	846179752.0	846323627.0	2.5	66	117	0.76	†
31	48.62	871711977.0	871770993.0	4.0	79	168	0.83	*†
32	47.38	873240386.5	873348986.5	5.0	382	471	0.89	*†
33	46.88	852610036.0	852803145.0	4.0	64	145	0.84	†
34	46.65	870788371.5	870888154.5	3.0	525	578	0.66	*†
35	45.91	872573505.5	872574690.5	56.5	183	327	0.07	*
36	43.92	846397466.0	846555633.0	3.0	64	155	0.85	†
37	43.19	844370196.5	844502478.5	16.5	89	115	0.25	*
38	43.00	832649592.5	832730427.5	13.5	103	168	0.72	*†
39	41.56	850686076.0	850797242.0	5.0	64	115	0.73	†
40	40.30	831632178.0	831704149.0	6.0	130	203	0.75	*†
41	39.78	847432082.0	847793800.0	4.5	43	117	0.70	†
42	38.52	818554205.0	818567360.0	3.0	129	225	0.67	†
43	38.43	818929463.5	818941129.5	3.5	127	211	0.83	†
44	**38.36**	**870807903.5**	**870880740.5**	**19.5**	**160**	**230**	**0.46**	**-**
45	38.18	844904670.5	845339224.5	4.0	65	117	0.76	†
46	38.06	862715623.0	862820090.0	3.0	183	238	0.66	*†
47	37.33	844497551.0	844813902.0	3.5	64	107	0.73	†

48	37.05	847102209.0	847105955.0	4.5	68	154	0.85	†
49	36.21	870839913.5	870879393.5	19.0	374	448	0.12	*
50	36.02	860476020.5	860725759.5	14.0	72	117	0.65	*†
51	35.83	869861329.0	869959067.0	21.5	188	312	0.13	*
52	35.75	834971587.5	835624757.5	5.5	64	155	0.44	*
53	35.72	872500300.5	872574716.5	45.5	589	715	0.10	*
54	35.48	846849840.5	847348530.5	33.5	65	113	0.17	-
55	35.07	863100796.0	863297118.0	5.0	64	115	0.85	*†
56	35.06	852264720.5	852282438.5	5.0	86	117	0.47	-
57	35.03	869808500.5	869959080.5	23.5	463	578	0.13	*
58	34.85	870965908.0	871103198.0	27.0	219	323	0.10	*
59	34.77	834079506.5	834292256.5	18.5	64	114	0.62	†
60	34.64	871080862.0	871284844.0	5.5	64	117	0.30	*
61	34.62	853391616.5	853466395.5	8.5	40	112	0.65	*†
62	34.28	856369603.5	856416176.5	17.5	64	100	0.46	-
63	34.27	857775521.5	857811214.5	13.5	90	151	0.68	†
64	34.24	852361691.0	852528686.0	4.5	101	154	0.30	-
65	34.18	871074147.5	871212179.5	41.5	154	234	0.08	*
66	33.98	845722990.0	846145613.0	15.5	64	112	0.39	-
67	33.85	871080861.0	871220103.0	6.5	64	108	0.21	*
68	33.78	844370236.5	844374108.5	6.5	66	110	0.27	-
69	33.73	847214708.5	847354065.5	16.5	65	116	0.30	-
70	33.60	847426399.5	847803834.5	4.0	152	234	0.51	†
71	33.29	847287158.0	847324948.0	21.0	64	88	0.28	-
72	33.28	846292602.5	846420058.5	16.5	69	117	0.37	-
73	32.97	847502098.5	847800338.5	5.0	45	95	0.48	-
74	32.95	871090940.0	871103203.0	22.5	123	216	0.15	*
75	32.82	874737600.5	874961049.5	16.0	242	324	0.15	*
76	32.58	846433917.0	846503369.0	2.5	64	117	0.71	†
77	32.53	849887540.0	850011558.0	19.5	74	116	0.20	-
78	32.51	849883940.5	850119023.5	19.0	64	117	0.15	-

79	32.49	872442477.5	872574689.5	34.0	620	679	0.16	*
80	32.47	870844322.0	870879392.0	25.0	787	882	0.15	*
81	32.38	869922867.0	869959069.0	18.5	195	305	0.21	*
82	32.37	824721030.5	825704813.5	8.5	64	177	0.18	-
83	32.32	849887475.0	850106926.0	41.5	749	847	0.06	-
84	32.29	850009830.5	850171220.5	28.0	410	507	0.08	-
85	32.27	871063522.5	871212319.5	26.0	244	325	0.16	*
86	32.11	871080862.5	871204089.5	4.0	73	117	0.30	*
87	32.08	874955244.0	874961060.0	6.0	222	327	0.17	*
88	31.85	855179245.5	855220760.5	56.0	358	427	0.04	-
89	31.84	869867650.5	869959081.5	21.5	858	967	0.16	*
90	31.82	847487778.5	847776397.5	28.5	64	106	0.41	-
91	31.73	832541935.0	832758714.0	27.0	413	516	0.06	-
92	31.73	839016981.5	839182315.5	4.5	74	117	0.65	*†
93	31.72	871080861.5	871206048.5	5.0	76	117	0.23	*
94	31.55	834980098.5	835591114.5	35.5	858	989	0.05	-
95	31.29	862700360.5	862739607.5	35.0	430	503	0.07	*
96	31.29	871080862.0	871115800.0	4.5	66	117	0.22	*
97	31.28	870769053.0	870886523.0	25.0	533	676	0.18	-
98	31.27	870994244.0	871103429.0	24.5	404	488	0.12	*
99	31.26	847216886.5	847358977.5	4.0	64	117	0.23	-
100	31.19	846651357.5	846739568.5	3.5	64	114	0.82	†

Table A.1: Table of the 100 loudest triggers obtained during the S5 background analysis. The bold line represents the loudest trigger for the ADI analysis after all the cuts are applied. The italic line represents the loudest trigger for the EBBH analysis after all the cuts are applied. The H1 and L1 times are the absolute GPS times associated with the event, Dur. is the duration of the trigger, $f_{min/max}$ its minimal and maximal frequency, SNR_{frac} the maximal value reached by the SNR fraction in the trigger. In the last column, a $*$ symbol appears when the trigger is removed by a data quality flag, and a † when in its removed because of its SNR_{frac} value, and - when the trigger is not removed by any mean.

Bibliography

[1] J. Weisberg, D. Nice, and J. Taylor. Timing Measurements of the Relativistic Binary Pulsar PSR B1913+16. *Astrophys.J.*, **722**:1030–1034, 2010.

[2] P. Ade *et al.* BICEP2 I: Detection Of B-mode Polarization at Degree Angular Scales. arXiv, 1403.3985. 2014.

[3] B. Abbott *et al.* LIGO: The Laser interferometer gravitational-wave observatory. *Rept.Prog.Phys.*, **72**:076901, 2009.

[4] T. Accadia *et al.* Virgo: a laser interferometer to detect gravitational waves. *Journal of Instrumentation*, **7**(03):P03012, 2012.

[5] S. Weinberg. *Gravitation and Cosmology.* John Wiley and Sons, 1972.

[6] C. W. Misner, K. S. Thorne, and J. A. Wheeler. *Gravitation.* W.H. Freeman and co., 1973.

[7] J. B. Hartle. *Gravity, an introduction to Einstein's General Relativity.* Addison Wesley, 2003.

[8] J. D. E. Creighton and W. G. Anderson. *Gravitational-Wave Physics and Astronomy.* WILEY-VCH, 2011.

[9] A. Einstein. The Foundation of the General Theory of Relativity. *Annalen Phys.*, **49**:769–822, 1916.

[10] J. C. Maxwell. A dynamical theory of the electromagnetic field. *Phil.Trans.Roy.Soc.Lond.*, **155**:459–512, 1865.

[11] A. A. Michelson and E. W. Morley. On the Relative Motion of the Earth and the Luminiferous Ether. *Am.J.Sci.*, **34**:333–345, 1887.

[12] A. Einstein. On the electrodynamics of moving bodies. *Annalen Phys.*, **17**:891–921, 1905.

[13] R. Hulse and J. Taylor. Discovery of a pulsar in a binary system. *Astrophys.J.*, **195**:L51–L53, 1975.

[14] P. R. Saulson. *Fundamentals of Interferometric Gravitational Wave Detectors*. World Scientific, 1994.

[15] J. Weber. Detection and Generation of Gravitational Waves. *Phys. Rev.*, **117**:306–313, 1960.

[16] R. Weiss. Electromagnetically Coupled Broadband Gravitational Antenna. In *Quaterly Progress Report, MIT Research Lab of Electronics*, volume 105, pages 54–76. 1972.

[17] G. E. Moss, L. R. Miller, and R. L. Forward. Photon-Noise-Limited Laser Transducer for Gravitational Antenna. *Appl. Opt.*, **10**:2495–2498, 1971.

[18] T. Accadia *et al.* Calibration and sensitivity of the Virgo detector during its second science run. *Class.Quant.Grav.*, **28**:025005, 2011.

[19] P. R. Saulson. Gravitational wave detection: Principles and practice. *Comptes Rendus Physique*, **14**:288–305, 2013.

[20] B. F. Schutz and M. Tinto. Antenna patterns of interferometric detectors of gravitational waves. *Mon. Not. R. Astron. Soc.*, **224**:131, 1987.

[21] J. Aasi *et al.* The characterization of Virgo data and its impact on gravitational-wave searches. *Class.Quant.Grav.*, **29**:155002, 2012.

[22] P. Hello. Coupling of gravitational wave interferometric detectors. *Progress in Optics*, **38**:85–164, 1998.

[23] H. B. Callen and R. F. Greene. On a Theorem of Irreversible Thermodynamics. *Phys.Rev.*, **86**:702–710, 1952.

[24] P. R. Saulson. Thermal noise in mechanical experiments. *Phys.Rev.*, **D42**:2437–2445, 1990.

[25] F. Acernese *et al.* Properties of seismic noise at the VIRGO site. *Class.Quant.Grav.*, **21**:S433–S440, 2004.

[26] G. Ballardin, L. Bracci, S. Braccini, C. Bradaschia, C. Casciano, *et al.* Measurement of the VIRGO superattenuator performance for seismic noise suppression. *Rev.Sci.Instrum.*, **72**:3643–3652, 2001.

[27] F. Acernese *et al.* Measurements of Superattenuator seismic isolation by Virgo interferometer. *Astroparticle Physics*, **33**(3):182 – 189, 2010.

[28] M. Punturo. The Virgo sensitivity curve. Technical report, Virgo, 2004.

[29] M. Zimmermann and E. Szedenits. Gravitational waves from rotating and precessing rigid bodies: Simple models and applications to pulsars. *Phys. Rev. D*, **20**:351–355, 1979.

[30] R. N. Manchester, G. B. Hobbs, A. Teoh, and M. Hobbs. The Australia Telescope National Facility pulsar catalogue. *Astron.J.*, **129**:1993, 2005.

[31] B. Allen. *Relativistic Gravitation and Gravitational Radiation*, chapter The stochastic gravity-wave background: sources and detection. Cambridge University Press, 1997.

[32] T. Damour and A. Vilenkin. Gravitational radiation from cosmic (super)strings: Bursts, stochastic background, and observational windows. *Phys.Rev.*, **D71**:063510, 2005.

[33] K. A. Postnov and L. R. Yungelson. The Evolution of Compact Binary Star Systems. *Living Reviews in Relativity*, **17**(3), 2014.

[34] L. Blanchet. Gravitational Radiation from Post-Newtonian Sources and Inspiralling Compact Binaries. *Living Rev.Rel.*, **17**:2, 2014.

[35] B. Allen, W. G. Anderson, P. R. Brady, D. A. Brown, and J. D. Creighton. FINDCHIRP: An Algorithm for detection of gravitational waves from inspiraling compact binaries. *Phys.Rev.*, **D85**:122006, 2012.

[36] N. Wiener. *Extrapolation, interpolation and smoothing of stationary time series*. The Technology Press of the MIT, John Wiley and Sons, New York., 1960.

[37] J. Abadie *et al.* Predictions for the rates of compact binary coalescences observable by ground-based gravitational-wave detectors. *Classical and Quantum Gravity*, **27**(17):173001, 2010.

[38] C. D. Ott. The Gravitational Wave Signature of Core-Collapse Supernovae. *Class.Quant.Grav.*, **26**:063001, 2009.

[39] H. Dimmelmeier, J. A. Font, and E. Muller. Relativistic simulations of rotational core collapse. 2. Collapse dynamics and gravitational radiation. *Astron.Astrophys.*, **393**:523–542, 2002.

[40] H. Dimmelmeier, C. D. Ott, A. Marek, and H.-T. Janka. Gravitational wave burst signal from core collapse of rotating stars. *Phys. Rev. D*, **78**:064056, 2008.

[41] W.-Q. Zhang, S. Woosley, and A. Heger. Fallback and Black Hole Production in Massive Stars. *Astrophys.J.*, **679**, 2008.

[42] L. Dessart, A. Burrows, E. Livne, and C. Ott. Multi-dimensional radiation/hydrodynamic simulations of protoneutron star convection. *Astrophys.J.*, **645**:534–550, 2006.

[43] W. Keil, H. T. Janka, and E. Muller. Ledoux convection in protoneutron stars: A Clue to supernova nucleosynthesis? *Astrophys.J.Lett.*, **473**, 1996.

[44] J. A. Miralles, J. A. Pons, and V. Urpin. Convective instability in proto-neutron stars. *Astrophys.J.*, **543**:1001–1006, 2000.

[45] J. A. Miralles, J. Pons, and V. Urpin. Anisotropic convection in rotating proto-neutron stars. *Astron.Astrophys.*, **420**:245–249, 2004.

[46] E. Müller, M. Rampp, R. Buras, H.-T. Janka, and D. H. Shoemaker. Toward Gravitational Wave Signals from Realistic Core-Collapse Supernova Models. *The Astrophysical Journal*, **603**(1):221, 2004.

[47] E. Müller and H.-T. Janka. Gravitational radiation from convective instabilities in Type II supernova explosions. *Astronomy and Astrophysics*, **317**:140, 1997.

[48] C. D. Ott, A. Burrows, T. A. Thompson, E. Livne, and R. Walder. The spin periods and rotational profiles of neutron stars at birth. *Astrophys.J.Suppl.*, **164**:130–155, 2006.

[49] D. Lai and S. L. Shapiro. Gravitational radiation from rapidly rotating nascent neutron stars. *Astrophys.J.*, **442**:259, 1995.

[50] D. Lai. Astrophysical Sources for Ground-Based Gravitational Waves Detectors. In J. Centrella, editor, *AIP Conf. Proc 575*, page 146. 2001.

[51] A. Corsi and P. Meszaros. GRB afterglow plateaus and Gravitational Waves: multi-messenger signature of a millisecond magnetar? *Astrophys.J.*, **702**:1171–1178, 2009.

[52] S.-L. Ou, J. E. Tohline, and L. Lindblom. Nonlinear development of the secular bar-mode instability in rotating neutron stars. *Astrophys.J.*, **617**:490–499, 2004.

[53] L. Lindblom, B. J. Owen, and S. M. Morsink. Gravitational radiation instability in hot young neutron stars. *Phys.Rev.Lett.*, **80**:4843–4846, 1998.

[54] R. Bondarescu, S. A. Teukolsky, and I. Wasserman. Spinning down newborn neutron stars: nonlinear development of the r-mode instability. *Phys.Rev.*, **D79**:104003, 2009.

[55] B. J. Owen, L. Lindblom, C. Cutler, B. F. Schutz, A. Vecchio, *et al.* Gravitational waves from hot young rapidly rotating neutron stars. *Phys.Rev.*, **D58**:084020, 1998.

[56] B. J. Owen and L. Lindblom. Gravitational radiation from the r mode instability. *Class.Quant.Grav.*, **19**:1247–1254, 2002.

[57] R. Bondarescu, S. A. Teukolsky, and I. Wasserman. Spin Evolution of Accreting Neutron Stars: Nonlinear Development of the R-mode Instability. *Phys.Rev.*, **D76**:064019, 2007.

[58] A. L. Piro and E. Pfahl. Fragmentation of Collapsar Disks and the Production of Gravitational Waves. *Astrophys.J.Lett.*, **658**:1173, 2007.

[59] M. van Putten. Proposed source of gravitational radiation from a torus around a black hole. *Phys.Rev.Lett.*, **87**:091101, 2001.

[60] M. van Putten. LIGO/VIRGO searches for gravitational radiation in hypernovae. *Astrophys.J.*, **575**:L71–L74, 2002.

[61] M. van Putten. Gravitational Waveforms of Kerr Black Holes Interacting with High-Density Matter. *Astrophys.J.Lett.*, **684**:91, 2008.

[62] S. Woosley and J. Bloom. The Supernova Gamma-Ray Burst Connection. *Ann.Rev.Astron.Astrophys.*, **44**:507–556, 2006.

[63] J. Abadie *et al.* Search for gravitational waves from low mass compact binary coalescence in LIGO's sixth science run and Virgo's science runs 2 and 3. *Phys. Rev. D*, **85**:082002, 2012.

[64] J. Aasi *et al.* Search for gravitational waves from binary black hole inspiral, merger, and ringdown in LIGO-Virgo data from 2009-2010. *Phys. Rev. D*, **87**:022002, 2013.

[65] R. M. O'Leary, F. A. Rasio, J. M. Fregeau, N. Ivanova, and R. W. O'Shaughnessy. Binary mergers and growth of black holes in dense star clusters. *Astrophys.J.*, **637**:937–951, 2006.

[66] R. M. O'Leary, B. Kocsis, and A. Loeb. Gravitational waves from scattering of stellar-mass black holes in galactic nuclei. *Mon.Not.Roy.Astron.Soc.*, **395**(4):2127–2146, 2009.

[67] P. Csizmadia, G. Debreczeni, I. Racz, and M. Vasuth. Gravitational waves from spinning eccentric binaries. *Class.Quant.Grav.*, **29**:245002, 2012.

[68] W. E. East, S. T. McWilliams, J. Levin, and F. Pretorius. Observing complete gravitational wave signals from dynamical capture binaries. *Phys.Rev.*, **D87**(4):043004, 2013.

[69] Y. Guersel and M. Tinto. Near optimal solution to the inverse problem for gravitational wave bursts. *Phys.Rev.*, **D40**:3884–3938, 1989.

[70] E. E. Flanagan and S. A. Hughes. Measuring gravitational waves from binary black hole coalescences: 2. The Waves' information and its extraction, with and without templates. *Phys.Rev.*, **D57**:4566–4587, 1998.

[71] W. G. Anderson, P. R. Brady, J. D. Creighton, and E. E. Flanagan. An Excess power statistic for detection of burst sources of gravitational radiation. *Phys.Rev.*, **D63**:042003, 2001.

[72] J. Sylvestre. Time-frequency detection algorithm for gravitational wave bursts. *Phys. Rev. D*, **66**:102004, 2002.

[73] T. Pradier, N. Arnaud, M.-A. Bizouard, F. Cavalier, M. Davier, *et al.* An Efficient filter for detecting gravitational wave bursts in interferometric detectors. *Phys.Rev.*, **D63**:042002, 2001.

[74] B. Abbott *et al.* Upper limits on gravitational wave bursts in LIGO's second science run. *Phys.Rev.*, **D72**:062001, 2005.

[75] S. Klimenko, I. Yakushin, A. Mercer, and G. Mitselmakher. Coherent method for detection of gravitational wave bursts. *Class.Quant.Grav.*, **25**:114029, 2008.

[76] P. J. Sutton, G. Jones, S. Chatterji, P. M. Kalmus, I. Leonor, *et al.* X-Pipeline: An Analysis package for autonomous gravitational-wave burst searches. *New J.Phys.*, **12**:053034, 2010.

[77] LIGO-Virgo search papers, `https://www.lsc-group.phys.uwm.edu/ppcomm/Papers.html`.

[78] M. Edwards. *On the search for intermediate duration gravitational waves using the spherical harmonic basis.* Ph.D. thesis, Cardiff University, 2013.

[79] E. Thrane, S. Kandhasamy, C. D. Ott, W. G. Anderson, N. L. Christensen, *et al.* Long gravitational-wave transients and associated detection strategies for a network of terrestrial interferometers. *Phys.Rev.*, **D83**:083004, 2011.

[80] B. Abbott *et al.* Search for gravitational waves associated with 39 gamma-ray bursts using data from the second, third, and fourth LIGO runs. *Phys. Rev. D*, **77**:062004, 2008.

[81] W. H. Press, S. A. Teukolsky, W. T. Vetterling, and B. P. Flannery. *Numerical Recipes in FORTRAN: The Art of Scientific Computing, Second Edition.* Cambridge University Press, 1992.

[82] T. Burstegard and E. Thrane. Burstegard: a hierarchical clustering algorithm. Technical Report LIGO-L1200204-v1, LIGO scientific collaboration, 2012.

[83] T. Prestegard, E. Thrane, N. L. Christensen, M. W. Coughlin, B. Hubbert, *et al.* Identification of noise artifacts in searches for long-duration gravitational-wave transients. *Class.Quant.Grav.*, **29**:095018, 2012.

[84] J. Abadie *et al.* Sensitivity to Gravitational Waves from Compact Binary Coalescences Achieved during LIGO's Fifth and Virgo's First Science Run. 2010.

[85] M. Was, M.-A. Bizouard, V. Brisson, F. Cavalier, M. Davier, *et al.* On the background estimation by time slides in a network of gravitational wave detectors. *Class.Quant.Grav.*, **27**:015005, 2010.

[86] M. Was, M.-A. Bizouard, V. Brisson, F. Cavalier, M. Davier, *et al.* Limitations of the time slide method of background estimation. *Class.Quant.Grav.*, **27**:194014, 2010.

[87] M. H. M. van Putten, A. Levinson, H. K. Lee, T. Regimbau, M. Punturo, *et al.* Gravitational radiation from gamma-ray bursts as observational opportunities for LIGO and VIRGO. *Phys.Rev.*, **D69**:044007, 2004.

[88] L. Santamaría and C. Ott. Gravitational Wave Emission from Accretion Disk Instabilities – Analytic Models. Technical Report LIGO-T1100093-v1, LIGO scientific collaboration and Virgo collaboration, 2011.

[89] `http://www.grid.kfki.hu/twiki/bin/view/RmiVirgo/CBwaves`.

[90] J. Abadie *et al.* All-sky search for gravitational-wave bursts in the second joint LIGO-Virgo run. *Phys.Rev.*, **D85**:122007, 2012.

[91] J. Abadie *et al.* Search for Gravitational Waves from Intermediate Mass Binary Black Holes. *Phys.Rev.*, **D85**:102004, 2012.

[92] P. R. Brady, J. D. Creighton, and A. G. Wiseman. Upper limits on gravitational-wave signals based on loudest events. *Class.Quant.Grav.*, **21**:S1775–S1782, 2004.

[93] J. Aasi *et al.* Search for gravitational waves associated with gamma-ray bursts detected by the InterPlanetary Network. 2014.

[94] J. Abadie *et al.* Calibration of the LIGO Gravitational Wave Detectors in the Fifth Science Run. *Nucl.Instrum.Meth.*, **A624**:223–240, 2010.

[95] B. P. Abbott *et al.* Search for high frequency gravitational-wave bursts in the first calendar year of LIGO's fifth science run. *Phys. Rev. D*, **80**:102002, 2009.

[96] B. P. Abbott *et al.* Search for gravitational-wave bursts in the first year of the fifth LIGO science run. *Phys. Rev. D*, **80**:102001, 2009.

[97] J. Abadie *et al.* All-sky search for gravitational-wave bursts in the first joint LIGO-GEO-Virgo run. *Phys. Rev. D*, **81**:102001, 2010.

[98] J. Abadie *et al.* Predictions for the Rates of Compact Binary Coalescences Observable by Ground-based Gravitational-wave Detectors. *Class.Quant.Grav.*, **27**:173001, 2010.

[99] Burst Group 2013-2014 white paper, `https://wiki.ligo.org/Bursts/WhitePaper2013`.

[100] S. Chatterji. *The search for gravitational wave bursts in data from the second LIGO science run.* Ph.D. thesis, MIT, 2005.

Résumé

Cette thèse présente les résultats de l'analyse all-sky STAMPAS de recherche de signaux transitoires longs d'ondes gravitationnelles, dans les données 2005-2007 des interféromètres LIGO et Virgo. Les ondes gravitationnelles sont des perturbations de la métrique de l'espace-temps, et les expériences Virgo et LIGO sont conçues pour les détecter. Ces expériences sont des interféromètres de Michelson, avec des bras longs respectivement de 3 km et 4 km, dont la luminosité en sortie est modifiée lors du passage d'une onde gravitationnelle.

Jusqu'à très récemment, les pipelines de recherche de signaux transitoires se concentraient uniquement sur les signaux courts, qui durent moins d'une seconde, et sur les signaux de coalescence de binaires. STAMPAS est l'un des tout premiers pipelines entièrement dédiés à la recherche de signaux transitoires longs, qui durent d'une à plusieurs centaines de secondes.

Ces signaux sont émis, entre autres, par les instabilités qui apparaissent pendant la violente création des proto-étoiles à neutrons. Les instabilités dans les supernovæ à effondrement gravitationnel et celles des disques d'accrétion sont également de possibles sources de signaux transitoires longs. Les coalescences de binaires excentriques de trous noirs sont elles aussi censées émettre de puissantes ondes gravitationnelles pendant plusieurs secondes avant leur fusion.

STAMPAS est basé sur la corrélation de données issues de deux interféromètres. On construit des cartes temps-fréquence à partir des données, et leurs pixels les plus significatifs sont agrégés et forment les "triggers" (candidats potentiels d'ondes gravitationnelles). Aucune hypothèse sur la provenance, le temps ou la forme des signaux recherchés n'est formulée.

La première analyse effectuée avec STAMPAS a été réalisée à partir des données acquises entre 2005 et 2007 par les deux détecteurs LIGO. Après une sélection rigoureuse des "triggers", l'analyse en a révélé un taux proche du bruit Gaussien attendu, ce qui constitue un accomplissement majeur. Aucune onde gravitationnelle n'a été détectée, et nous avons établi des limites hautes sur les taux astrophysiques de plusieurs modèles de sources d'instabilités de disques d'accrétion et de coalescences de binaires excentriques de trous noirs. Le pipeline STAMPAS a montré qu'il sera efficace dans la recherche des signaux transitoires longs d'ondes gravitationnelles lors de la prochaine génération d'interféromètres.

Mots clés : Ondes gravitationnelles, Interférométrie, Signaux transitoires longs, Analyse du signal, Instabilités de disque d'accrétion, Binaires excentriques de trous noirs.

Abstract

This thesis presents the results of the STAMPAS all-sky search for long transient gravitational waves in the 2005-2007 LIGO-Virgo data. Gravitational waves are perturbations of the space-time metric. The Virgo and LIGO experiments are designed to detect such waves. They are Michelson interferometers with 3 km and 4 km long arms, whose light output is altered during the passage of a gravitational wave.

Until very recently, transient gravitational wave search pipelines were focused on short transients, lasting less than 1 second, and on binary coalescence signals. STAMPAS is one of the very first pipelines entirely dedicated to the search of long transient gravitational wave signals, lasting from 1s to $\mathcal{O}(100s)$.

These signals originate, among other sources, from instabilities in protoneutron stars as a result of their violent birth. The standing accretion shock instability in core collapse supernovae or instabilities in accretion disks are also possible mechanisms for gravitational wave long transients. Eccentric black hole binary coalescences are also expected to emit powerful gravitational waves for several seconds before the final plunge.

STAMPAS is based on the correlation of data from two interferometers. Time-frequency maps of the data are extracted, and significant pixels are clustered to form triggers. No assumption on the direction, the time or the form of the signals is made.

The first STAMPAS search has been performed on the data from the two LIGO detectors, between 2005 and 2007. After a rigorous trigger selection, the analysis revealed that their rate is close to Gaussian noise expectation, which is a significant achievement. No gravitational wave candidate has been detected, and upper limits on the astrophysical rates of several models of accretion disk instability sources and eccentric black holes binary coalescences have been set. The STAMPAS pipeline demonstrated its capabilities to search for any long transient gravitational wave signals during the advanced detector era.

Keywords: Gravitational waves, Interferometry, Long transients, Signal Processing, Accretion Disk Instabilities, Eccentric Black Hole Binaries